Towards label-free, non-invasive phenotypic characterization of advanced cell culture models

DISSERTATION

zur Erlangung des

Doktorgrades der Naturwissenschaften

(Dr. rer. nat.)

der Fakultät Chemie und Pharmazie der Universität Regensburg

vorgelegt von

Tobias Naber

aus Regensburg

im Jahr 2025

Towards label-free, non-invasive phenotypic characterization of advanced cell culture models

DISSERTATION

zur Erlangung des

Doktorgrades der Naturwissenschaften

(Dr. rer. nat.)

der Fakultät Chemie und Pharmazie der Universität Regensburg

vorgelegt von

Tobias Naber

aus Regensburg

im Jahr 2025

Diese Arbeit entstand in der Zeit von Januar 2021 bis Mai 2025 am **Institut für Analytische Chemie, Chemo- und Biosensorik** der Fakultät Chemie und Pharmazie der Universität Regensburg sowie am **Fraunhofer Institut für Elektronische Mikrosysteme und Festkörpertechnologien (EMFT)**.

Die Arbeit wurde unter der Leitung von Prof. Dr. Joachim Wegener angefertigt.

Promotionsgesuch eingereicht am: 27.05.2025

Kolloquiums Termin am: _____

Prüfungsausschuss:

Vorsitzender:	PD Dr. Thomas Hirsch
Erstgutachter:	Prof. Dr. Joachim Wegener
Zweitgutachter:	Prof. Dr. Karsten Haupt
	(Université de Technologie de Compiègne)
Drittprüferin:	Apl. Prof. Dr. Miriam Breunig

Für meine Familie

"The audience has waited all this time

You're well-rehearsed and you know your lines

So introduce them to

The wonderful dysfunctional you"

Shinedown. "Dysfunctional You". By Eric Bass. Planet Zero

1 INTRODUCTION 1

1.1 ADVANCED CELL CULTURE MODELS IN DRUG DISCOVERY 1
1.2 CHARACTERIZATION OF 3D CELL CULTURE MODELS 6

2 OBJECTIVES 12

3 MATERIAL AND METHODS 14

3.1 GENERAL CELL CULTURE CONDITIONS 14
3.1.1 WORKING WITH MAMMALIAN CELL LINES 14
3.1.2 CELL LINES UNDER STUDY 14
3.1.3 SUBCULTIVATION PROTOCOLS 16
3.1.4 CULTIVATION OF TUMOR SPHEROIDS 18
3.1.5 COMPOSITION OF BUFFERS AND SOLUTIONS 19
3.2 IMPEDANCE ANALYSIS 20
3.2.1 BASIC PRINCIPLES OF IMPEDANCE-BASED CELL MONITORING 20
3.2.2 ELECTRIC-CELL-SUBSTRATE IMPEDANCE SENSING (ECIS) 21
3.2.3 REAL TIME MONITORING OF TRANSEPITHELIAL ELECTRICAL RESISTANCE (TER) 22
3.2.4 CIS-TER: EXPERIMENTAL SETUP 24
3.3 RATIOMETRIC OPTICAL IMAGING 27
3.3.1 THEORETICAL BACKGROUND 27
3.3.2 COMMERCIAL SETUP FOR OXYGEN AND PH IMAGING 29
3.3.3 CALIBRATION OF SENSOR FOILS 30
3.3.4 DATA EVALUATION PROCESS FOR RATIOMETRIC OPTICAL IMAGING 31
3.4 TER-OX: EXPERIMENTAL SETUP 35

4 RATIOMETRIC OPTICAL OXYGEN IMAGING OF 3D CELL CULTURE MODELS 38

4.1 GENERAL REMARKS ON OXYGEN PROFILING 38
4.1.1 VALIDATION OF ASSAY PLATFORM USING FINITE ELEMENT ANALYSIS 38
4.1.2 DETERMINATION OF OXYGEN CONSUMPTION RATES – A COMPARISON 40
4.2 MAPPING OF OXYGEN PROFILES UNDERNEATH TUMOR SPHEROIDS CULTURED ON POROUS SUPPORTS 46

4.2.1 Influence of the porous support on oxygen profile 46
4.2.2 Influence of cell type and spheroid size on oxygen profile 50
4.2.3 Development of lateral oxygen profiles over time 52
4.2.4 Application of oxidative phosphorylation modulators 55
4.2.5 Towards a higher throughput 60
4.2.6 Conclusion and Outlook 61
4.3 Mapping of oxygen profiles underneath complex 3D cell culture models 63
4.3.1 Organoids and Tumoroids 63
4.3.2 Precision-cut tissue slices 69
4.3.3 Conclusion and Outlook 72

5 RATIOMETRIC OPTICAL PH IMAGING OF 2D AND 3D CELL CULTURE MODELS 74

5.1 pH monitoring of 2D cell layers cultured on permeable substrates 74
5.1.1 Influence of cell-to-sensor distance 74
5.1.2 Impact of glucose deprivation and oxidative phosphorylation modulators on EAR 75
5.1.3 Sequential analysis of oxygen consumption and extracellular acidification 80
5.2 Monitoring of pH gradients underneath tumor spheroids 83
5.2.1 pH mapping underneath tumor spheroids cultured directly on the sensor foil 83
5.2.2 pH mapping underneath tumor spheroids cultured on permeable substrates 86
5.2.3 Sequential analysis of oxygen and pH gradients underneath tumor spheroids 88
5.3 Conclusion & Outlook 91

6 TER-OX: SIMULTANEOUS MONITORING OF EPITHELIAL BARRIER FUNCTION (TER) AND RESPIRATION (OX) 93

6.1 Establishment of the TER-Ox platform 93
6.1.1 Characterization of different cell types using TER-Ox 93
6.1.2 Comparison of TER-Ox to established platforms 96
6.2 Application of the TER-Ox platform 98
6.2.1 Monitoring of drug induced changes 98
6.2.2 Monitoring of epithelial-to-mesenchymal transition 99
6.2.3 Characterization of complex tissue models 101

6.3 Conclusion and Outlook 103

7 CIS-TER: IMPEDANCE SPECTROSCOPIC MONITORING OF INDIRECT CO-CULTURES 105

7.1 Development of electrode setups for impedance sensing of the basolateral cell layer 105
7.2 Histamine treatment of U373 cells cultured underneath barrier forming cell lines 109
7.3 Conclusion & Outlook 113

8 SUMMARY 115

9 ZUSAMMENFASSUNG 117

10 PUBLICATION BIBLIOGRAPHY 120

11 APPENDIX 136

11.1 Supplementary Information 136
11.2 Consumables and Devices 141
11.3 Abbreviations 143
11.4 Curriculum Vitae 146
11.5 List of publications 148
11.6 Danksagung 149
11.7 Eidesstaatliche Erklärung 151

1 Introduction

1.1 Advanced cell culture models in drug discovery

The use of cell-based tissue and disease models is of great importance during drug development processes. Absorption, transport, toxicity, and efficacy of drugs are often initially screened with the help of cell-based models especially during the pre-clinical phase. Drug discovery relied on the use of 2D cell monolayers for decades. Even though cell monolayers are easy to handle and the application of monolayers is fast and cheap, the approach has an obvious limited biological relevance compared to the complex surroundings *in vivo* (Duval et al. 2017). This leads to a less accurate predictability of the important drug characteristics listed above. Ultimately many drugs later fail during the extremely time-consuming and costly clinical phases (Sun et al. 2022). A solution might be offered by applying advanced tissue models for drug development.

Advanced monolayer culture

A first approach is presented by introducing co-cultures of two or more cell types within a monolayer. The mixed monolayers can either be formed by mixing different cell types during cell inoculation or by using micropatterning (Goubko and Cao 2009). The resulting co-cultures can be used to study cell-cell contacts and communication between the different cell types (Bogdanowicz and Lu 2013). Culture of monolayers on permeable membranes instead of impermeable plastics presents a second option of improving monolayer culture (Sheridan et al. 2008). The permeable nature of porous substrates mimics *in-vivo* conditions more closely compared to impermeable substrates. The possibility to expose the cells to fluids from both sides provides a more physiological environment for cell differentiation and polarization (Patrone et al. 1992; Mazzocchi et al. 2014). In addition, the use of permeable substrates enabled the indirect co-culture of two different layers on opposite sides of the membrane, making crosstalk between two different cell layers accessible (Chung et al. 2018). However, these models still rely on the use of monolayers lacking the complex 3D environment *in-vivo*. To overcome the issue of missing biological complexity and to bridge the gap between *in vivo* and *in-vitro*, scientists try to culture cells in more complex 3D environments enabling interactions between different cell types as well as between cells and the extracellular matrix. In addition, sophisticated 3D culture offers the possibility to create models mimicking organ functions (Cacciamali et al. 2022).

Layer-by-Layer Co-Cultures

One option to provide a 3D cell structure is the direct co-culture of cells in multilayers. As a result, two or more different cell layers are stacked on top of each other. Layered co-culture can be achieved in a scaffold free environment based on the formation of ECM proteins by the applied cell types. However, the use of external scaffolds in tissue engineering can be beneficial. Layer-by-Layer culture of cells is mainly used to mimic barriers formed by cells *in-vivo*. A prominent example of a cellular barrier consisting of different layers of cells is skin. Layered co-culture models of the skin are mainly based on the co-culture of keratinocytes with a second cell type important for the skin's functionality (Choudhury and Das 2021). Kim et al. co-cultured keratinocytes with fibroblasts forming a cell-based model with skin-like morphology. The developed model was successfully used to determine the effect of antifibrotic drugs and the resulting tissue was used as transplant to close skin wounds in mice (Kim et al. 2018). To study the interaction between keratinocytes and neuronal cells, Ahn et al. proposed a co-culture of these cells using a microfluidic chip. The two cell types are thereby cultured in two channels separated by a hydrogel mimicking the extracellular matrix. The approach enabled the formation of an innervated epidermal keratinocyte layer (Ahn et al. 2023). Other studies focused on layered co-culture models of important cellular barriers formed in different organs such as the lung (Shiraishi et al. 2024), the liver sinusoid (Kang et al. 2013) and the uterine wall (Shlomo et al. 2024). Takahashi et. al used a co-culture model of patient-derived cancer cells with 3D stromal tissues formed *in-vitro* to determine anticancer drug effects which are highly affected by the interaction of cancer cells with their surrounding (Takahashi et al. 2024).

Spheroids and organoids

The culture of anchorage-dependent cells in non-adhesive surroundings results in the formation of cellular aggregates. Depending on the complexity of these aggregates, they are called spheroids or organoids (Figure 1 A). In comparison to 2D culture, culturing cells in the third dimension more closely reproduces cell-cell and cell-matrix contacts, as well as the supply and gradient of nutrients present *in vivo* (Vakhshiteh et al. 2023). The most convenient cellular 3D aggregates are multicellular spheroids (MCS). Spheroids are spherical aggregates of cells made up of three different zones called the proliferative zone, the quiescent zone and the necrotic core (Figure 1 B). The proliferative zone is the outermost rim of the spheroid. Cells located in this zone are alive and proliferating as they have space to duplicate, experience the best access to nutrients from the culture fluid and metabolic waste products do not accumulate. Cells in the

quiescent zone of the spheroid are alive but do not proliferate anymore. The inner zone, the necrotic core, consists of mostly dead cells. Up to a certain critical size strongly dependent on the cell line, spheroids may form without necrotic cores (Mueller-Klieser et al. 1986; Hirschhaeuser et al. 2010). Formation of spheroids requires culturing cells in a non-adhesive manner. Over the past years, several different options to produce uniform spheroids in medium to high numbers have evolved. The strategies can be divided in scaffold free and scaffold-based techniques (Dirheimer et al. 2022). Scaffold based techniques use hydrogels like Matrigel® or Collagen for spheroid formation. Scaffold free approaches concentrate on the culture of cells in non-adhesive surroundings. Therefore, the cells can be cultured in wells coated with agents preventing cell adherence. As cells cannot adhere and spread on the surface anymore, cellular aggregation is promoted, and spheroids are formed over time. This approach is commonly referred to as *liquid overlay technique* (Yuhas et al. 1977). In the *hanging drop technique*, cells are cultured in a small droplet hanging from the lid of a standard cell culture plate. The surface tension formed by the droplet and gravitational forces lead to an aggregation of the cells in the apex of the droplet (Kelm et al. 2003). Other scaffold free methods use constant stirring or microfluidics to force cells into spheroid formation (Vadivelu et al. 2017). While liquid overlay, hanging drop and stirring based approaches are rather cheap and easy to apply, they are often associated with low reproducibility of spheroid size and shape. Microfluidic devices are reported to offer a more sophisticated and reliable way to form uniform spheroids, however the setup can be rather complex and expensive (Vakhshiteh et al. 2023). Spheroids can either be formed from a single cell type (homotypic), or by combining several different cell types into a co-culture model (heterotypic). Spheroids are mainly used to mimic the early phases of the formation of avascular solid tumors and can therefore be applied to testing of anti-tumor therapies (Hirschhaeuser et al. 2010). Apart from cancer research spheroids have been used in tissue engineering, emulating bone and cartilage regeneration as well as regeneration processes in liver, nerve and skin tissue (Chae et al. 2021).

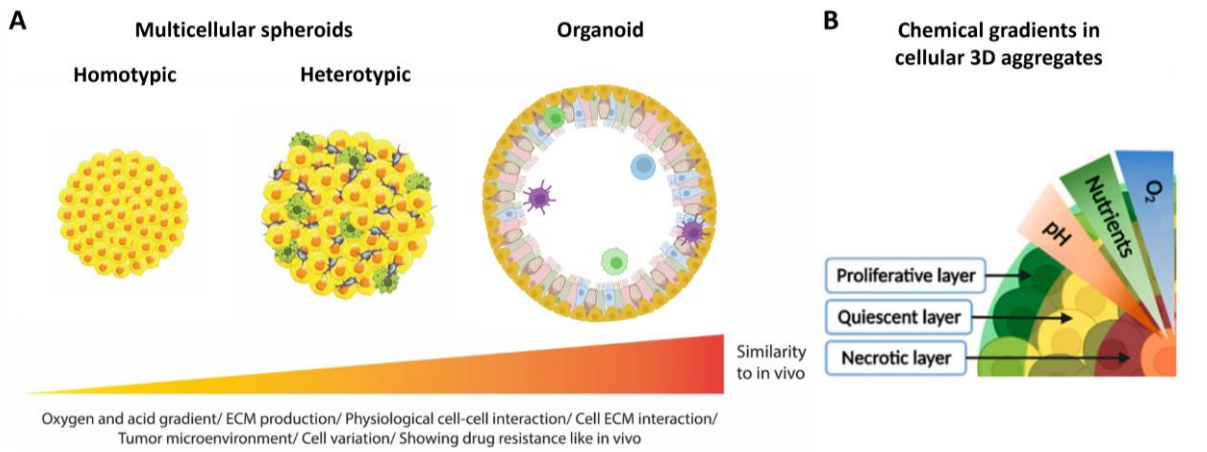

Figure 1: (A) Schematic illustration of different 3D cell culture models. Adapted from Vakhshiteh et al. 2023. Created in BioRender. (B) Chemical gradients and resulting evolving zones within cellular 3D aggregates. Adapted from Dirheimer et al. 2022.

A more advanced method of culturing cells in 3D is the formation of organoids (Zhao et al. 2022). In comparison to multicellular spheroids, organoids are capable of self-organization and self-renewal. Additionally, organoids exhibit organ specific functions. While spheroids mainly rely on cell lines, organoids are produced using primary material, progenitor cells or stem cells. The use of *human induced pluripotent stem cells* (hiPSCs) enables the development of patient derived organoid models without ethical concerns. In 2012 Yamanaka has been rewarded with the Nobel Prize in Physiology and Medicine for the generation of human induced pluripotent stem cells (Ochi 2013). For formation of organoids, iPSCs are usually cultured on ultra-low attachment plates in matrices like Matrigel®, collagen or synthetic hydrogels. Additionally, the growth medium needs to be supplemented with soluble factors driving the differentiation into cell types to be present in the desired tissue. Organoids from iPSC have been successfully developed for many organ types, including intestine, lung, pancreas, heart, skin and brain (Zhao et al. 2022). Organoids have already been used in a variety of different applications including the study of infectious diseases, genetic disorders and cancer (Kim et al. 2020). Even though organoids are a highly promising tool in 3D cell culture, they do suffer from certain drawbacks that need to be addressed. The development of organoids from stem cells leads to a limited maturation of the tissue. Additionally, the lack of vascularization can lead to the formation of necrotic cores as organoids are typically quite large with diameters above 1 mm. Apart from biological limitations, the process of generating organoids is more time consuming and costly compared to more simple 3D models such as spheroids or multilayers (Andrews and Kriegstein 2022).

Precision-Cut Tissue Slices

A rather different option to gain excess to three-dimensional tissue models is the use of *ex-vivo precision cut tissue slices* (PCTS). PCTS are derived from biopsies of humans or animals which are subsequently cut into thin slices of the original tissue (Parrish et al. 1995). The size thickness of the tissue slice depends on the organ of origin and typically ranges between 100 µm and 600 µm (Majorova et al. 2021). The preparation and the slicing protocols are similar with slight alterations for different tissues. To prepare the tissue slices, the explanted tissue is directly transferred to a preservation solution. The tissues are then cut into cylindrical cores. Depending on the organ of origin, tissues must be stabilized before by agarose inflation. Agarose inflation is needed for so called non-solid organs as for example the lung (Lam et al. 2023; Graaf et al. 2010). The prepared slices can be cultured in the lab for approximately one week until some of the cell types present in the slice start to take damage or die. Hence, a main task in PCTS research is the expansion of the slice's lifetime. PCTS have already been prepared for many different organ types and in many different applications, such as toxicology, pharmaceutical research and more recently also in studying host-pathogen interactions (Majorova et al. 2021; Davies et al. 2015). Compared to the other above mentioned *in-vitro* models, *precision cut tissue slices* are very closely resembling the cellular composition and most importantly structural complexity of the host tissue (Lam et al. 2023). However, access to precision cut slices, especially of human material, is very limited and the preparation procedures are complex and can only be performed by highly trained personnel. In addition, the long-term culture of PCTS is a problem which needs to be further evaluated in future research (Preuß et al. 2022).

1.2 Characterization of 3D cell culture models

As presented above 3D tissue and disease models are highly promising tools for drug discovery. In order to study effects of potential drugs on the developed models, tailored analytical tools are needed to characterize and detect changes upon drug exposure. However, development of analytical tools is far behind the existing biological methods. In order to effectively apply 3D tissue and disease models in the future, easy to use non-invasive tools will be of great importance. The following chapter will focus on existing tools, their strengths and weaknesses.

Destructive approaches

Destructive options analyzing 3D tissues can be divided into two main approaches. The aggregates can either be completely disassembled into single cell solutions or dissected into ultrathin sections. To obtain slices of spheroids or organoids, the tissue models are either embedded in a paraffin blocks or frozen. For embedding in paraffin, the samples first need to be fixed using paraformaldehyde and dehydrated in absolute ethanol and toluene before they are enclosed in an agarose matrix and finally treated with liquid paraffin. The paraffin block is cut with the help of a microtome. The resulting sections can be stored at 4 °C until further use (Guyon and Daubon 2023). To obtain cryosections, the aggregates must be embedded in commercially available cryomedium or in gelatine solutions. Afterwards, the samples are frozen using dry ice or liquid nitrogen. Finally, the frozen specimen is cut into cryosections using a cryotome. The resulting sections can be stored in liquid nitrogen until further use. Both methods can be used to obtain slices between 4 and 50 µm (Charlet-Faure et al. 2023). The obtained tissue slices can finally be analyzed using different approaches. Most common is the analysis using microscopy in combination with immunohistochemical or immunofluorescent staining (Wiley et al. 2016). After analysis of the 2D sections, a high resolution image of the 3D aggregate can be obtained by computer-assisted reconstruction of the z-stack (Parfitt 2019). Apart from microscopy, researchers have used mass spectrometry to spatially analyze the 2D slices. Similar to the microscopic analysis, the resulting distribution maps can be reconstructed to 3D images of the original specimen (Piehowski et al. 2020; Xie et al. 2020). These approaches result in highly resolved structural or molecular information on conditions within the spheroid. Microscopic techniques offer a possibility for in-depth analysis of cellular and extracellular structures, whereas mass spectrometry additionally enables the spatial analysis of metabolic changes within the aggregate.

Another option is the disassembly of 3D aggregates into single cell solutions, e.g. via EDTA and trypsin treatment. It is even possible to disassemble the spheroid with respect to the

different zones formed within. The single cell solutions can then be further analyzed with a variety of different methods which are also used to analyze 2D layers. Apart from simple approaches like viability assays and ATP-assays, the cell suspensions are assessable to more complex approaches such as flow cytometry and different omics analysis (Frandsen et al. 2021; Patra et al. 2016).

Destructive methods offer the possibility of an in-depth analysis of spheroids with high spatial resolution and a maximum of information gained. However, the aggregate is destroyed, and it is not possible to monitor changes within a tissue model over time, e.g. during prolonged drug treatments. In addition, these approaches are rather complex and labor intensive, as the protocols need many different small preparation steps.

Minimal invasive and label-based approaches

Apart from destructive methods, scientists have tried to analyze spheroids using methods which are locally invasive but maintain the overall structure of the 3D construct, or which rely on the use of chemical labels for the intact spheroid. While these approaches still interfere with the biological integrity of the specimen, these tools do not rely on the disassembly of the 3D cell culture model as seen for destructive approaches. An example for an invasive but not destructive approach are microelectrodes, which have been used for a long time to determine gradients of oxygen and pH within 3D aggregates (Mueller-Klieser and Sutherland 1982; Acker et al. 1987a). Positioning of the electrodes allows for determination of these gradients with spatial resolution.

Besides the use of invasive microneedles, it is possible to analyze spheroids by applying chemical reagents as probes for certain characteristics. The use of viability assays has become a well-established tool to determine drug induced effects on spheroids (Kijanska M. 2016). Well known examples are commercially available assays like CellTiter-Glo®, PrestoBlue® or MTT assays. These assays mainly rely on the conversion of precursor molecules to fluorophores or dyes. Their conversion is dependent on the metabolic activity and therefore the viability of the cells. The fluorescence or absorbance can then be analyzed with the help of plate readers (Kamiloglu et al. 2020). The conversion of the precursor molecule mainly relies on the cells present in the outer cell layers of the 3D aggregate and therefore does not offer information on the deeper or inner zones of the tissue model. While these assays lack in depth of information, they are easy to use and can be applied in high throughput which is of special interest in drug screening campaigns.

Labels and probes are also used to analyze 3D tissue models using microscopic techniques. However, microscopy of cellular aggregates suffers from several factors. The transport of labels/probes towards the center of the spheroid might be hindered by the tissue. Therefore, a uniform distribution of the label is not given, especially for bigger aggregates. This problem can be solved to some extent, e.g. by using smaller probes, or by adjusting the incubation time. The second and even more problematic factor is the penetration depth of visible light into tissue. This influences the excitation of the probe as well as the analysis of the emission (Sirenko et al. 2015). The main cause for the limited penetration depth is the scattering of visible light caused by the inhomogeneous refractive indices within the specimen. Combination of these issues can lead to images mainly depicting the outer layers of the aggregate rather than the complete specimen. To overcome these issues scientists have tried to use advanced microscopic techniques, such as multiphoton microscopy and light-sheet-based fluorescence microscopy which can enhance the penetration depth into tissue up to 1 cm (Costa et al. 2019). Another approach to enable better spatial resolution within the tissue models is the use of optical clearing methods. Optical clearing methods can be used to modify the optical properties of the specimen by removing, replacing or modifying individual components. Methods include immersion in solvents with high refractive indices or hydrogels, dehydration of the cell samples as well as delipidation using specialized detergents (Costa et al. 2019). Microscopic techniques are used with a variety of different labels and probes. Application of molecular probes or nanoparticles assessing cell viability, labeling structural elements of the cells, but also measuring extracellular metabolites such as glucose or oxygen have been developed. This enables a detailed analysis of many parameters influencing the formation, growth and conditions of cellular 3D models (Sirenko et al. 2015; Zamora-Perez et al. 2022). However, apart from the problematics caused by limited penetration of light in tissue, these approaches also suffer from photobleaching and/or cytotoxicity of the molecular probes which impedes the use of these approaches for time resolved monitoring (Schneckenburger and Richter 2021).

Non-invasive approaches

The option to analyze 3D tissue and disease models in a time resolved manner is best given by the application of non-invasive assay platforms.

A relatively simple and easy approach to measure effects of anticancer drugs on tumor spheroids is the measurement of spheroidal growth using phase contrast microscopy. Studies have shown that results of this label-free approach are in good agreement with results obtained using viability assays. However, in comparison to these assays the label-free analysis offers the

possibility of a repetitive and therefore time resolved analysis of drug treatments (Thakuri et al. 2019; Kessel et al. 2017).

A more complex microscopic technique visualizing 3D structures of cellular aggregates is a method called holotomography. Holotomography uses the different refractive indices and the resulting phase shift of the light within a specimen to create high resolution images of the spheroids 3D morphology. By applying the light source from different angles towards the tissue model, 3D images or holotomograms can be developed (Kim et al. 2024). The approach offers resolution on sub-cellular level, can be used for long-term monitoring and it can be adapted to automatization and therefore high-throughput (Lee et al. 2024).

Another option for label-free analysis of 3D tissue models is the use of impedance-based techniques. In impedance-based techniques, the biological specimen is cultured in between or on top of a set of electrodes. Afterwards an alternating current (AC) is applied to the electrodes. The signal can either be applied at a single distinct frequency or over a broad range of different frequencies. The ability of high-frequency AC to penetrate tissue enables the use of impedance measurements for the analysis of drug-induced changes on 3D tissue and disease models as the resulting impedance represents the inner dielectric structure of the specimen (Alexander et al. 2019). One of the biggest challenges to overcome when using impedance readouts to characterize 3D tissue models is the positioning of the aggregates on or between the electrodes such that sneak currents not penetrating the tissue are avoided or controlled. Electrode placement as well as aggregate placement can easily lead to leakage currents which impede the characterization of the aggregate. Therefore, researchers have come up with a variety of different approaches for the placement of spheroids (see Figure 2). Molckovsky and Wilson trapped spheroids in a specifically designed chamber between two rod-shaped electrodes and were able to distinguish between apoptosis and necrosis of the cells in the spheroid (Molckovsky and Wilson 2001). A second approach was presented by Hildebrandt et al., trapping spheroids formed by mesenchymal stem cells in a capillary with a diameter of 300 µm. The electrodes were positioned on either side of the capillary openings, forcing the current to flow through the entrapped spheroid. Using this approach, they were able to show that differentiation of the stem cells was measurable with an impedimetric setup (Hildebrandt et al. 2010). With the help of a microcavity array, researchers were able to determine differences between spheroids formed from different cells. Furthermore, they were able to resolve drug induced changes and drug efficacy on spheroids. The spheroids were cultured in a microcavity which was equipped with a set of electrodes applied on the side walls of the cavities (Kloss et al. 2008). Finally, impedance spectroscopy has been applied to microfluidic chips or flow

channels entrapping spheroids. Microfluidics were equipped with a variety of different coplanar electrodes but also with electrodes on opposite sides of the channel. Spheroids were mainly entrapped by using hydrogel cavities or constrictions of the channel (Hupf 2018; Wang et al. 2024; Chmayssem et al. 2022).

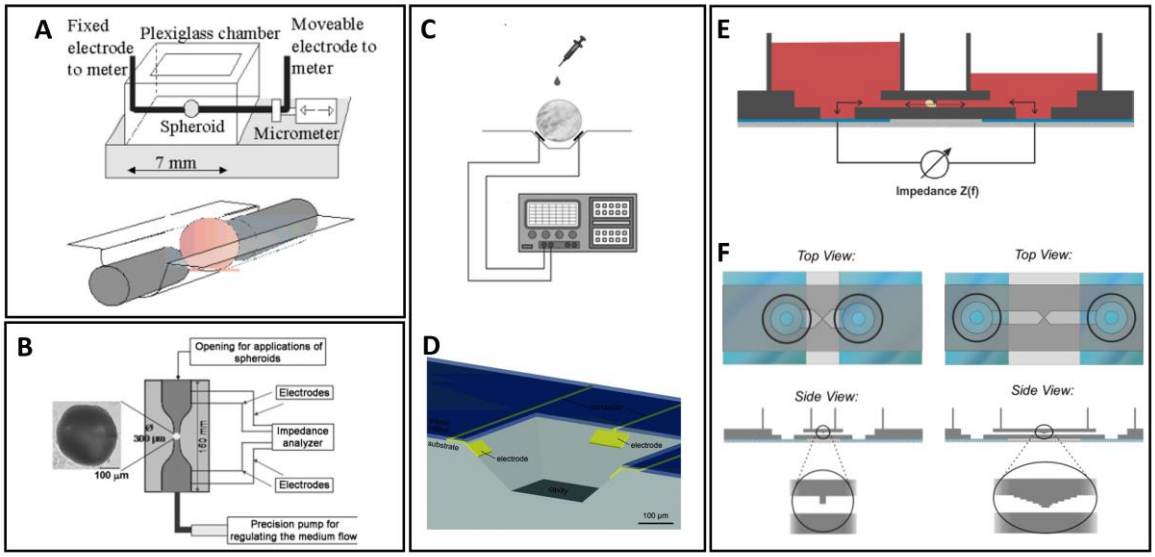

Figure 2: Comparison of impedance-based techniques to monitor tumor spheroids. (A) Spheroid is entrapped between two rod shaped electrodes. Adapted from Molckovsky and Wilson 2001. (B) Spheroid is entrapped in a capillary. Electrodes are placed on both ends of the capillary. Adapted from Hildebrandt et al. 2010. (C) & (D) Spheroid is placed in a microcavity. Electrodes are placed on the side walls of the cavity. Adapted from Kloss et al. 2008. (E) & (F) Spheroid is entrapped in a microfluidic channel. Electrodes are placed on either side of the channel. Adapted from Hupf 2018.

Another approach to monitor spheroids is presented by the commercially available Seahorse device. The device is based on a ratiometric optical readout of oxygen and pH and offers the possibility to integrally determine the respiratory rate as well as the extracellular acidification rate of 3D aggregates (Russell et al. 2017). A similar commercially available approach is called SensoSphere. Here, spheroids are cultured in microcavities doped with oxygen sensitive fluorophores enabling a ratiometric time resolved readout of the spheroid's oxygen consumption (Grün et al. 2023). However, both approaches suffer from a lack of information on the distribution of oxygen within the tumor spheroids.

Comparison of the different approaches.

The different approaches presented above have varying strengths and weaknesses quickly compared in Table 1. Destructive and invasive approaches suffer from the partial or even complete destruction of the studied tissue model. Due to this destructive nature, these approaches cannot be used to determine time-resolved changes of the tissue models. In addition, they are often relatively complex and need a lot of different working steps. However, the

information gained especially by fully destructive approaches is unmet. Label-based microscopic techniques offer a non-destructive way to gain similar information. However, they suffer from optical limitations due to necessary penetration of light in tissue. Label-based analysis is also used in common viability assays which offer a minimum of complexity and can therefore be easily applied to screening campaigns in need of high throughput. However, the information content is minimized to the viability of the cells. In addition, the use of labels prevents the option of time-resolved analysis. The labels themselves could have cytotoxic effects after certain incubation periods and in the case of microscopic applications the specimen must be fixed for the labeling process. Time-resolved monitoring can only be achieved by applying non-invasive monitoring approaches. These methods, however, still suffer from relatively low information content and a limited applicability to higher throughput. Therefore, it is crucial to develop novel and less complex techniques which can be used to characterize effects on 3D tissue and disease models over time.

Table 1: Comparison of different analytical approaches to characterize 3D tissue and disease models. -: weakness, 0: limitations in use, +: strength

Approach	Destructive approaches	Label-based viability assays	Label-based microscopy	Non-invasive monitoring
Avoiding Invasiveness	-	0	0	+
Information content	+	-	0	0
Temporal resolution	-	-	-	+
Low complexity	-	+	0	0
Throughput	0	+	0	0

2 Objectives

The use of more complex and advanced disease models in drug development processes could greatly improve the efficiency and accuracy of drug development and especially of pre-clinical studies. Examples of well-developed and advanced tissue models range from co-cultures in a monolayer over the combination of several monolayers to complex 3D structures, such as spheroids and organoids. However, the use of such models is not only dependent on physiologically relevant disease models, but also of the implementation of more effective analytical readout methods to characterize the multi-cellular tissue models. Until now, state of the art methods used to decipher impacts of drugs on advanced and in particular 3D cell culture models suffer from a lack of temporal and spatial resolution or are often invasive in nature. These assays mainly rely on staining, slicing and disassembling of the 3D cell culture models. In addition to their invasive nature, most of these methods do not allow monitoring of the same tissue model over time. Available label-free and time-resolved approaches are often complex and fail to offer detailed information on the cell culture model.

Therefore, this work focuses on the expansion of label-free and non-invasive assay platforms towards advanced disease models. In this process we aim to propose novel assays to determine:

i) epithelial barrier function and respiratory activity of 2D monolayers cultured on permeable substrates simultaneously,

ii) impedance characteristics of a combination of two indirectly co-cultured cellular monolayers,

iii) pH monitoring of cell monolayers cultured on permeable substrates,

iv) oxygen and pH monitoring of 3D tissue models based on the same cell type called spheroids, and

v) oxygen monitoring of 3D cell culture models based on a combination of different cell types, namely organoids and precision cut tissue slices.

Ratiometric optical imaging and impedance spectroscopy will form the basis for the readout platforms to be established. Ratiometric optical imaging of oxygen and pH serve as microphysiometric approach which will enable us to determine metabolic phenotypes of cells. Impedance spectroscopy on the other hand provides the possibility to examine morphological changes of cell bodies. This work aims to combine these principles in different technical settings

to characterize the biological systems, their metabolic phenotype and their dielectric structure, shortly listed above.

In particular, an assay platform determining the oxygen and pH profile within tumor spheroids shall be developed. By culturing the spheroids on permeable substrates which can be transferred between oxygen and pH sensors we aim to determine both phenotypes of the same tumor spheroid. Oxygen and pH sensing of tumor spheroids cultured on permeable substrates shall be developed using the VisiSens TD imaging kit. We aim to expand the use of ratiometric optical pH imaging to cellular monolayers and to spheroids cultured on permeable culture substrates. In the case of oxygen sensing, it shall only be investigated whether imaging of 3D tumor spheroids is possible, as the approach has already been used for 2D cell layers before (Naber et al. 2025).

In addition, more complex multicellular 3D cellular systems, namely brain organoids and precision cut tissue slices, shall be characterized using the VisiSens TD system. Brain organoids, derived from human induced pluripotent stem cells co-cultured with cancer cells are used as a niche model in metastasis research. These organoids shall be characterized regarding their oxygen profile in the presence and absence of co-cultured metastatic cancer cells. Moreover, a protocol shall be developed to determine the oxygen footprint of patient derived precision cut lung slices.

A further aim of this work is the development of a novel assay platform enabling the determination of the respiratory activity and the barrier integrity of monolayers cultured on permeable substrates. Therefore, the above-mentioned fundamental principles, impedance spectroscopy and ratiometric optical oxygen imaging, shall be combined in a novel measurement setup. The setup shall be compared to the established methods of barrier function and oxygen monitoring, cellZscope® and VisiSens TD. We aim to use the combinatory assay platform to determine drug induced changes as well as disease effects on 2D cell monolayers cultured on permeable substrates.

In a final system we are aiming to establish a setup which will enable the characterization of two individual cell layers cultured together in one experimental setup by impedance spectroscopy. The setup should combine a cell layer which is cultured on a permeable substrate hanging above a second cell layer directly cultured on thin-film gold film electrodes. The use of appropriate electrode design shall enable simultaneous monitoring of both cell layers.

3 Material and Methods

3.1 General Cell Culture Conditions

3.1.1 Working with mammalian cell lines

Working with living cell lines *in vitro* requires working in aseptic conditions. Therefore, cell culture work was performed under a laminar air flow cabinet (Thermo Fisher Scientific Inc., Waltham, USA). Cell culture consumables were either bought in sterile packaging or sterilized before use in a steam autoclave (DX-45, Systec GmbH & Co. KG, Linden, Germany). All solutions were pre-warmed in a waterbath (Julabo, Type TW12, Seelbach, Germany) to 37 °C to ensure ideal conditions for the mammalian cell lines under study. The supernatant medium was exchanged every three to four days. For cultivation, the cell lines were grown in cell culture flasks (Greiner Bio-One GmbH, Kremsmünster, Austria) and placed inside a standard cell culture incubator (Heraeus BB15, Thermo Fisher Scientific Inc., Waltham, USA) at 37 °C, 5 % CO_2 and 95 % relative humidity. All cell lines were subcultivated at approximately 80 to 90 % confluency. During cultivation and before subcultivation, confluency and morphology of the cells were checked using a phase contrast microscope (Nikon Diaphot Inverted Phase Contrast Microscope, Nikon Instruments Europe, Amstelveen, Netherlands).

3.1.2 Cell Lines Under Study

In this work seven different cell lines were used. The culture medium differed for the individual cell lines. The formulations of the culture media are shown in *Table 2*. The cell lines under study are described in more detail in following paragraphs.

Madin and Darby originally isolated Madin Darby Canine Kidney (MDCK) cells from the kidney of a cocker spaniel in 1958. Several different subtypes of the MDCK cell line are currently persisting (Gaush et al. 1966). In this work two of these sublines, called MDCK-I and MDCK-II, were studied. Both strains represent epithelial cell cultures derived from the same parental cell line. MDCK-I cells originate from a low passage of the parental line and are generally associated with the formation of strong epithelial barriers, resulting in values for the transepithelial electrical resistance (TER) well over 1000 Ωcm^2. In addition, MDCK-I cells are characterized by a small size and appear in an overall flat morphology (Dukes et al. 2011). MDCK-II cells in contrast are bigger in size. Additionally, MDCK-II cells are known for the formation of moderately strong barriers with TER values in the range between 50 and 300 Ωcm^2 (Stevenson et al. 1988).

The subtype 52E of Normal Rat Kidney cells (NRK) was initially described in 1978 and has been derived from a parental NRK cell line isolated from the rat species *rattus norvegicus* (Larco and Todaro 1978). NRK-52E cells are characterized by a cobblestone morphology forming leaky monolayers with TER values below 10 Ωcm^2. The cell line was purchased from the *Deutsche Sammlung von Mikroorganismen und Zellkulturen* (DSMZ)

A549 cells are human lung adenocarcinoma type II alveolar epithelial cells, isolated from an explanted lung adenocarcinoma of a 58 year old male in 1972 (Giard et al. 1973). The cell line forms uniform monolayers with polygonal cell bodies. Similar to NRK cells, the monolayers are very leaky corresponding to very low TER values (Hermanns et al. 2004). A549 cells are constantly used in studies addressing the influence of substances on respiratory activity. The cell line was provided by Prof. Dr. Heilmann (Department of Pharmaceutical Biology, University of Regensburg).

The U373 MG (Uppsala) cell line is a human glioblastoma astrocytoma cell line which was isolated from an explanted malignant tumor (Pontén and Macintyre 1968). The cell line is characterized by a glial morphology. U373 MG cells were provided by Prof. Buschauer (Department of Pharmaceutical & Medicinal Chemistry, University of Regensburg).

Table 2: Formulation of cell culture media used for cultivation of the cell lines studied in this thesis.

Cell Line	**Basal Medium**	**FCS / vol %**	**Streptomycin / µg/mL**	**Penicillin / units/mL**	**Additional Supplements**
NRK-52E	Dulbecco's Modified Eagle's Medium (DMEM) 3.7 g·L^{-1} $NaHCO_3$ 4.5 g·L^{-1} D-Glucose	5	100	100	2 mM Glutamine
SK-Mel 28		10	100	100	2 mM Glutamine
MCF-7	Minimum Essential Medium Eagle (MEM) 2.2 g·L^{-1} $NaHCO_3$ 1 g·L^{-1} D-Glucose	10	100	100	2 mM Glutamine 1 mM Pyruvate
MDCK I & MDCK II		5	100	100	4 mM Glutamine
U373-MG		5	100	100	2 mM Glutamine
A549	Dulbecco's Modified Eagle's Medium (DMEM) (50 %) 3.7 g·L^{-1} $NaHCO_3$ 4.5 g·L^{-1} D-Glucose Nutrient Mixture F-12 Ham (50 %)	5	100	100	2 mM Glutamine

SK-Mel 28 cells are melanocytic cells isolated and established from skin tissue of a 51 year old male with a malignant melanoma in 1975 (Fogh et al. 1977). SK-Mel cells exhibit a polygonal cell shape forming epithelial-like monolayers. The cell line was purchased from the DSMZ.

Michigan Cancer Foundation-7 (MCF-7) cells are human adenocarcinoma cells established from a pleural diffusion of a 61 year old female suffering from a breast carcinoma (Soule et al. 1973). MCF-7 cells form epithelial like monolayers with a polygonal cell shape. The cell line was provided by Prof. Göpferich (Department of Pharmaceutical Technology, University of Regensburg).

3.1.3 Subcultivation Protocols

Subcultivation of cells was regularly performed using a standardized protocol. The protocol differed slightly depending on the cell line and is detailed in Table 3. After aspiration of the cell culture medium, the cells were treated with PBS^{--} to discard cell debris as well as Ca^{2+} and Mg^{2+} ions which play an important role for the formation of cell-cell and cell-matrix contacts. In order to detach the cells from the flask surface and from each other, some cell lines were first incubated with an EDTA solution in PBS^{--} (1 mM). Afterwards the cells were treated with trypsin, to disassemble cell-cell and cell-substrate contacts. The cells were then washed off the flasks using cell culture medium, which additionally inactivates the previously added trypsin. The solution containing the suspended cells was transferred to a Greiner tube and centrifuged. Centrifugation speed and time was cell type dependent (see Table 3). After centrifugation the supernatant medium was aspirated, and the cell pellet was resuspended in the respective cell culture medium. After resuspension the cell suspension was first diluted into cell culture flasks for further cultivation. Afterwards the cells were counted either using a *Bürker counting chamber* (Paul Marienfeld GmbH & Co. KG, Lauda Königshofen, Germany) or an automated cell counter (Countess 3, Thermo Fisher Scientific Inc., Waltham, USA).

Table 3: Subcultivation steps for individual cell lines used in this work. The given volumes are valid for a cell culture flask with a growth area of 25 cm^2.

	A549	**MDCK-II**	**MDCK-I**	**SK-Mel 28**	**MCF-7**	**U373**	**NRK**
1) 4 mL PBS^{--}	2x	2x	2x	2x	2x	2x	2x
2) 4 mL EDTA in PBS^{--} (1 mM, 10 min, 37 °C, 0 % CO_2)	-	1x	2x	-	-	-	1x
3) 1 mL trypsin in PBS^{--} (0.05 % (w/v), 10 min, 37 °C, 0 % CO_2)	1x	1x	1x c = 0.25 % (w/v)	1x	1x c = 0.25 % (w/v)	1x	1x
4) Digestion stopped by addition of 10 mL of the respective cell culture medium							
5) Centrifugation	110 x g 10 min	110 x g 10 min	110 x g 10 min	200 x g 5 min	200 x g 5 min	110 x g 10 min	110 x g 10 min
6) Resuspension in 4 mL of the respective cell culture medium							

After cell counting, the suspension was diluted to the desired cell density and seeded onto the substrate needed for the experiment. In this work, cells were either cultured on permeable filter substrates, on impermeable electrode surfaces or in 96-well agarose plates for spheroid formation (see chapter 3.1.4). The different cell-seeding densities are summarized in Table 4. Cells were grown on filters with an apical volume of the cell suspension of V_{apical} = 200 µL and a basolateral volume of pure cell culture medium of $V_{basolateral}$ = 850 µL. When regular culture plates were needed, a volume of V = 500 µL of the cell suspension was inoculated when using 24 well plates and a volume of V = 200 µL was added when working with 96 well plates.

Table 4: Cell densities for different cell types and culture substrates.

Cell Line	Type of culture Substrate	Density / cells·cm^{-2}
MDCK-I	permeable	$4.95 \cdot 10^5$
	impermeable	$4.5 \cdot 10^5$
MDCK-II	permeable	$4.95 \cdot 10^5$
	impermeable	$4.5 \cdot 10^5$
NRK	permeable	$4.95 \cdot 10^5$
	impermeable	$4.5 \cdot 10^5$
A549	permeable	$4.95 \cdot 10^5$
SK-Mel	permeable	$2.75 \cdot 10^5$
MCF-7	permeable	$3.3 \cdot 10^5$
U373	permeable	$3.3 \cdot 10^5$
	impermeable	$3 \cdot 10^5$

3.1.4 Cultivation of Tumor Spheroids

Spheroid formation was achieved by culturing suspended cells using the *liquid overlay technique*. Therefore, cells were seeded on a non-adhesive culture substrate, resulting in the assembly of spherical cell aggregates called spheroids. In this work, a standard 96-well flat bottom cell culture plate (Cellstar®, Greiner Bio-One GmbH, Kremsmünster, Austria) was coated with agarose dissolved in serum free cell culture medium (1.5 % (w/v), 50 µL/well, Sigma-Aldrich, St. Louis, MA, USA). Before addition to the wells, the agarose solution was heated using a microwave. Subsequently, the plate was cooled down to ensure the solidification of the agarose gel. The plates were pre-incubated at 37°C prior to cell-seeding and the cells were inoculated at the desired concentration. The loaded plates were incubated on an orbital shaker at 120 rpm for 4 h and for another 20 h at 50 rpm. Shaking was performed at 37 °C and 0 % CO_2 in a dry incubator. In order to prevent the plates from drying out during shaking, the plates were sealed with Parafilm® (Bemis Company Inc, Neenah, WI, USA). Additionally, cell culture medium was supplemented with HEPES buffer (4-(2-hydroxyethyl)-1-piperazineethane-sulfonic acid, 20 mM, Sigma-Aldrich, St. Louis, MA, USA) to ensure a stable and physiological pH at CO_2-free conditions. Spheroid growth and maturation was completed by an incubation period of 6 to 7 days in a standard cell culture incubator (37 °C, 5 % CO_2, 95 % relative humidity).

3.1.5 Composition of Buffers and Solutions

Experiments were generally performed in Leibovitz L15 medium (Sigma-Aldrich, St. Louis, MA, USA). Depending on the experiment, L15 medium was supplemented with different additives. Antimycin A (5 mM), Malonoben (10 mM) and Cytochalasin D (10 mM) were stored as stock solution in DMSO at -20 °C and freshly diluted in the measurement buffer to a working concentration of 2 µM, 100 nM and 5 µM, respectively. Glucose was supplemented from a stock solution in PBS^{++} (250 $g \cdot L^{-1}$) to obtain a working concentration of 4.5 $g \cdot L^{-1}$.

3.2 Impedance Analysis

3.2.1 Basic principles of impedance-based cell monitoring

The theory of impedance-based cell sensing has already been discussed in detail elsewhere. The paragraph below provides a short summary of the theoretical background (Stolwijk and Wegener 2019).

Theoretical background of impedance

In systems working with alternating currents (AC) a sinusoidal voltage U(t) is applied. Using Euler's formula, the voltage can be described as follows:

$$U(t) = U_0 e^{i\omega t}$$

where:

$$\omega = 2\pi f$$

with $i^2 = -1$, U_0 describing the voltage amplitude, ω the angular frequency, t the time and f the applied frequency.

Application of this sinusoidal voltage results in a current I(t) which can be described similarly as:

$$I(t) = I_0 e^{i(\omega t - \varphi)}$$

The quantity φ describes the phase difference between U(t) and I(t) and becomes zero for an ideally resistive system.

Following Ohm's Law results in the impedance Z for AC-systems:

$$Z = \frac{U(t)}{I(t)} = \frac{U_0}{I_0} \cdot e^{i\varphi} = |Z| e^{i\varphi}$$

Where $|Z|$describes the magnitude of the impedance.

In an alternative notation, the complex impedance is described through its imaginary and the real part:

$$Z = |Z| cos\varphi + i|Z| sin\varphi = Re(Z) + iIm(Z) = R + iX$$

The real part (Re) is also described as resistance R, whereas the imaginary part (Im) is termed reactance X.

Impedance-based cell monitoring

Cellular impedance monitoring can be used to monitor cells with label-free, non-invasive means and with high time-resolution. In general, the cells are cultured on top of or in between two or more electrodes, an alternating current is applied, and according to the theories above, the impedance of the system is determined. In this system, cells act as an additional barrier within the current path, characterized by a distinct impedance footprint. So far, two main possibilities to study cellular impedance have been developed: (A) The cells are cultured directly on the surface of thin-film gold electrodes deposited on impermeable substrates or (B) the cells are cultured on permeable substrates, also called filter inserts, applied between an apical and a basolateral electrode (Figure 3). Approach (A) is sensitive to a broad range of different cell types independent from their barrier forming nature. Additionally, it can be easily applied to higher throughputs. However, culturing cells on permeable substrates offers a closer emulation of the biological scenario in comparison to the impermeable counterpart. Even more so, for many assays targeting permeability and cellular polarity it is essential to culture cells on permeable substrates. In addition, certain cell types need permeable substrates to fully develop polarized phenotypes.

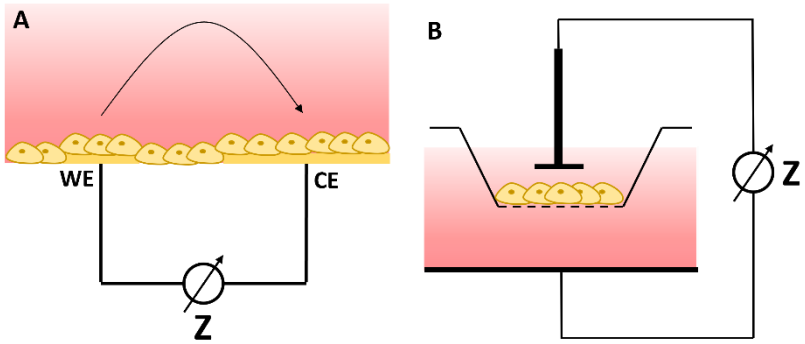

Figure 3: Established approaches to measure cellular impedance. (A) Cellular impedance monitoring of monolayers cultured directly on the surface of thin film gold electrodes (ECIS). (B) Impedance Sensing of cell monolayers cultured on permeable substrates.

3.2.2 Electric-cell-substrate impedance sensing (ECIS)

In Electric cell-substrate impedance sensing (ECIS) cells are grown directly on top of a set of thin-film electrodes deposited on standard cell culture substrates (Lukic and Wegener 2005). The applied low amplitude AC current can pass the cell layer by different pathways. Strongly dependent on the sensing frequency, the current can either flow through the paracellular cleft or directly through the cell. In the frequency range used for ECIS, the cell membrane can be approximated as a capacitor, which results in high impedance values at low frequencies, (< 1 kHz) forcing the current to flow around the cells. As a consequence, at lower frequencies the

state of the cell-cell and cell-substrate contacts are assessable in more detail. However, at higher frequencies (> 10 kHz), the current can couple capacitively through the cell membrane, leading to a measurement of the impedance representing the cell body (Stolwijk and Wegener 2019).

ECIS can be performed in various measurement modes depending on the question being addressed. In this work, the multi frequency / time mode (MFT) was used for characterization of the electrode layouts of CIS-TER as well as the determination of the appropriate sensing frequencies for the cell lines under study. In MFT mode, the impedance is measured over a broad range of frequencies ranging from 1 Hz to 100 kHz resulting in the maximum information regarding cell morphology, cell-cell and cell-substrate contacts. However, MFT suffers from poor time resolution (~ 15 – 20 min). If higher time resolution was of essence, measurements were performed in the single frequency / time mode (SFT). In SFT mode, only a single frequency is applied, resulting in a much higher temporal resolution (~ 4 min). In order to ensure the sensitivity of the frequency with respect to the cell line under study, the sensitive frequency had to be determined beforehand in a MFT measurement. The sensitive frequency is strongly dependent on the electrode setup and most importantly on the cell type under study (Wegener et al. 2000).

In this work, the concept of electric-cell-substrate impedance sensing was applied to the CIS-TER setup which is explained in more detail in chapter 3.2.4.

3.2.3 Real time monitoring of transepithelial electrical resistance (TER)

To determine barrier forming properties of cells cultured on permeable substrates, the filters are sandwiched between a basolateral electrode and an electrode in the apical liquid compartment. Impedance was then determined by applying an alternating voltage with an amplitude of 50 mV at distinct frequencies in the range between 1 Hz and 100 kHz while measuring the resulting current. The impedance was determined for each frequency at every time-point, leading to the time-resolved detection of impedance spectra. Impedance spectra were analyzed by an equivalent circuit to the raw data. Therefore, the different parts of the experimental system (electrodes, filter, cells, medium) are described by impedance elements within an electrical circuit (Figure 4). The different parts of such a typical circuit are shortly described in the following paragraph. The constant phase element (CPE) describes the impedance of the interface of the electrode and the buffer, whereas the impedance contribution of the medium is described by R_{med}. The properties of the filter substrate as well as the cell layer itself can both be best described by a parallel connection of a resistor and a capacitor. Hence, the characteristics of the filter system are described by R_{Ins} and C_{Ins}. The properties of the cell layer are defined

by C_{Cl} and by R_{Cl}, which are referred to as the transepithelial electrical capacitance (TEC) and the transepithelial electrical resistance (TER). The following transfer function of the electric circuit is now used to determine the individual parameters through fitting procedures:

$$Z(\omega) = R_{bulk} + \frac{1}{\frac{1}{R_{Cl}} + i\omega C_{CL}} + \frac{1}{\frac{1}{R_{ins}} + i\omega C_{ins}} + \frac{1}{(i\omega)^n A}$$

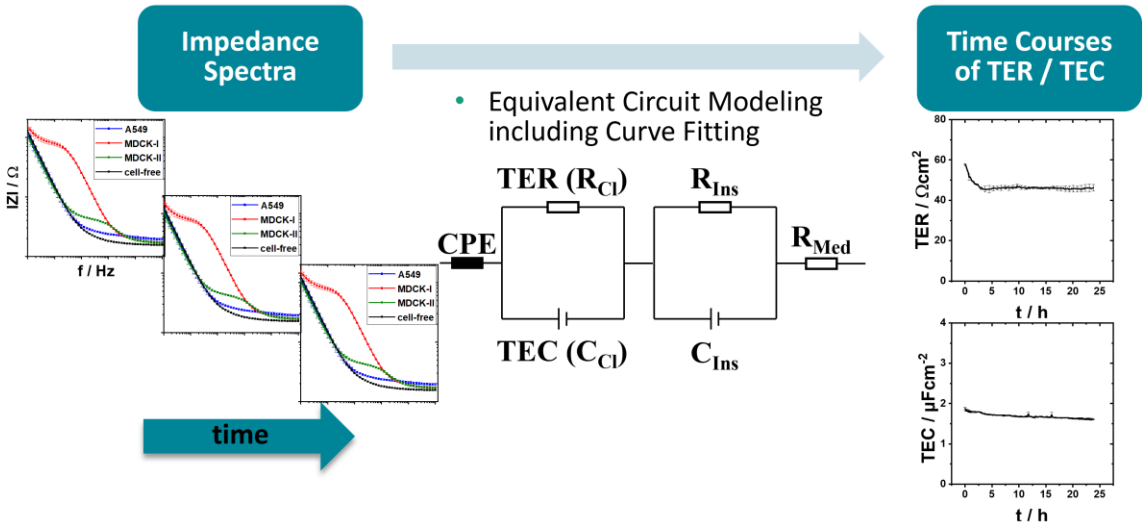

Figure 4: Data evaluation of time resolved impedance spectra using equivalent circuit modeling. Impedance spectra can be used to determine time courses of the transepithelial electrical resistance (TER) and the transepithelial electrical capacitance (TER). TER and TEC are calculated via equivalent circuit modeling considering each part of the experimental setup as part of an electrical circuit. Apart from cellular parameters this approach results in the parameters CPE, R_{med}, R_{ins} and C_{ins} which describe the interface of electrode and buffer, the bulk resistance of the buffer and the electrical parameters of the porous inserts, respectively.

In this work TER and TEC were determined with the help of three different systems:

i) cellZscope®,

ii) TER-Ox and

iii) CIS-TER.

The cellZscope® 3 device is commercially available and state of the art for online monitoring of TER values. The device consists of a cell module, a docking station, and a controller unit (Figure 5). Inside the cell module, the apical dipping electrodes are fixed to the lid of the cell module with magnetic mount and the basolateral pot electrodes are screwed onto the bottom part of the cell module. The electrodes are completely made up of stainless steel. For measurements, the cell module and the docking station were placed inside a standard cell culture incubator at the desired conditions. The combination of both was connected to the controller placed outside of the incubator. Measurements were controlled via the cellZscope®

software. Hardware and software have been provided by nanoAnalytics GmbH (Münster, G). To perform cellZscope® experiments the filters were transferred to the pot electrodes of the device. Impedance spectra of the system were recorded continuously over defined periods. During the measurement the device remained in a standard cell culture incubator at the desired temperature, CO_2 content and humidity.

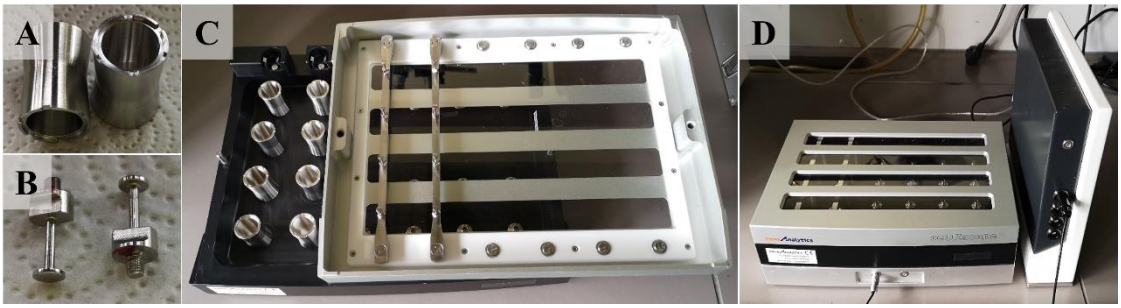

Figure 5: cellZscope® 3 hardware. (A) basolateral pot electrodes (B) apical dipping electrodes (C) cell chamber with partly integrated basolateral and apical electrodes (D) completed setup with the controller and the base plate.

The newly developed setups of TER-Ox and CIS-TER are explained in more detail in chapters 3.4 and 3.2.4, respectively. Both systems were developed in the course of this thesis and combine TER readings with secondary readouts.

3.2.4 CIS-TER: Experimental Setup

The CIS-TER platform combines both previously described approaches of measuring the cellular impedance in a single setup (Figure 7 A). Therefore, the CIS-TER mode was implemented in both, the hardware and the software of the cellZscope® M with the help of nanoAnalytics GmbH. In comparison to the standard cellZscope® 3 device, the basolateral setup consists of a set of two thin-film gold electrodes instead of the stainless-steel pot electrode used in the standard cellZscope® 3 setup. The thin-film gold electrodes were deposited on a Lexan® plate (provided by nanoAnlytics GmbH) and the final electrode plates were glued to a polymer block with twelve wells in the size of a well in a 24 well culture plate completing the basolateral CIS-TER plate. Each well had the correct size and height to additionally hang a filter substrate above the basolateral electrode layout. The cell module and the docking station of the cellZscope® M device were adjusted to the polymer blocks serving as basolateral vessels instead of the stainless-steel pot electrodes used in the cellZscope® 3 device (Figure 6). The docking station was designed to hold two cell modules at the same time enabling simultaneous monitoring of twenty-four wells. The apical electrode was introduced similarly to the cellZscope® 3 from the lid of the cell module. Instead of the magnetic bars used in the cellZscope® 3 device, the bars holding the dipping electrodes were screwed to the lid.

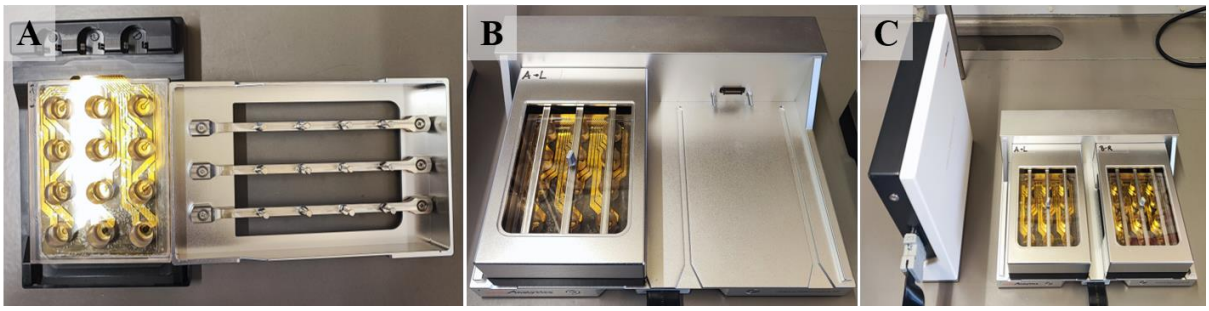

Figure 6: cellZscope® M hardware. (A) Cell module holding the basolateral electrode block containing the basolateral thin-film gold electrodes and the lid of the cell module holding the apical dipping electrodes (B) Docking station holding one of the cell modules. (C) Completed setup of the cellZscope® M device consisting of the controller unit, the docking station and two cell modules containing the electrode blocks.

To find a well performing electrode setup two different electrode designs were analyzed (Figure 7 D). The first design consisted of a set of two circularly interdigitated electrodes (BE1, A_{total} = 0.25 cm^2). The interdigitated electrode bars are 150 µm wide and 200 µm apart. Interdigitated electrodes offer the possibility to gain information over a larger surface area. However, larger electrode areas are correlated with lower impedance signals and decreased sensitivity (Zhang et al. 2017). This is important when working with cells characterized by weaker impedance footprints. To overcome this issue, a second layout was designed consisting of a single circular working electrode (d = 250 µm, A = 0.049 mm^2) and a larger horseshoe counter electrode (BE2, A = 0.8 cm^2). The impedance of this system is now determined only by the cells growing on the small working electrode, strongly increasing sensitivity of the setup, ideally suited for low-impedance cell monolayers. To obtain the final, small electrode size of the circular electrode, the originally deposited circular gold structure (d = 3 mm, A = 7 mm^2) was reduced in size by photolithographic processes. The photolithography was performed by Stefanie Michaelis, Fraunhofer EMFT, using a mask specifically manufactured for the CIS-TER setup (compugraphics Jena GmbH, Jena, Germany).

The novel setup allowed to choose between several modes using the cellZscope® M, by depending on the activation of different electrode combinations:

i) **TER-mode**: Electrodes 1 and 2 are connected in parallel as one basolateral electrode and are connected against electrode 1; the TER of the cell layer cultured on the porous substrate is monitored (Figure 7 B yellow cell layer).

ii) **CIS-mode**: Electrodes 1 and 2 are connected against each other; electrode 3 is not used; the basolateral cell layer is monitored (Figure 7 C brown cell layer).

iii) **CIS-TER-mode**: CIS- and TER-mode are combined in subsequent measurements for each time point; Impedance of both cell layers is monitored.

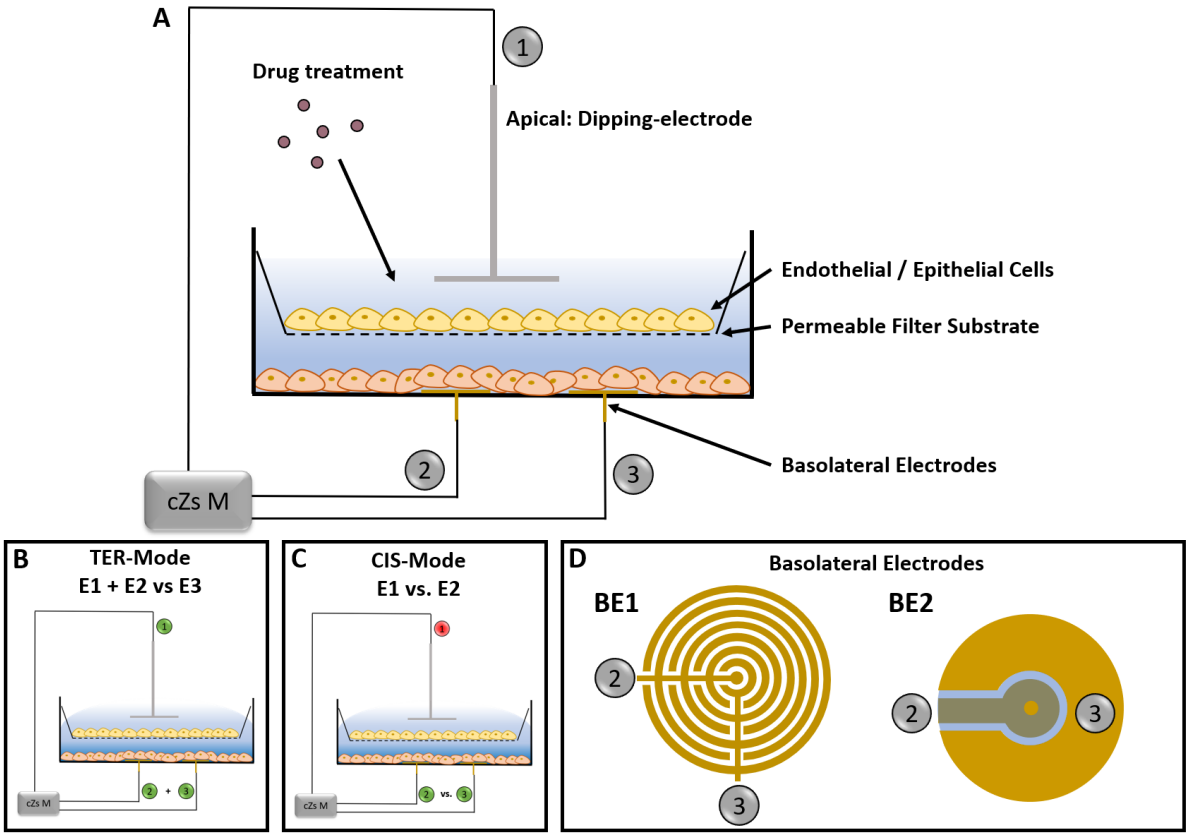

Figure 7: (A) Schematic setup of the CIS-TER platform. (B) Schematic illustration of the TER-Mode. Electrodes 1 and 2 are connected in parallel as one basolateral electrode and are connected against electrode 1 (C) Electrodes 1 and 2 are connected against each other. Electrode 3 is not used. (D) Different layout options for basolateral electrodes. Electrode 1 represents the apical dipping electrode. Electrodes 2 and 3 represent the two basolateral electrodes. In the case of the interdigitated layout, the electrodes are equally sized. In the small electrode setup, electrode 2 represents the small working electrode and electrode 3 the bigger horseshoe counter electrode.

Before the inoculation of the cells onto the electrodes, the plates were treated in an argon plasma for 30 s to ensure sterility and increase the hydrophilicity of the electrode surface. After cell seeding, the plates were kept under the airflow cabinet for approximately 15 minutes to prevent an inhomogeneous distribution of the cells on the electrode layout by convection. Afterwards, the plates were moved into a standard cell culture incubator (37 °C, 5 % CO_2, 95 % relative humidity). After 24 h, the medium in the wells was renewed. The medium was refreshed again after 48 h and the measurements were started. Substances were added after a baseline measurement of approximately 1- 2 h. An exception was made in measurements assessing cell adhesion. Here, the measurement was started directly after cell inoculation. Prior to inoculation, a baseline of the cell-free electrode in medium was recorded until stable impedance values were obtained, the measurement was paused for cell seeding and finally continued after the cells were seeded on the electrodes.

3.3 Ratiometric Optical Imaging

3.3.1 Theoretical Background

The use of luminescence for ratiometric optical imaging has been described in detail before and the following chapter provides a short summary of the theoretical background (Lakowicz 2006; Schmittlein 2018). Ratiometric optical fluorescence imaging is based on the emission of light by one or more excited molecules called luminophores. The emission of light is known as *photoluminescence* and is divided into two different sub-processes called *fluorescence* and *phosphorescence*. The processes occurring in luminophores can be depicted in a *Jablonski Diagram* as shown in Figure 8. Absorption of light by a luminophore leads to its excitation from the electronic ground level S_0 to an electronically excited state such as S_1 or S_2. Each of the electronic states is further divided into several vibrational states. After excitation, the luminophore undergoes internal conversion processes, leading to the relaxation towards the vibrational ground state of the electronically excited state S_1. Further relaxation from the ground state of the S_1 level can occur in three different options (Itoh 2012). The first option is a relaxation to the ground level by emission of light in a process known as *fluorescence*. A second option for the direct relaxation back to S_0 is *quenching*. However, *quenching* can only occur under the presence of a molecule, called quencher, with fitting electronical states. *Quenching* leads to a transfer of energy to the quencher. The quencher itself is excited and its relaxation occurs without the emission of light. The third option is a spin forbidden process called *intersystem crossing* which ultimately leads to an electronical triplet state T_1. The relaxation of the luminophore to the ground level S_0 from this state is called *phosphorescence*. Similar to fluorescence, phosphorescence is quenchable by a suitable quencher.

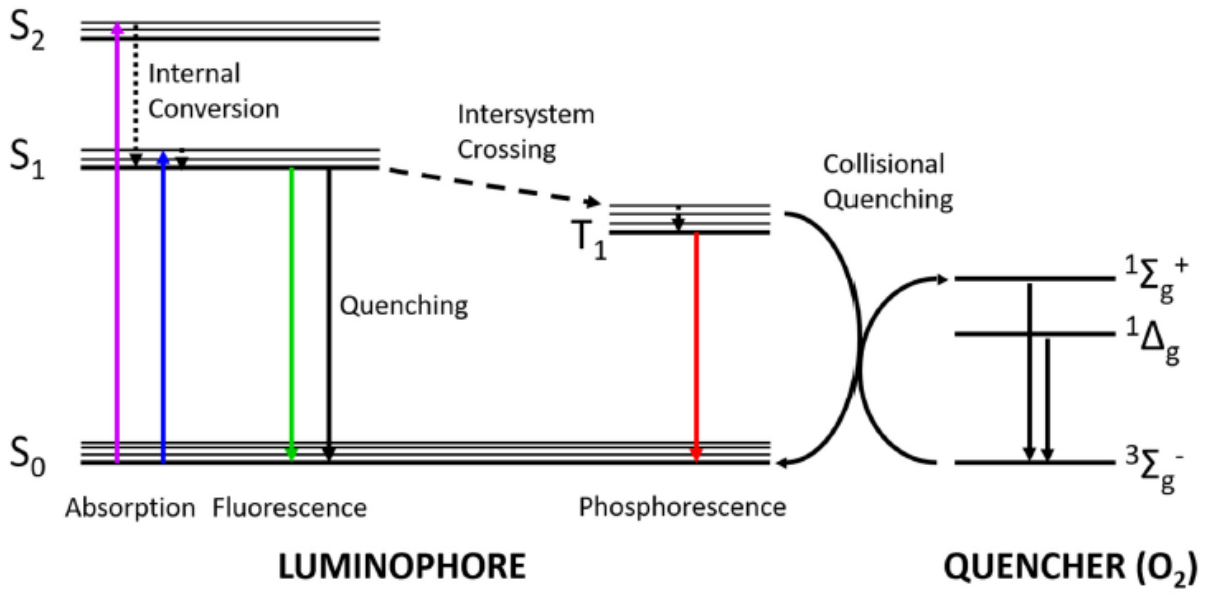

Figure 8: Jablonski Diagram depicting the processes taking place in a luminophore upon optical excitation. Adapted from Schmittlein 2018.

Ratiometric optical imaging as it is performed in this work is based on the application of two fluorophores with different sensitivities of their luminescence to the presence of an analyte. One luminophore is called *sensing fluorophore* and its intensity is altered by the presence of the analyte, while the intensity of the second fluorophore is not influenced by the analyte. This second luminophore is called *reference fluorophore* (Figure 9 A). In consequence, the ratio of both fluorophores provides a ratiometric signal which can be correlated to the respective analyte concentrations. In comparison to only using the alterations of the sensing fluorophores intensity upon analyte concentration changes, the ratiometric approach offers several benefits. Most importantly, the use of ratiometric signals enables self-referencing, minimizing effects of instruments, sample-matrix and variations of external parameters in the surrounding medium of the cells (Yang et al. 2023). This can improve accuracy, precision as well as reproducibility of the analyte quantification resulting in an overall less error prone analytical tool (Madhu et al. 2023).

Oxygen in its triplet ground state ($^3\sum_g^-$) is a collision quencher of phosphorescence of the sensing fluorophore, altering the measured intensity of this fluorophore in a concentration dependent manner (Figure 9 B). During the process, triplet oxygen takes up the energy from the triplet state T_1 of the luminophore. Following the energy transfer, oxygen is either converted to the first ($^1\Delta_g$) or second ($^1\sum_g^+$) excited state of singlet oxygen (Wilson 1992). Singlet oxygen has a very short lifetime of about 3 µs (Hatz et al. 2007) and relaxes back to the triplet form by vibrational processes without emission of visible light (see Figure 8, Vanderkooi et al. 1987).

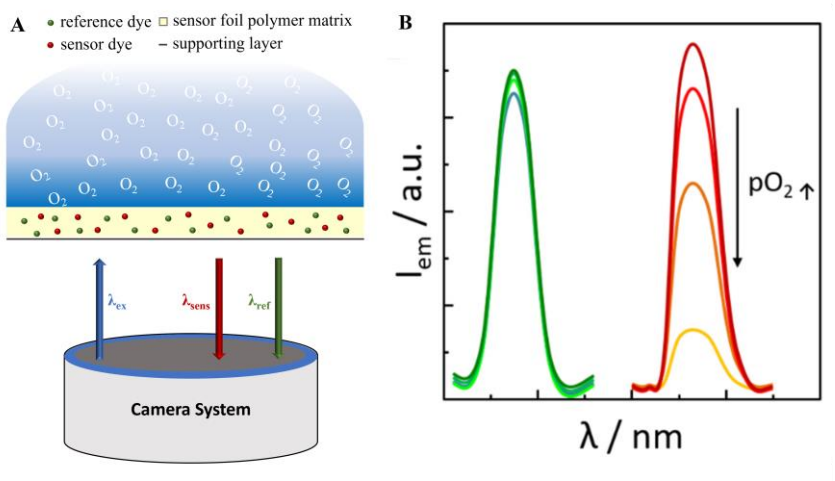

Figure 9: Principle of ratiometric optical oxygen imaging as used in this work. (A) Schematic illustration of ratiometric optical oxygen imaging. (B) Intensity changes of the **reference fluorophore** and the **sensing fluorophore** with the analyte concentration. Adapted from Schmittlein 2018.

Ratiometric pH sensing is performed by capitalizing on the reversible interaction of a fluorophore with H^+-ions (Schreml et al. 2011). At high H^+-concentrations and therefore low pH values, the sensing fluorophore is protonated, leading to differences in emission characteristics such as fluorescence lifetime and intensity. These changes can again be determined with concentration dependency.

3.3.2 Commercial setup for Oxygen and pH Imaging

In this work, a commercial setup was used for ratiometric optical oxygen and pH sensing. The VisiSens TD system (PreSens Precision Sensing GmbH, Germany) is made up of a camera system, an LED ring, and an optical lens. The LED ring and the optical lens are mounted with the help of a tube that fits the respective lens. In this work three different lenses combined with two different tubes have been used (see Figure 10). The applied lenses had different magnification factors and field of views resulting in varying resolutions. The following lenses were used in this thesis:

i) lens set “VisiSens TD area i”
ii) lens set “VisiSens TD area ii”
iii) lens set “VisiSens TD mic”

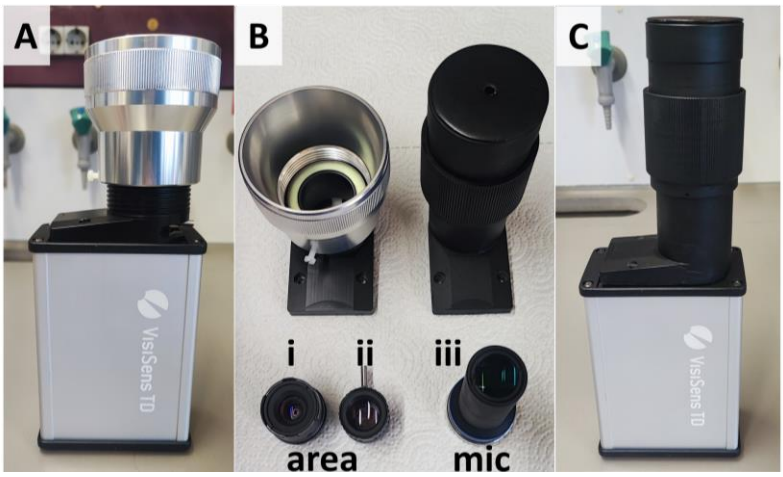

Figure 10: VisiSens TD system and lenses used in this work. (A) Completed VisiSens TD setup with tube for area lenses. (B) Possible combination of tubes and lens systems. (C) Completed VisiSens TD mic setup.

Lenses i) and iii) are commercially available from PreSens GmbH. Objective i) can be used for monitoring large field of views between 4 x 3 cm^2 and 8 x 6 cm^2 (1292 x 946 pixels) resulting in a low-resolution image, whereas lens iii) offers a 2x magnification and can be used to record high resolution images of smaller field of views of 2064 x 1540 μm^2 (1292 x 946 pixels). Objective ii) was purchased during the course of this thesis and provides an intermediate solution with a field of view of 15.69 x 12.55 mm^2 (1292 x 946 pixels, CS2325ZM01, ArduCam, Hong Kong). The culture vessel was placed directly on top of the respective tube (area or mic, see Figure 10 B). The cell culture vessel was previously equipped with a sensor foil glued to the bottom of the vessel using biocompatible silicon glue. Before further treatments the plates were stored in the dark for approximately 24 h to ensure full drying of the silicon glue. Sensor foils for oxygen (SF-RPSu4) and pH (SF-HP5R) were provided by PreSens Precision Sensing GmbH. Before use, sensor plates were treated with an argon plasma for 1 min.

3.3.3 Calibration of Sensor foils

Oxygen sensor foil:

The oxygen sensor foil was calibrated via a 2-point calibration at 0 % and 100 % dissolved oxygen saturation. Therefore, the sensor foil was first flooded with an oxygen saturated solution of the measurement buffer representing 100 % oxygen saturation or 149.3 torr partial oxygen pressure at 37 °C. The second solution was deprived of oxygen by the addition of sodium sulfite ($NaSO_3$, 10 g/L) to the respective measurement buffer. Sodium sulfite reacts with the oxygen present in the buffer solution (Yagi and Inoue 1962). This buffer is then used as 0 % oxygen or 0 torr calibration solution. For both solutions a picture was taken using the snapshot function of the measurement software. The luminescence ratio was determined using the VisiSens

Scientifical software by choosing the region of interest on the sensor spot that needed to be calibrated. If more than one sensor spot of sensor foil was present in a single field of view, each sensor spot was calibrated individually by choosing several regions of interest.

pH sensor foil:

The pH sensor foil was calibrated using solutions of the measurement buffer with six different pH values (5.5, 6, 6.5, 7, 7.5, 8). The pH was adjusted with the help of a pH electrode (SenTix® 41, Xylem Inc, Washington D.C., USA). The solutions were subsequently applied to the sensor and the sensor spot was washed once with the respective pH solution before the snapshot was taken. The luminescence ratios were then determined as described above for oxygen sensor foil calibration.

3.3.4 Data evaluation process for ratiometric optical imaging

The data evaluation process for both analytes was very similar and is demonstrated exemplary for oxygen in Figure 11. The measurement resulted in micrographs taken by the camera of the VisiSens TD system. All pictures were further analyzed by building the ratio of the red and the green channel representing the emission of the *sensing fluorophore* and the *reference fluorophore*. After a noise correction, performed via the VisiSens Scientifical software, and the application of the respective calibration data, the time resolved oxygen and pH maps were determined. These maps were further analyzed by a time-stack analysis of certain regions of interest, resulting in the respective time courses. The same procedure was applied to determine pH maps and pH time courses. For pH measurements, the linear decrease of pH with time was used to calculate the extracellular acidification rate (EAR) in units of mpH·min^{-1} as follows:

$$pH = EAR \cdot t + pH(t = 0)$$

Similarly, to determine the apparent oxygen consumption rate (AOCR) of the cells from oxygen time courses, the linear decrease within the first hour of the measurement was used:

$$pO_2 = AOCR \cdot t + pO_2(t = 0)$$

The resulting AOCR had the unit torr·h^{-1} and was converted to amol·(s·cell)$^{-1}$ with the help of the volume within the measurement system. AOCR was normalized to the number of cells seeded at the beginning of the experiment.

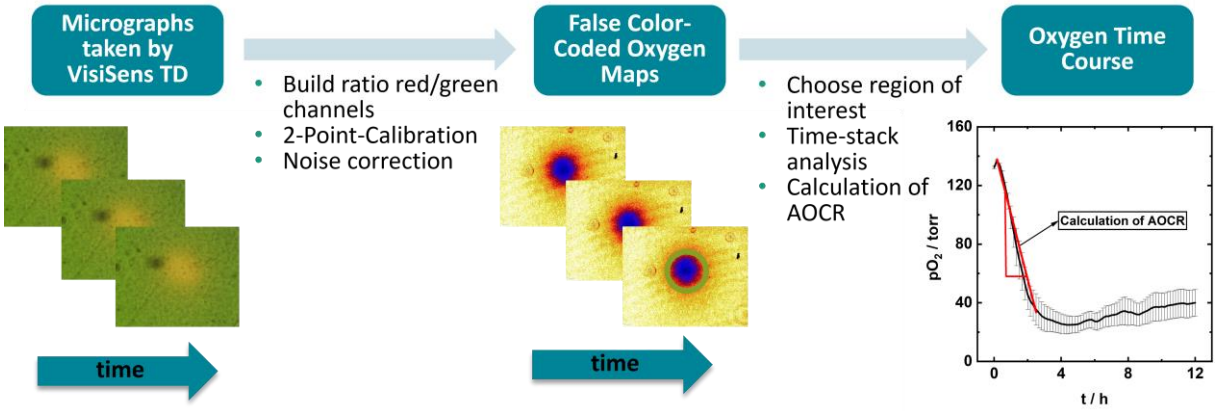

Figure 11: Time-resolved data evaluation process for ratiometric optical oxygen imaging. Extracellular acidification rates are determined similarly using false color-coded pH maps. Adapted from (Naber et al. 2025).

A second approach for the quantification of cellular oxygen consumption was the calculation of the oxygen consumption rate (OCR) which relies on the equilibrium value of the partial pressure of dissolved oxygen. For OCR calculation the value of pO_2 at t = 2 h was used. The empirical equilibrium value was inserted in following equation described by Mamchaoui and Saumon (Mamchaoui and Saumon 2000):

$$OCR = \frac{-D \cdot S \cdot [pO_2(h) - pO_2(0)]}{h}$$

With: D: diffusion coefficient of O_2 in water at 37 °C: D = $3.3 \cdot 10^{-5}$ $cm^2 s^{-1}$

S: cell-covered area of the substrate

α: solubility coefficient of oxygen in water at 37 °C: α = 0.94 µmol·cm^{-3}·atm^{-1}

h: height of the medium column

$pO_2(h)$: Oxygen partial pressure at the position of the cell layer at t = 2 h (measured)

$pO_2(0)$: Oxygen partial pressure at the air/medium surface: $pO_2(0)$ = 149.3 torr.

In addition to the time-resolved analysis of oxygen consumption and pH modulation, the oxygen and pH maps of spheroids were further employed to determine lateral oxygen and pH profiles (Figure 12). Therefore, a rectangular region of interest with a defined width of 12 pixels was placed across the recorded micrograph and the resulting map. Subsequently, the lateral distribution of oxygen and pH within this region of interest was determined along r. The lateral profiles were smoothed using a 20-point Savitzky-Golay smoothing of order 2. The resulting profiles were used to determine the oxygenation and the pH levels within 3D tissue models such as spheroids or organoids. Lateral pH profiles were identified using the same steps.

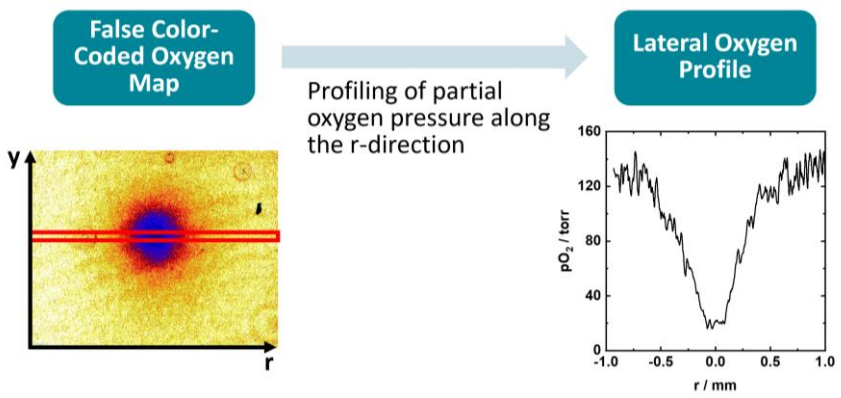

Figure 12: Spatial data evaluation process for ratiometric optical imaging. False color-coded oxygen maps are analyzed by placing a rectangle with a width of 12-pixels across the map. Partial oxygen pressure values are then profiled along the r-direction resulting in lateral oxygen profiles. Lateral pH profiles are determined similarly using false color-coded pH maps.

In order to combine both, the spatial and the temporal information measured for spheroids, the aerobic profile and the anaerobic profile were developed for a more in-depth analysis of oxygen uptake and extracellular acidification, respectively. The data evaluation process providing the aerobic profile is shown in Figure 13. Therefore, two partial oxygen pressure values were extracted from the lateral oxygen profile at positions $r^0 = 0$ mm and $r^+ = 0.1$ mm. These values were then subtracted from the partial oxygen pressure in ambient air $pO_2 = 149.3$ torr at 37 °C to obtain the respective values $\Delta pO_2(0)$ and ΔpO_2 (0.1). In addition, the width of the profile at half of $\Delta pO_2(0)$ was determined (FWHM). The portray of these values alongside the apparent oxygen consumption rate, representing the temporal resolution of the approach, in a spider web plot resulted in the aerobic profile. The spatial information for the anaerobic profile was prepared similarly using the lateral pH profile of the system under study. pH values were extracted at the same positions as described for the oxygen profiles and later subtracted from a pH value of pH = 7.4 resulting in $\Delta pH(0)$ and $\Delta pH(0.1)$, respectively. Furthermore, the width of the profile at half of $\Delta pH(0)$ was calculated. Combination of the three values with the extracellular acidification rate in a spider web plot resulted in the anaerobic profile of a spheroid. In both cases, a polygon enclosing a bigger area resulted from a higher respiratory activity or a stronger acidification of the extracellular environment.

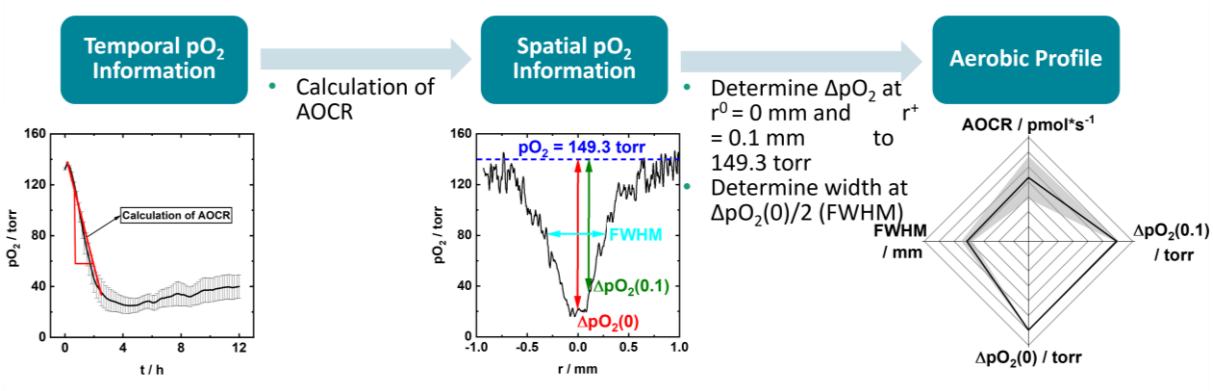

Figure 13: Determination of the aerobic profile combining spatial oxygen information and temporal information on partial oxygen pressure of a 3D cell model. Temporal information is represented by the apparent oxygen consumption rate. Spatial information is represented by the difference of partial oxygen pressure to 149.3 torr at two distinct positions (r = 0 mm and r = 0.1 mm) of the lateral oxygen profiles ($\Delta pO_2(0)$ and $\Delta pO_2(0.1)$) as well as the full width at half maximum (FWHM). Anaerobic profiles are determined similarly.

3.4 TER-Ox: Experimental Setup

The newly developed setup of the TER-Ox platform alongside most of the data measured using TER-Ox assays (presented in chapter 6) were published throughout the course of this thesis (Naber et al. 2025).

The TER-Ox setup was developed to combine ratiometric oxygen mapping and impedance spectroscopic characterization of cells cultured on permeable substrates (Figure 14). The assay platform consists of a novel cell chamber designed with the help of the in-house machine shop (Department of Chemistry and Pharmacy, University of Regensburg), the VisiSens TD system for oxygen imaging, a relay and a Solartron impedance analyzer (SI 1260, Solartron Analytical, Farnborough, UK). At the current state, the different measurement modes required individual operating systems and were therefore run on two computers. The VisiSens TD system and the measurement chamber were placed inside a dry incubator at 37 °C and 0 % CO_2.

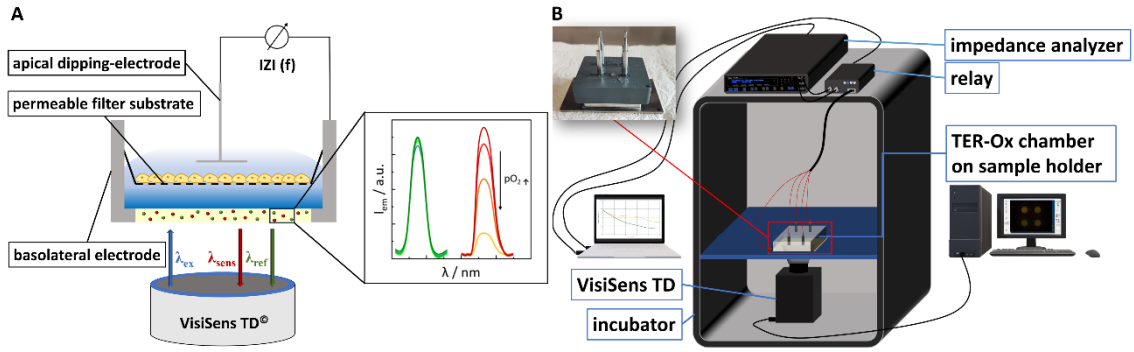

Figure 14: Setup of the TER-Ox assay. (A) Schematic setup of the TER-Ox approach combining impedance spectroscopy and ratiometric imaging. (B) Combined setup of the TER-Ox approach including all required devices. Adapted from (Naber et al. 2025).

The center piece of the TER-Ox platform is the measurement chamber (Figure 15 E). The chamber consists of a basolateral chamber and a lid with incorporated apical dipping electrodes. The basolateral part is made up of four individual layers. The first layer is a stainless steel (l = 5.6 cm, w = 8.7 cm, h = 1.9 mm) base serving as a support for the entire chamber. This supporting plate has four circular holes (d = 1.6 cm) serving as optical windows needed to perform optical oxygen imaging. The second layer is an optically transparent Lexan® plate (l = 5.6 cm, w = 8.7 cm, h = 0.5 mm, type 8010 MC colorless 112 polish, alt-intech) carrying four circular spots of the oxygen sensitive sensor foil. The sensor spots are glued onto the Lexan® plate in positions matching the optical windows of the supporting layer using biocompatible silicon glue (RS Components Ltd., United Kingdom). On the top of the Lexan® plate we apply a second stainless-stell plate with a thickness of approximately 100 µm matching the thickness of the sensor foil. The outer dimensions are again matching the size of the base

plate. In addition, the plate has four circular openings at the dimensions and position of the four oxygen sensor spots. This ensures the contact of the oxygen sensor foil to the measurement buffer. To complete the basolateral setup, we fix a stainless-steel block (l = 5 cm, w = 5 cm, h = 1.645 mm) with four cylindrical openings to the bottom plate. Together with the stainless steel plate, the openings serve as basolateral fluid compartement and basolateral pot electrode. To prevent leakage out of the chamber or between the four wells, the contact areas between the stainless-steel plate and the Lexan® plate as well as the stainless-steel plate and stainless-steel block, are sealed using a layer of silicon fat (KORASINOL-Paste, Kurt Obermeier GmbH & co. KG) and a silicon rubber (l = 5 cm, w = 5 cm, h = 1 mm, Product-Nr.: 240000100, Technischer Handel Straub), respectively (Figure 15 A & B).

The apical part completes the setup. It holds four individual dipping electrodes necessary for impedance measurements across the cell layer while also serving as a lid. Therfore, we designed a PVC lid with four drill holes. The holes are postioned in the center of the cavities of the basolateral chamber and are used to fix the stainless-steel dipping electrodes (d = 4.5 mm) glued into the drill holes using biocompatible silicon glue (Figure 15 C and D).

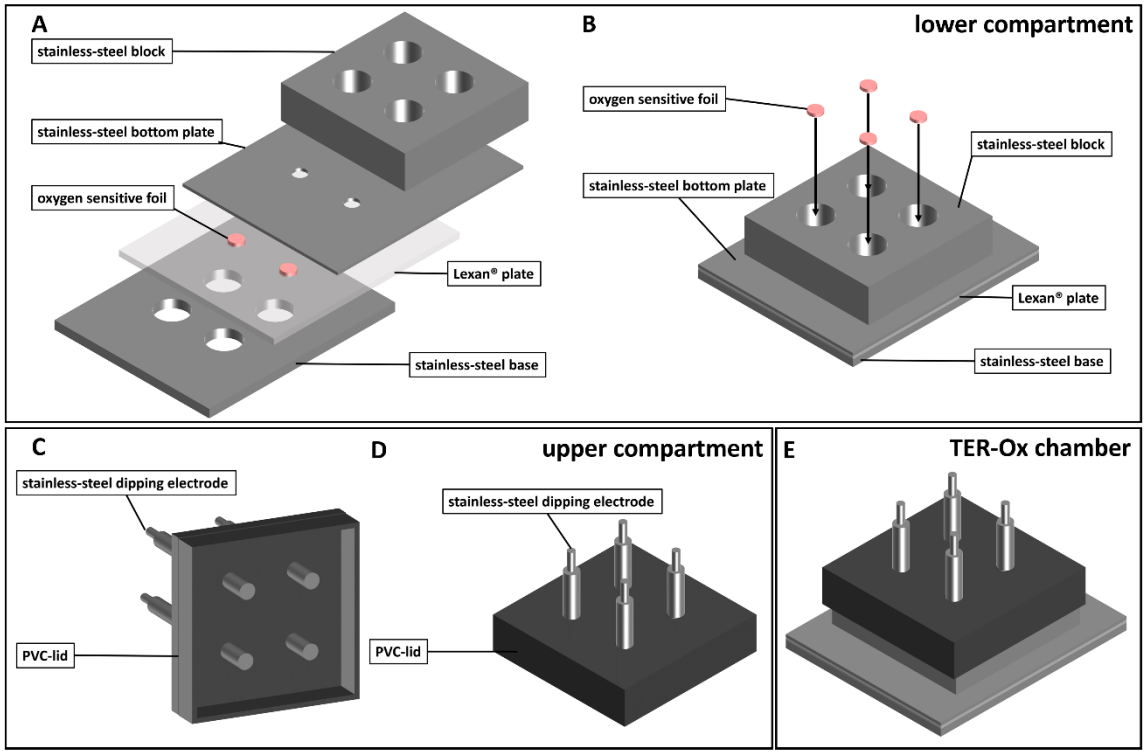

Figure 15: Assembly of the novel TER-Ox measurement chamber. (A) Different layers of the basolateral chamber setup: Stainless-steel base for support; Lexan® plate with circular openings filled with spots of a commercial oxygen sensor foil; stainless-steel plate and stainless-steel block serving as basolateral pot electrode. (B) Fully assembled basolateral part of the chamber. (C) Bottom view of the apical part of the chamber, consisting of a PVC lid and four individually addressable stainless-steel dipping electrodes. (D) Top view of the apical part of the chamber. (E) Fully assembled TER-Ox chamber. Adapted from (Naber et al. 2025).

TER and TEC analysis used a numerical algorithm coded in MATLAB® by Prof. Dr. Joachim Wegener. The algorithm is based on the theories described in chapter 3.2.3. Oxygen images were recorded and evaluated using the VisiSens TD system and software as described in chapters 3.3.2 to 3.3.4.

For TER-Ox assays cells were seeded on filters as previously described. The filters were applied to the wells of the TER-Ox chamber and baselines were measured. After stable baseline values of the TER measurement, substances with well-defined biological impact on the cells under study were added to the apical compartment of the filter substrate and the measurement was continued.

4 Ratiometric Optical Oxygen Imaging of 3D cell culture models

Previous studies in our laboratory have demonstrated the feasibility of monitoring oxygen consumption of spheroids using ratiometric optical oxygen imaging (Schmittlein 2018; Pütz 2022; Frank 2023). Therefore, the spheroids were grown directly on the surface of the oxygen sensor. The following chapter will focus on extending ratiometric optical imaging to spheroids cultured on permeable filter substrates (Figure 16). Culturing spheroids on permeable substrates enables spheroids to be transferred to additional sensors for subsequent analysis of several parameters, increasing the obtained information on the spheroid.

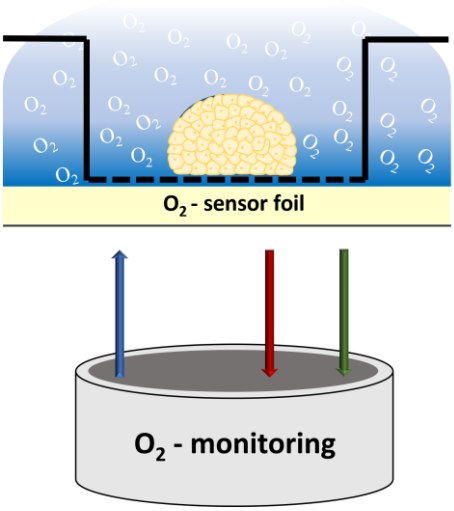

Figure 16: Ratiometric optical oxygen imaging of spheroids cultured on permeable filter substrates.

4.1 General Remarks on Oxygen Profiling

4.1.1 Validation of assay platform using finite element analysis

The use of the assay platform to determine oxygen profiles across tumor spheroids has already been discussed and validated in detail in cooperation with a theoretical PhD project conducted in our working group. Most important aspects are summarized below (Frank 2023). The validation was performed using finite element modeling. Finite element modeling (FEM) and other in silico approaches can be used to predict oxygen profiles and distributions within complex cell culture models (Materi and Wishart 2007). FEM can consider the physical principles behind oxygen mass transport in liquids and tissues as well as respiratory oxygen consumption. The model was fed with literature data found for oxygen diffusion in media and in tissue, represented by the tumor spheroid in the experiments, the dissolution of oxygen at the air-liquid interface as well as oxygen consumption rates of the applied cell lines. The OCRs were measured previously in experiments using 2D cell layers of the relevant cells. Furthermore, the model also considered the morphology change of the spheroids from a

spherical shape to an elliptical shape upon attachment onto the sensor foil. The alterations of the spheroids' shape were determined using confocal laser scanning microscopy. We used this mathematical model based on FEM to show, that the oxygen footprint measured by ratiometric optical imaging correctly depicts the oxygen distribution within a non-attached, "floating", and therefore completely spherical tumor spheroid. The experimental oxygen profiles were determined using VisiSens TD mic. To generate spheroids, two cancer cell lines, MCF-7 and U373 cells, were cultured for 6 days using the liquid overlay technique (chapter 3.1.4). After spheroid formation, the spheroids were transferred to the oxygen sensitive sensor foil. They were cultured for another 24 h to attach to the polymer foil. Subsequently, the profiles were monitored for several hours. Figure 17 shows the overlap between oxygen profiles determined experimentally at t = 2 h of the measurement with the VisiSens TD mic setup and the profiles calculated via finite element modeling. The results showed that the oxygen distributions obtained from oxygen maps measured using optical imaging were in good agreement with the mathematical model for both cell lines at four different spheroid sizes generated by varying the seeding densities. In experimental and theoretical studies, oxygen levels decreased towards the center of the spheroids at r = 0 µm in a similar manner. The minimum oxygen levels were consistent between experimental data and in-silico approach for both cell lines and the different seeding densities. The width and the minimum values of the lateral oxygen profiles were dependent on the seeding density and hence on the size of the spheroids. These results were in line with expectations described in literature: The oxygen uptake of the outer cell layers cannot be compensated by the diffusion of oxygen from the periphery to the center of the tumor spheroid, leading to a deprivation of oxygen in the center of the spherical aggregates. The bigger these aggregates, the stronger is the deprivation of oxygen. These trends have already been shown before using invasive methods (Mueller-Klieser and Sutherland 1982). It is therefore valid to conclude, that oxygen distribution measured using the two-dimensional sensor principle of this work correctly depict the oxygen distributions within the 3D cellular aggregate.

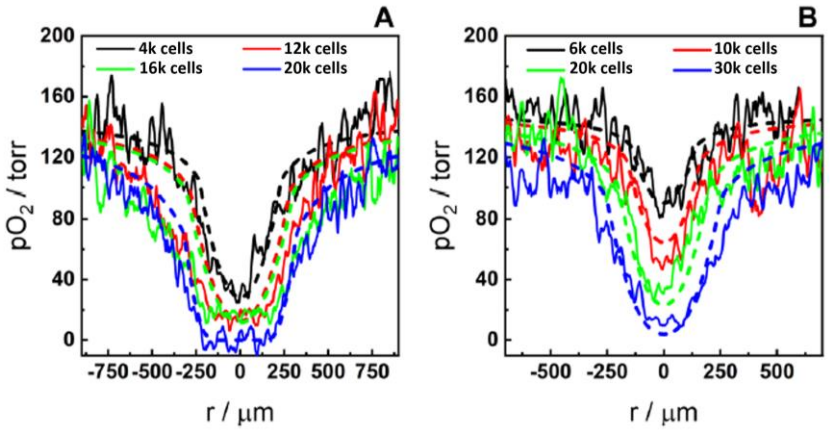

Figure 17: Comparison of lateral pO_2 gradients within tumor spheroids determined experimentally by VisiSens TD mic and the in-silico approach finite element modeling. Oxygen profiles of MCF-7 spheroids (A) and U373 spheroids (B) with different seeding densities at time point t = 1 h after the start of the measurement. r represents the lateral distance from the center of the tumor spheroid at r = 0 µm. Solid lines represent the experimental data, dashed lines represent results obtained from FEM. The spheroids were grown using the liquid overlay technique for 6 days and were transferred to the oxygen sensor foil. After an additional 24 h culture period on the sensor foil for spheroid attachment, the oxygen profiles were measured using VisiSens TD mic. Experiments were performed in a dry cell culture incubator at 37 °C and 0 % CO_2 (adapted from Frank 2023).

4.1.2 Determination of oxygen consumption rates – a comparison

As described in chapter 3.3.4, oxygen consumption rates can be determined by two fundamentally different approaches. Determination of the *apparent oxygen consumption rate* (AOCR) is based on the linear decline of partial oxygen pressure time course, whereas the calculation of the *oxygen consumption rate* (OCR), is based on the equilibrium partial oxygen pressure in the medium at t = 2 h of the measurement. Both options were described in detail in chapter 3.3.4. The following chapter presents consumption rates from two individual experiments conducted in the course of this thesis and compares the possible ways for quantifying the cellular oxygen consumption. In addition to the slope of the linear decline in the first hour of the measurement, calculation of the AOCR requires the medium volume of the system. For determination of the oxygen consumption rates, the distance between the spot where the partial oxygen pressure is determined and the air-liquid interface where the maximum partial oxygen pressure is present is needed.

Quantification of oxygen consumption of 2D monolayers

In this thesis we used two different methods to place the filters relative to the sensor foil, resulting in different values AOCR or OCR, respectively. In a first approach, cell monolayers were seeded onto the filters and the filters were hanging above the sensor foil (Figure 18). This resulted in the formation of a gap volume V_{gap} and a gap height x. Using this volume for the AOCR calculation and this distance for OCR calculation leads to the $AOCR_{gap}$ and the OCR_{gap} values. In addition to these possibilities, two more scenarios for the calculation of the

consumption rates are possible. In case of the AOCR the whole volume of the medium filled dish V_{max} (Figure 18 orange box) might be taken into account, resulting in the $AOCR_{max}$ value. Furthermore, only the volume of medium in the gap and the liquid volume in the filter above the cells might be considered, resulting in the volume V_{fil} (Figure 18 green box) and the respective consumption rate $ACOR_{fil}$. For the calculation of the OCR, either the distance between the sensor foil surface where the partial oxygen pressure was measured and the air-liquid interface (h) or the distance between the filter membrane (almost equal to the cell surface) and the air liquid interface (d) can be applied. These two options introduce the values described as OCR_{max} and OCR_{fil}.

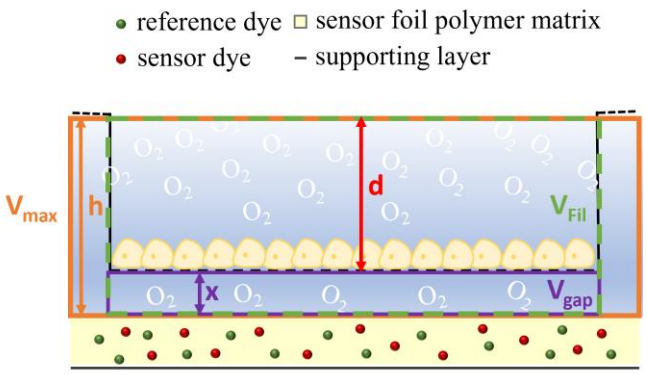

Figure 18: Different volumes and distances needed for the calculation of OCR and AOCR values for cells cultured on a filter substrate hanging above the sensor surface.

Figure 19 shows a comparison between the differently determined *oxygen consumption rates* and the *apparent oxygen consumption rates* described above. The data was taken from a TER-Ox experiment shown later in this thesis (Figure 56). In the experiment, MDCK-II cells were treated with malonoben which strongly enhances the oxygen consumption of cells or with antimycin A which shuts down oxygen consumption. The biological background of these influences on the cells will be discussed in detail in chapter 6.2.1. Culture of the cells under control conditions in L15 buffer, resulted in values of 4.6 ± 0.2 $amol \cdot (s \cdot cell)^{-1}$, 4.4 ± 0.2 $amol \cdot (s \cdot cell)^{-1}$ and 93 ± 3 $amol \cdot (s \cdot cell)^{-1}$ for OCR_{max}, OCR_{fil} and OCR_{gap}, respectively. Comparing the different values of the oxygen consumption rates for control conditions, it is obvious that the use of the gap distance to determine OCR_{gap} resulted in over 20-fold higher consumption rates compared to the rates found for the two remaining distances. Considering that the cells did not only have excess to the oxygen dissolved in the medium in the gap volume but also to the medium above the cells, it can be concluded that the use of the gap height alone is not meaningful to determine the OCR correctly as this approach neglects oxygen which is dissolved in the culture medium in the apical compartment of the filter. The values found by application of the gap height are therefore not trustworthy and will not be further considered in

this work. Calculation of OCR_{fil} and OCR_{max} did not result in significant differences. This is plausible as the difference between the two distances d and h is smaller than 5 %. The effect of malonoben treatment on the OCR values was only very marginal resulting in only slightly increased values of 4.80 ± 0.07 amol·(s·cell)$^{-1}$, 5.08 ± 0.07 amol·(s·cell)$^{-1}$, 103 ± 1 amol·(s·cell)$^{-1}$ for OCR_{max}, OCR_{fil} and OCR_{gap}, respectively. The shutdown of oxygen uptake upon AntA addition and the resulting decrease in the consumption rate was correctly in the different parameters regardless of the calculation method of the OCR with values of 0.6 ± 0.2 amol·(s·cell)$^{-1}$, 0.7 ± 0.2 amol·(s·cell)$^{-1}$, 13 ± 4 amol·(s·cell)$^{-1}$ for OCR_{max}, OCR_{fil} and OCR_{gap}, respectively. Calculation of OCR values relies on the use of equilibrium pressures of oxygen. Treatment of cells with malonoben however mainly influenced the initial decrease of oxygen due to oxygen consumption rather than the equilibrium state (Figure S 12). This resulted in the missing increase of the OCR values upon malonoben addition.

Calculation of the AOCR values resulted in a different trend within the different calculation possibilities. The highest values for cells cultured in the L15 control were found for the volume V_{max} (129 ± 4 amol·(s·cell)$^{-1}$) followed by V_{fil} (25.0 ± 0.8 amol·(s·cell)$^{-1}$) and V_{gap} (10 ± 0.3 amol·(s·cell)$^{-1}$). As already described above, cells also had access to oxygen which is dissolved in the medium above the cells. Therefore, the use of V_{gap} is also inappropriate for AOCR calculation. At first glance, the most plausible way to calculate the AOCR would be the use of the volume V_{max}. However, we were able to show in a previous thesis that the influence of the oxygen dissolved in the medium outside of the filter in the basolateral compartment on the dissolved oxygen in the gap is marginal within at least the first 12 h of the measurement (Figure S 1 (Frank 2023)). For calculations in this thesis, oxygen values within a maximum of 3 hours of experimental time were used. Within this time period, the cells most likely did not consume any of the oxygen dissolved in the medium surrounding the filter and the use of V_{max} would overestimate the available oxygen to the cells. Therefore, it is more reliable to use the volume V_{fil} for calculations of the AOCR. In contrast to the OCR values, the calculated AOCR values correctly depicted the increase of oxygen consumption after malonoben treatment with an increase of around 50 % regardless of the calculation approach. The addition of antimycin A resulted in an increase in oxygen partial pressures. However, for AOCR calculations the linear decrease initiated by cellular oxygen consumption is needed for the analysis. Hence, AOCR values for these samples could not be calculated and the values for these samples had to be set to 0 amol·(s·cell)$^{-1}$.

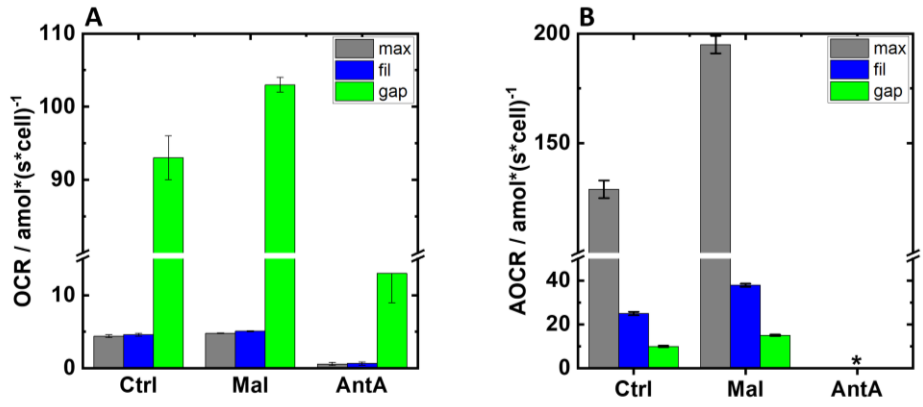

Figure 19: Comparison of different options to quantify oxygen consumption of cells cultured on filters hanging above the sensor foil. (A) Oxygen consumption rates calculated using the equilibrium partial oxygen pressure. (B) Apparent oxygen consumption rates calculated from the linear decrease of partial oxygen pressure time course in the beginning of the measurement. Data were recorded using the TER-Ox setup in a dry cell culture incubator at 37 °C and 0 % CO_2 (Mean ± SEM, n = 3).

The values of the $AOCR_{fil}$ found for the MDCK-II cells cultured under control conditions were in line with values found in literature (see also chapter 6.1.1) whereas the values of OCR_{max} resulted in lower values and the $AOCR_{max}$ in much higher values than reported in literature (Wagner et al. 2011). Therefore, for experiments using this setup, the $AOCR_{fil}$ will be used to quantify the rate of oxygen consumption.

Quantification of oxygen consumption of spheroids

For the oxygen measurements of the spheroids, the filters were placed directly on the sensor foil surface (Figure 20). In comparison to the system above this measurement approach did not lead to the formation of a measurable gap height between sensor foil and filter. Here, OCR values were exclusively calculated using the distance between the surface of the filter and the air-liquid interface (d), which is referred to as OCR_{fil}. However, it must be stated, that the used distance is not different to the distance between the sensor and the air-liquid interface (h), meaning that the calculation of the OCR cannot distinguish between OCR_{fil} and OCR_{max} in this case. To determine the apparent oxygen consumption rates two volumes can be considered – the overall volume V_{max} (Figure 20 orange box) and the apical volume within the filter substrate V_{fil} (Figure 20 green box).

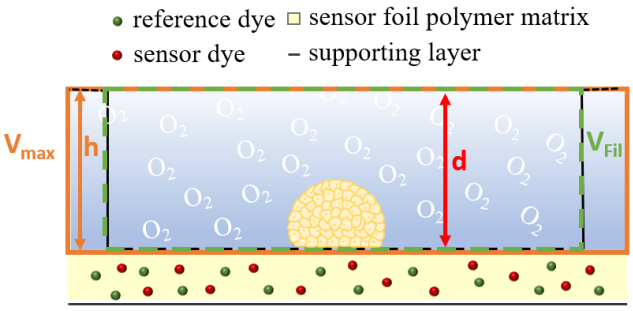

Figure 20: Different volumes and distances needed for the calculation of OCR and AOCR values of spheroids cultured on a filter substrate in direct contact to the sensor foil surface.

The results for the differently calculated consumption rates are depicted in Figure 21. The data originate from an experiment monitoring an MCF-7 spheroid cultured on a permeable filter substrate treated with malonoben (enhancing oxygen consumption) and antimycin A (impeding oxygen consumption). The biological relevance of this experiment will be discussed in detail in chapter 4.2.4 Figure 29. Interestingly, the OCR_{max} value did again not increase as expected for malonoben treated spheroids. OCR calculation resulted in values of 2.8 ± 0.1 pmol·s^{-1} and 2.9 ± 0.1 pmol·s^{-1} for spheroids cultured in L15 and for spheroids treated with malonoben, respectively. In contrast the calculated apparent oxygen consumption rates correctly depicted the expected trend. Values for both $AOCR_{max}$ and $AOCR_{fil}$, increased more than 2-fold. Reduction of oxygen consumption by AntA addition was correctly measured using the OCR_{max} as the value for spheroids treated with antimycin A was reduced to 0.18 ± 0.09 pmol·s^{-1}. The calculation of AOCR values for cells treated with AntA was again not possible as the treatment led to an increase in partial oxygen pressure. Therefore, as already explained above the values were set to 0 pmol·s^{-1}. Similar to the observations for the experiments with cell monolayers, the $AOCR_{max}$ values were overall higher than the values found for the $AOCR_{fil}$. Without gap volume below the filter, there is almost no possibility for the cells to consume the dissolved oxygen in the medium surrounding the filter in the basolateral compartment. Accordingly, the AOCR is again best determined by using the $AOCR_{fil}$.

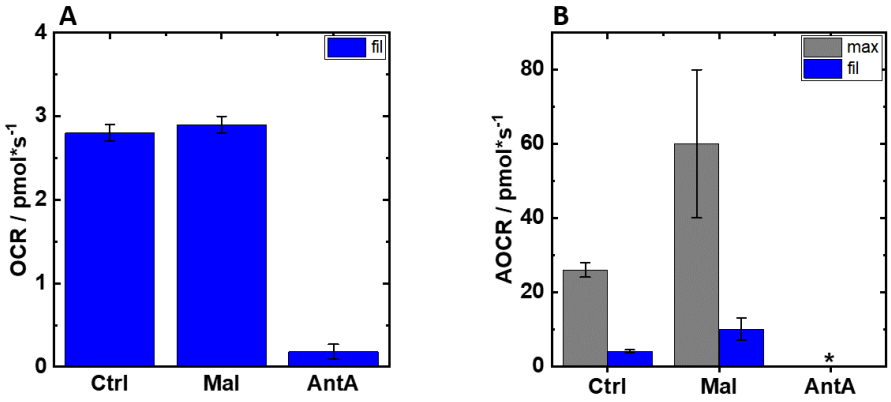

Figure 21: Comparison of different options to quantify oxygen consumption of MCF-7 spheroids cultured on filters standing directly on the sensor foil surface. (A) *Oxygen consumption rates* calculated using the equilibrium partial oxygen pressure. (B) *Apparent oxygen consumption rates* calculated from the linear decrease of partial oxygen pressure time courses in the first hour of the measurement. Data were recorded using the VisiSens TD mic setup in a dry cell culture incubator at 37 °C and 0 % CO_2 (Mean ± SEM, n = 3).

Summarizing the results shown in this chapter it can be stated that the two most reliable ways to quantify the oxygen consumption in the applied systems were the OCR_{fil} and the $AOCR_{fil}$. OCR_{fil} resulted in values of 2.8 ± 0.1 pmol·s^{-1} and the $AOCR_{fil}$ of 4 ± 0.4 pmol·s^{-1}. Both values were slightly higher than reported values found in literature. Mukomoto et al. determined oxygen consumption rates for MCF-7 spheroids seeded with a cell number of $10 \cdot 10^3$ cells using scanning electrochemical microscopy resulting in values of around 0.9 pmol·s^{-1} (Mukomoto et al. 2020). However, the spheroids seeded in this work were seeded with a cell number of $20 \cdot 10^3$ cells. Considering these differences in cell number, the values are comparable for both calculation approaches. The calculations made to determine the OCR rely on an equation which was derived for a cellular system cultured on an impermeable substrate (Mamchaoui and Saumon 2000). In this work, the cells were cultured on permeable substrates, resulting in a more complex distribution of oxygen as well as diffusion dynamics of oxygen which are not considered in the OCR equation. As quickly described above the special geometry of the filter setup impedes the free diffusion of oxygen within the system. The gap height between cells on the filter membrane and the sensor surface is either small (hanging filter) or not measurable at all (filter directly placed on the sensor foil surface) and therefore hinders the oxygen diffusion from the basolateral medium surrounding the filter to the cells. Considering these influences and the results found for 2D monolayers cultured on permeable substrates, the following chapters of this work will rely on the use of $AOCR_{fil}$ for quantification of the cellular oxygen consumption. Additionally, the $AOCR_{fil}$ will be referred to as AOCR in the following chapters.

4.2 Mapping of oxygen profiles underneath tumor spheroids cultured on porous supports

As demonstrated in the previous chapter and in prior experimental studies conducted in our group, ratiometric optical oxygen imaging can be employed to assess lateral oxygen profiles across tumor spheroids that are directly in contact with the sensor foil. The following chapters will show that this method is also applicable to tumor spheroids cultured on permeable substrates. Culturing tumor spheroids on permeable substrates offers the possibility to not only measure oxygen profiles but in addition, profiles of other analytes on the same biological model upon transfer to a different sensor surface (see chapter 5.2.3).

4.2.1 Influence of the porous support on oxygen profile

In the first set of experiments, the influence of the permeable substrate on oxygen profiling via VisiSens TD mic was tested. Therefore, MCF-7 and U373 tumor spheroids were cultured on four differently porous filter substrates (Table 5). The polymer supports mainly differed in their porosity ε calculated as follows:

$$\varepsilon = r_{pore}^2 \cdot \delta_{pore} \cdot \pi$$

with r_{pore}: radius of the pore and δ_{pore}: the density of the pore.

The various filters were placed onto the sensor plate 24 hours after the spheroids were added to the porous substrates. For the measurement, the filters were positioned directly on top of the sensor foil glued into a 12-well cell culture plate (TPP Techno plastics Products AG, Trasadingen, Schweiz) instead of the usual hanging position. Setting the filters on the sensor film offered the closest possible contact between spheroid and sensor.

Table 5: Material characteristics of porous filter substrates used to determine the influence of the filter supports on imaging of oxygen profiles of tumor spheroids.

filter type (abbreviation)	filter material	pore size d / µm	pore density δ / pores/cm^2	porosity ε / %	membrane thickness d / µm
Sabeu CellQart (SFtl0.4)	PET	0.4	$1.0 \cdot 10^8$	12.6	11.5
Sabeu CellQart (SFtl1.0)	PET	1.0	$2.0 \cdot 10^6$	1.6	11
Sabeu CellQart (SFtl3.0)	PET	3.0	$2.0 \cdot 10^6$	14.1	12
Sabeu CellQart (SFtp0.4)	PET	0.4	$2.0 \cdot 10^6$	0.3	11.5

Oxygen profiles found for MCF-7 spheroids formed with a cell number of $2 \cdot 10^4$ cells are compared in Figure 22. Different filter types holding spheroids of the same size were compared to a spheroid placed directly on the sensor surface. In general, the lateral oxygen profiles (Figure 22 A) showed the expected u-shaped trajectory. As already described in chapter 4.1.1, partial oxygen pressure decreased towards the center of the spheroid. However, the decrease was differently pronounced for spheroids cultured on the various porous substrates. The worst overlap between spheroids cultured on filter substrate and spheroids directly attached to the sensor foil surface was detected for the SFtp0.4 filters. The polymer membrane in these filters has the lowest porosity of the tested filter substrates (ε = 0.3 %). The dissolved oxygen present on the basolateral side of the membrane, in the buffer within the small gap between filter and sensor surface, may not be sufficiently accessible for the cells grown on the apical side of the membrane. The diffusion of oxygen through the membrane is obviously strongly hindered and the profiles were not describing the oxygenation of the spheroid correctly. It is expected that an increased porosity should increase the alignment of profiles measured for spheroids cultured on porous substrates and the direct approach. This assumption was valid for SFtl1.0 and SFtl0.4 with porosities of 1.6 % and 12.6 %, respectively. Monitoring of spheroids cultured on filter type SFtl1.0 resulted in stronger oxygen depletion towards the center of the profile (60 to 70 torr) than found for spheroids grown on the SFtp0.4 filters, which resulted in oxygen levels around 100 torr in the center of the profile. However, the use of SFtl1.0 did not result in an overlap with the data obtained for spheroids cultured directly on the sensor surface. The lateral oxygen profiles measured for spheroids loaded on the even more porous SFtl.04 filters (ε = 12.6 %) were in good agreement with the direct approach with minimum oxygen levels

around 30 torr. Considering the assumption, that the decisive factor is the porosity of a membrane alone, monitoring of spheroids cultured on SFtl3.0 should also correctly reproduce the lateral oxygen profiles. As the membrane in these filters has an even higher porosity $\varepsilon = 14.1$ % than membranes in SFtl0.4 filters. However, the results showed that monitoring of the spheroids cultured on SFtl3.0 filters resulted in a weaker oxygen deprivation. The profile showed a smaller width and higher oxygen levels in the center, between 40 torr and 50 torr, than expected after measuring with the direct approach. This trend is confirmed by the oxygen maps depicted in Figure 22 B. This suggests that the approach is not mainly limited by the porosity which considers the size and the density of the pores but is rather predominantly determined by the density of the pores. The pore density found in SFtl0.4 filters is 50-fold bigger than δ_{pore} of the other filter types. In other words, a big pore size combined with a relatively low pore density can result in a high porosity, which may not be sufficient to ensure an accurate measurement of oxygen distributions using an imaging approach that strongly relies on spatial resolution. A second factor could be the thickness of the supporting polymer membrane. While SFtl0.4 filter membranes have a thickness of $d = 11.5$ µm, SFtl3.0 filters are slightly thicker with $d = 12$ µm. However, this difference is minimal and likely did not contribute to the variations in the oxygen profiles to the extent observed. To estimate the difference in diffusion time of oxygen through the pores of the membranes with different pore thickness, the random walk model was considered. The model describes the statistical distance a particle following Brownian motion can travel in a certain amount of time. Even though the model does not consider concentration differences as well as the nature of the pores, it can be used to estimate the influence of the membrane thickness on the result of the measurement. The following equation describes the mean squared displacement $<x(t)^2>$ of such a particle in a one-dimensional system:

$$< x(t)^2 >= \int_{-\infty}^{\infty} x^2 \cdot dx \cdot P(x) = 2 \cdot D \cdot t$$

With D as the diffusion coefficient and t the time.

The equation can now be used to determine the time needed for oxygen to diffuse through a pore of the membrane. The diffusion coefficient for oxygen in water at 37 °C was set to $2.89 \cdot 10^{-5}$ $\mu m^2 \cdot \mu s^{-1}$ (Xing et al. 2014). Solving the random walk model for time t resulted in values of 0.19 s for the SF0.4tl filters with a thickness of 11.5 µm and a time of 0.21 s for SFtl3.0 filters with a thickness of 12 µm. Considering that the fastest time resolution used for oxygen monitoring in this work was 5 mins and the lateral oxygen profiles shown in this work

were taken 2 h after measurement start, the differences of these filters could not have resulted from the different membrane thicknesses.

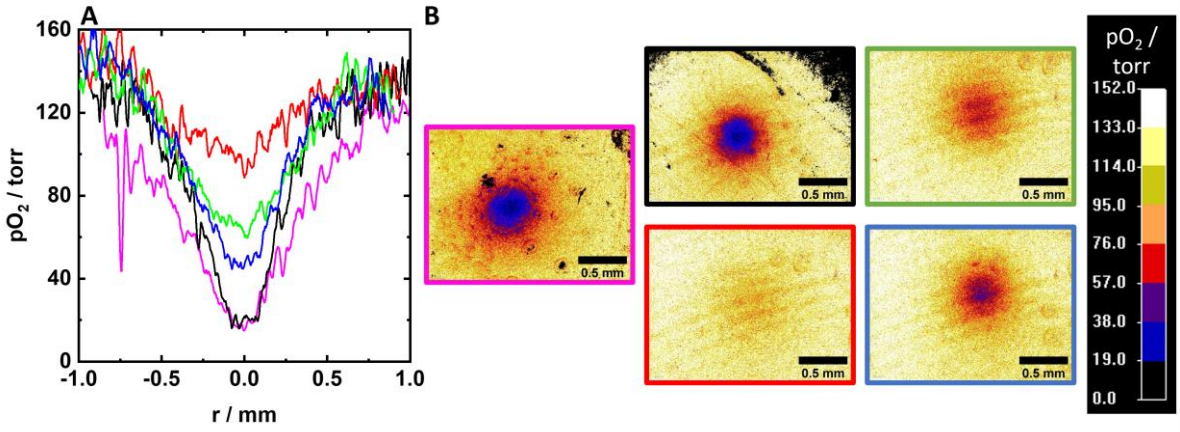

Figure 22: Dependency of lateral oxygen profiles of MCF-7 spheroids on porous membrane characteristics. Lateral profiles of partial oxygen pressure (A) and oxygen distribution maps (B) at t = 2 h after measurement start of MCF-7 spheroids. Scalebar: 0.5 mm. MCF-7 cells were seeded at a cell number of $20 \cdot 10^3$ cells at d = 0 and cultivated for 6 days using the liquid overlay technique. After cultivation, spheroids were transferred to filter substrates with different polymer membranes (no filter, SFtl0.4, SFtl1.0, SFtl3.0 and SFtp0.4) in L15 buffer (+ 1 % penicillin/streptomycin). 24 h after transfer, filters were applied directly on the sensor surface and oxygen profiles were measured for several hours using VisiSens TD mic. The experiments were performed in a dry cell culture incubator at 37 °C and 0 % CO_2.

To validate the results found for MCF-7 spheroids, spheroids of a second cell line, U373, were investigated. The trends found for MCF-7 tumor spheres also held true for the U373 spheroids (Figure 23). Spheroids cultured on SFtl0.4 filters resulted in lateral oxygen profiles that are in good agreement with the direct approach, while the lateral oxygen profiles for spheroids cultured on filters with lower pore density showed a less pronounced lateral oxygen profile. Partial oxygen pressures in the center of the spheroid ranged from 10 torr to 25 torr for the direct approach and for spheroids attached to SFtl0.4 substrates. The center oxygen levels for spheroids cultured on filters with lower pore density were significantly higher. Monitoring of spheroids on SFtl3.0 filters reached minimum oxygen levels around 60 torr, and spheroids grown on SFtl1.0 filters values between 70 torr and 80 torr. The highest values above 100 torr were found for spheroids cultured on SFtp0.4. The trend was observed in the oxygen maps as well as the resulting lateral oxygen profiles. Once more, this suggests that it is crucial to take the detailed structure of the membrane into account, rather than solely considering membrane porosity. According to the presented results, subsequent experiments were conducted using the SFtl0.4 filter type.

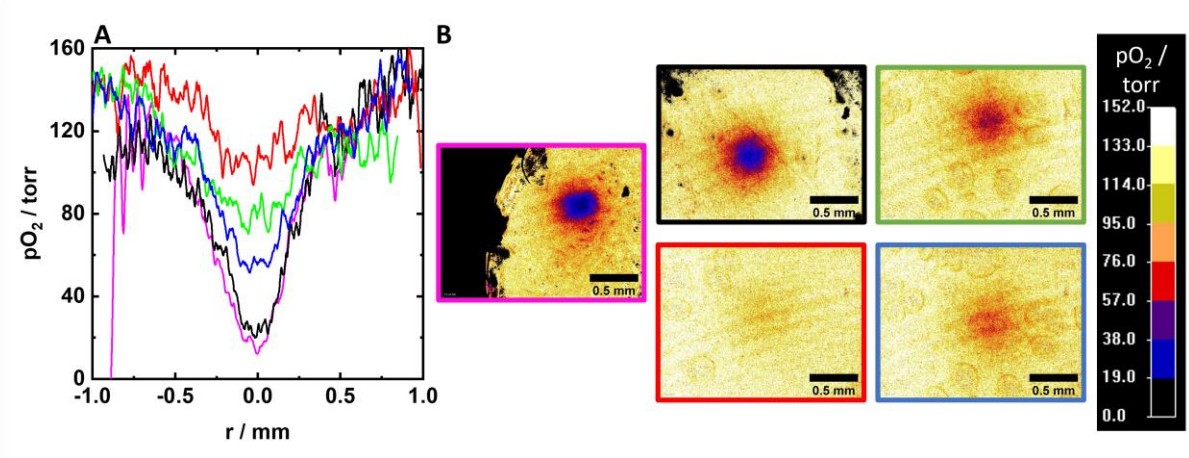

Figure 23: Dependency of lateral oxygen profiles of U373-MG spheroids on porous membrane characteristics. Lateral profiles of partial oxygen pressure (A) and oxygen distribution maps (B) at t = 2 h after measurement start of U373 spheroids. Scalebar: 0.5 mm. U373-MG cells were seeded at an initial cell number of $30 \cdot 10^3$ cells at d = 0 and cultivated for 6 days using the liquid overlay technique. After cultivation spheroids were transferred to filter substrates with different polymer membranes (no filter, SFtl0.4, SFtl1.0, SFtl3.0 and SFtp0.4) in L15 buffer (+ 1 % penicillin/streptomycin). 24 h after transfer, filters were applied directly on the sensor surface and oxygen profiles were measured for several hours using VisiSens TD mic. Experiment was performed in a dry cell culture incubator at 37 °C and 0 % CO_2.

4.2.2 Influence of cell type and spheroid size on oxygen profile

In a next step, the two cell lines, MCF-7 and U373 MG, were monitored at two additional cell numbers, $4 \cdot 10^3$ cells and $6 \cdot 10^3$ cells, respectively. Seeding at different cell numbers resulted in varying spheroid sizes strongly dependent on the cell line. Furthermore, a third cell line, SK-Mel 28, was included to show that the method can be applied to a broad variety of tumor spheroids with different sizes, shapes and tissue origin. MCF-7 spheroids and U373 spheroids strongly differ in growth characteristics. The spheroidal growth of both cells has been described elsewhere before (Frank 2023). MCF-7 cells have a short compacting phase of 1 to 2 days before growing in size, while U373 spheroids are characterized by a continuous compaction of the spheroids. After reaching a certain size, MCF-7 spheroids maintain the same diameter. The growth pattern of MCF-7 cells leads to spheroids with similar sizes after 6 days regardless of the initial seeding density. This spheroid growth pattern was also resolved using VisiSens TD mic (Figure 24 A). The oxygen profiles for MCF-7 spheroids seeded with $4 \cdot 10^3$ cells and $20 \cdot 10^3$ cells were very similar. Only slight variations in oxygen partial pressure in the spheroid center and the width of the profile were observed. Oxygen levels in the center of the spheroids seeded at lower cell numbers were around 30 torr, whereas values for spheroids seeded with $20 \cdot 10^3$ cells were lower around 20 torr. The growth characteristics of U373 cells lead to differences in spheroid size controlled by the seeding density. Seeding with lower density leads to smaller spheroids (Frank 2023). These findings were confirmed using ratiometric optical imaging (Figure 24 B). Lateral oxygen profiles of U373 spheroids seeded with a cell number

of $30 \cdot 10^3$ cells were strongly pronounced reaching oxygen levels in the spheroid center around 30 torr. Oxygen profiles of spheroids seeded with a lower initial cell number of $6 \cdot 10^3$ cells resulted in the formation of the typical oxygen gradient as well. However, the profile was narrower compared to the larger spheroids and the partial oxygen pressure in the center of the spheroids was significantly higher in the smaller spheroids with values around 100 torr. Again, these findings were in line with expected trends found in literature. The larger the spheroid, the bigger the two outer zones containing living cells - proliferative zone and quiescent zone. The more cells reside in these zones, the more cells consume oxygen, resulting in lower partial pressure of oxygen in the center of the aggregate (Mueller-Klieser and Sutherland 1982).

Additionally, the results were compared to lateral oxygen profiles detected for U373 and MCF-7 spheroids cultured directly on the sensor foil surface. The oxygen profiles of spheroids cultured on the filters were again in line with the results obtained by the direct approach. Considering the concurrence of the results, the use of spheroids cultured on permeable substrate for the determination of the oxygen consumption characteristics could be further validated.

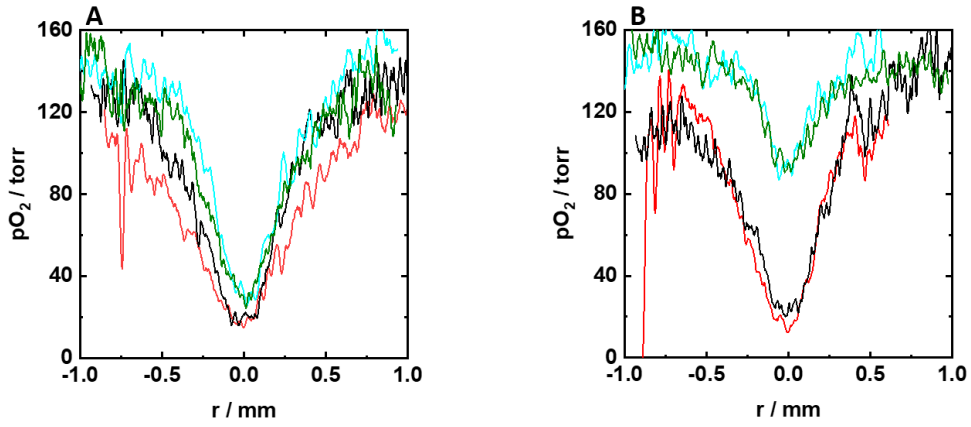

Figure 24: Dependency of lateral oxygen profiles of tumor spheroids on spheroid size and seeding density. Lateral oxygen profiles at t = 2 h of tumor spheroids formed by (A) MCF-7 cells and (B) U373-MG cells. Cells were seeded at two different densities, cultured for 6 days using the liquid overlay technique and finally transferred to the desired filter (SFtl0.4) or sensor substrate. 24 h after transfer, the oxygen profiles were monitored via VisiSens TD mic. MCF-7 spheroids: Filter: **$4 \cdot 10^3$ cells** and **$20 \cdot 10^3$ cells**; direct: **$4 \cdot 10^3$ cells** and **$20 \cdot 10^3$ cells**. U373 spheroids: Filter: **$6 \cdot 10^3$ cells/well** and **$30 \cdot 10^3$ cells**; direct: **$6 \cdot 10^3$ cells** and **$30 \cdot 10^3$ cells**. Experiments were performed in a dry cell culture incubator at 37 °C and 0 % CO_2.

In comparison to the spherical MCF-7 and U373 spheroids, spheroids formed by SK-Mel cells appear in a disklike shape. Lateral oxygen profiles of SK-Mel spheroids obtained via VisiSens TD measurements are presented in Figure 25. SK-Mel spheroids were bigger in size compared to the spheroids before with diameters over 800 µm. Accordingly, lateral oxygen profiles were wider. The partial oxygen pressure in the center was around 20 torr. To demonstrate, that ratiometric imaging of spheroids on filters provides a reproducible method for obtaining oxygen distributions within tumor spheroids, the oxygen profiles of three independently monitored SK-

Mel spheroids are shown Figure 25. A high similarity was found for the oxygen traces of the individual spheroids. The width as well as the oxygen levels in the center were almost identical. Additionally, the experiments shown in chapters 4.2.1 and 4.2.2 have also been reproduced and were depicted in a similar manner in the supplementary information in Figure S 2 to Figure S 5. Regardless of the filter type, cell type or the seeding density, oxygen imaging resulted in reproducible lateral oxygen profiles.

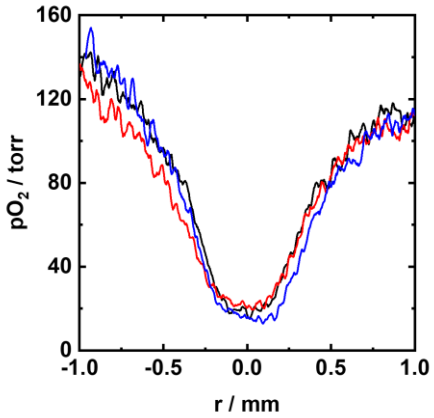

Figure 25: Lateral oxygen profiles of spheroids formed by SK-Mel 28-cells. Cells were seeded at a density of $4 \cdot 10^3$ cells/well, cultured for 6 days using the liquid overlay technique and finally transferred to the filter substrate (SFtl0.4). 24 h after transfer, the oxygen profiles were monitored via VisiSens TD mic. Each color represents the oxygen profile of an individual spheroid at t = 2 h. Experiments were performed in a dry cell culture incubator at 37 °C and 0 % CO_2.

4.2.3 Development of lateral oxygen profiles over time

In a next step, the time resolved development of the lateral oxygen profiles was investigated in more detail. Figure 26 A depicts the lateral oxygen profiles for an MCF-7 spheroid formed from an initial cell number of $20 \cdot 10^3$ cells within the first 90 minutes after the filter was applied to the sensor surface. Oxygen imaging was performed every 10 minutes. Within the first 60 mins, the profile gradually developed until reaching its final and fully developed equilibrium state after approximately 70 mins. Figure 26 B shows the development of lateral oxygen profiles over the course of several hours. A lateral oxygen profile was obtained every hour. Again, the profile was fully developed after approximately one hour. Afterwards, the profile was stable for at least another 4 h. These time-resolved developments are presented from a different perspective in Figure 26 C which shows the development of partial oxygen pressure in the center of the spheroid over time. As expected from the lateral oxygen profiles, partial oxygen pressure decreased linearly within the first hour, before stabilizing at a minimum value of around $pO_2 = 20$ torr. Hence, analysis of lateral oxygen profiles should be conducted 1 - 2 h after application of the filters to the sensor. At t = 2 h the lateral oxygen profiles were fully developed and the experimental observation time may be limited to this initial part of the

experiment. Therefore, lateral oxygen profiles in the following experiments of this thesis were analyzed 2 h after the start of the measurement.

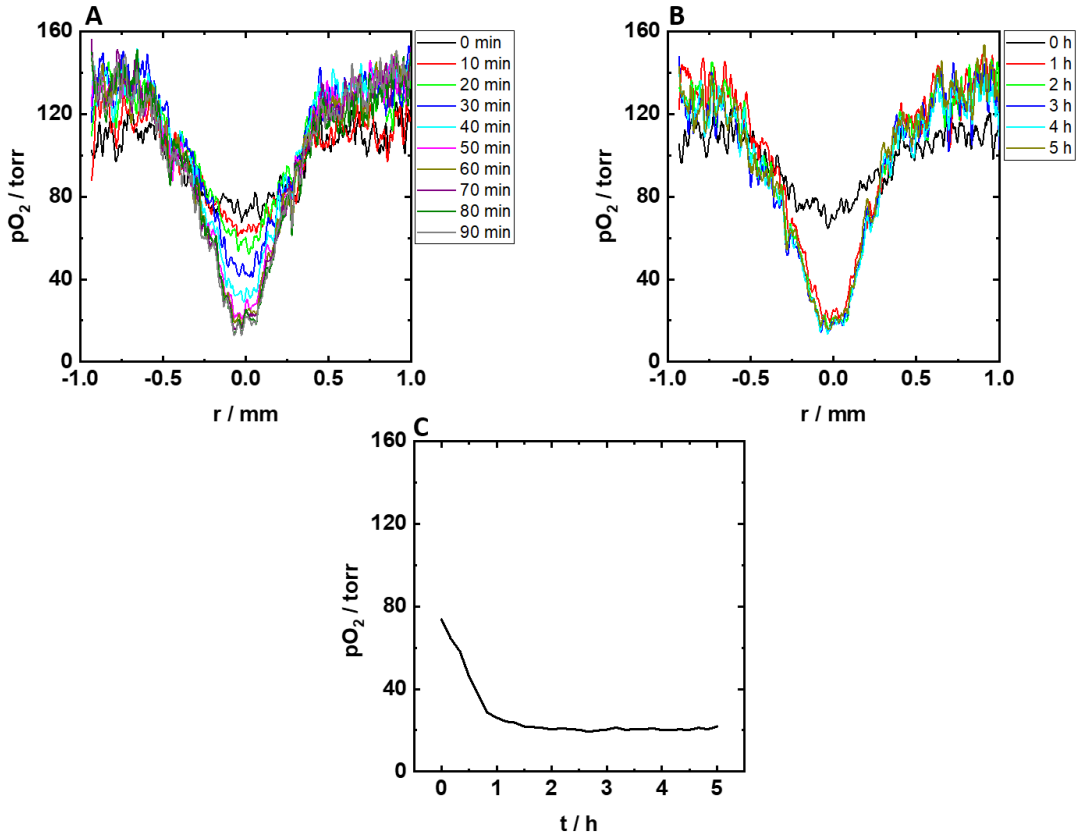

Figure 26: Time resolved development of partial oxygen pressure within a MCF-7 spheroid. (A) Development of lateral oxygen profile within the first 1.5 hours of the measurement. (B) Development of lateral oxygen profile over a period of 5 hours. (C) Time course of partial oxygen pressure in the center region of the spheroid. Cells were seeded at an initial cell number of $20 \cdot 10^3$ cells, cultured for 6 days using the liquid overlay technique and finally transferred to the filter substrate (SFtl0.4). 24 h after transfer, the oxygen profiles were monitored via VisiSens TD mic. Experiment was performed in a dry cell culture incubator at 37 °C and 0 % CO_2.

The detection of the time-resolved development of oxygen profiles offers the possibility to determine oxygen consumption rates for spheroids. The rates found for the different cell lines tested in this work are summarized in Figure 27. *Apparent oxygen consumption rates* in MCF-7 spheroids originally formed from $4 \cdot 10^3$ cells were only slightly lower as AOCR determined for the spheroids formed from initially $20 \cdot 10^3$ cells with values of 2.6 ± 0.2 pmol/s and 3.7 ± 0.2 pmol/s, respectively. In contrast, the difference found for U373 spheroids with different initial cell numbers was strongly pronounced with an AOCR value of 0.31 ± 0.07 pmol/s for the small spheroids ($6 \cdot 10^3$ cells) and 4.0 ± 0.1 pmol/s for the bigger U373 spheroids ($30 \cdot 10^3$ cells). This trend can be attributed to the different growth characteristics described in chapter 4.2.2. Finally, SK-Mel spheroids formed with an initial cell number of $12 \cdot 10^3$ cells were analyzed. Oxygen imaging of these spheroids resulted in the overall highest AOCR with a value of 9 ± 3 pmol/s, which was in line with previous findings,

as SK-Mel cells formed the largest tumor spheroids which subsequently resulted in the strongest oxygen depletion in the center of the spheroids. It is also obvious that the relative errors, calculated from SEM values, found for the consumption rates of SK-Mel cells and the lower initial cell number of U373 cells were significantly higher than the other relative errors. The *apparent oxygen consumption rate* of SK-Mel spheroids had a relative error of 35 % and the relative error found for the small U373 spheroids was around 23 % in comparison to less than 6 % for the other spheroids. In the case of the SK-Mel spheroids, the larger errors can be explained with the extremely fast oxygen consumption. The time resolution, which was set to 10 mins, needs to be adjusted to a shorter measurement interval to obtain more precise data during the linear decrease of time course data crucial for a more precise fitting procedure. The higher errors for U373 spheroids formed from $6 \cdot 10^3$ cells can also be explained using the time-resolved development of the partial oxygen pressure. The consumption of oxygen was very small and very difficult to detect in comparison to the other spheroids, limiting the precision of the linear fit. The lateral oxygen profiles of these small U373 spheroids were hence very close to the limit of detection.

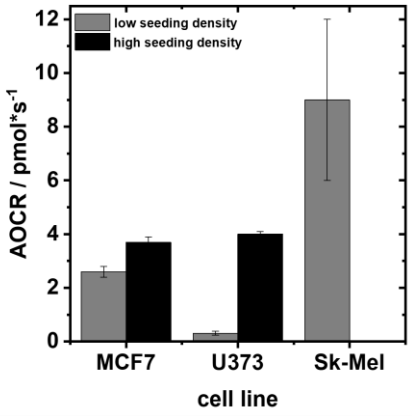

Cell type	Initial cell number/ cells	AOCR / pmol/s
MCF-7	$4 \cdot 10^3$	2.6 ± 0.2
	$20 \cdot 10^3$	3.7 ± 0.1
U373 MG	$6 \cdot 10^3$	0.31 ± 0.07
	$30 \cdot 10^3$	4.0 ± 0.1
SK-Mel 28	$4 \cdot 10^3$	9 ± 3

Figure 27: Apparent oxygen consumption rates found for spheroids of three different cell lines studied with ratiometric oxygen imaging. Cells were seeded at different initial cell numbers and cultured using the liquid overlay technique for 6 d before transfer to the filter substrates (SF0.4tl). After 24 h filters were transferred to the sensor plate. All experiments were performed in a dry cell culture incubator at 37 °C and 0 % CO_2. Data is shown as Mean ± SEM, n = 3.

In the next step, the spatial information and the time-resolved data were combined into an aerobic profile (AEP) of a spheroid. Therefore, the values for the partial oxygen pressure at two distinct values of the lateral oxygen profile were subtracted from the maximum partial oxygen pressure in buffer (149.3 torr). The selected positions were at $r^0 = 0$ mm and $r^+ = 0.1$ mm resulting in $\Delta pO_2(0)$ and $\Delta pO_2(0.1)$, respectively. In addition, the width of the spectrum at a height of $\Delta pO_2(0)/2$ (FWHM) was determined. The temporal information in the aerobic profile is represented by the *apparent oxygen consumption rate* (AOCR). The area within the resulting

spider plot scales with the respiratory activity of the spheroid. The larger the area enclosed by the spider plot; the more oxygen is consumed by the respective spheroid. The areas were normalized to the maximum area of a spider plot enclosed by the outermost line. Figure 28 shows the aerobic profiles found for the spheroids tested in this work. As expected from the data shown individually before, the AEP with the largest area was found for the SK-Mel spheroids (51 %). The AEP of U373 cells was strongly dependent on the initial cell number with an area of 3 % for spheroids seeded with a cell number $6 \cdot 10^3$ cells and an area of 25 % for spheroids formed by an initial cell number of $30 \cdot 10^3$ cells. The AEPs of MCF-7 spheroids with varying initial cell numbers differed only slightly, resulting in areas of 24 % and 31 % for spheroids formed from $4 \cdot 10^3$ cells and $20 \cdot 10^3$ cells, respectively.

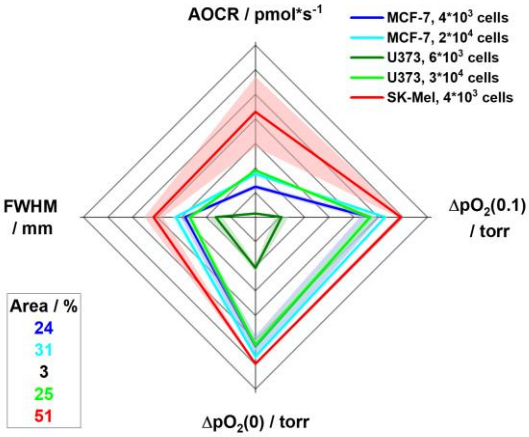

Figure 28: Aerobic profiles of the different spheroids studied in this work. Data are shown as Mean ± SEM (n = 3).

4.2.4 Application of oxidative phosphorylation modulators

To further validate the approach, especially with respect to possible applications in drug development processes, we applied two modulators of the oxidative phosphorylation – antimycin A and malonoben – to the different spheroids. Antimycin A is a blocker of complex III in the electron transport chain. Consequently, cellular respiration is reduced to a minimum or even shut down completely in the presence of antimycin A (Slater 1973). Subsequently, the affected cells induce cell death via an apoptosis-like pathway (Ogita et al. 2009). In contrast, addition of malonoben leads to maximization of cellular oxygen consumption. Malonoben acts as uncoupler of the oxidative phosphorylation. Malonoben is a weak acid and introduces a cycle transporting H^+ ions through the inner mitochondrial membrane (Terada 1975). On the cytoplasmic side of the inner mitochondrial membrane, the anionic form of the uncoupler traps H^+ ions forming its neutral form. The neutral uncoupler can then pass the membrane and release the H^+ ions in the mitochondrial matrix reducing the proton gradient necessary for ATP synthase functionality. The affected organism subsequently reacts by enhanced oxygen consumption

trying to re-establish proton gradients and therefore also ATP synthesis (Terada 1990; Childress et al. 2018). Figure 29 shows the influence of the two modulators on MCF-7 spheroids formed with an initial cell number of $20 \cdot 10^3$ cells. After antimycin A (AntA) addition, the lateral oxygen profile at t = 2 h did not develop anymore. Additionally, oxygen time courses showed that cells within the spheroids stopped consuming oxygen, as the partial oxygen pressure did not decrease but rather increased to values around 140 torr which was close to maximum oxygen concentration in solution at 37 °C (149.3 torr). Furthermore, the results allow for the following conclusions: The decreased oxygen levels in the middle of the spheroids did not result from limited diffusion of oxygen into the center of the spheroid but rather from the consumption of oxygen by the cells in the outer zones. If diffusion of oxygen was a significant factor, the lateral oxygen profiles would still be present after AntA addition. Effects of malonoben were not as significant as the reaction upon antimycin A addition. Nevertheless, malonoben supplementation resulted in the expected formation of a broader lateral oxygen profile as well as a slightly lower minimum of partial oxygen pressures within the MCF-7 spheroids. The spheroid treated with malonoben reached oxygen levels between 5 torr and 10 torr in the center of the spheroid, whereas oxygen levels in spheroids cultured in L15 only decreased to values between 20 torr and 30 torr. The strongest influence by malonoben was observed within the first 30 minutes after treatment. As visible in Figure 29 B, partial oxygen pressures within the spheroid adjusted more rapidly to a stable equilibrium state than spheroids cultured in L15 buffer. However, the equilibrium oxygen levels within the tumor spheroid two hours after treatment started, were only slightly altered by malonoben treatment for MCF-7 spheroids. It is also noticeable, that the oxygen values at the periphery of the spheroids were different. While the values next to spheroids treated with AntA were around 140 torr, the values for spheroids in L15 buffer (around 110 torr) and the values for spheroids treated with malonoben (approx. 100 torr) were significantly lower. There are two possible explanations for this phenomenon: i) The spheroids consumed enough oxygen, that the surrounding medium was also significantly deprived of oxygen or ii) after attachment of the spheroid to the filter substrates, cells proliferated and grew a monolayer surrounding the attached spheroids. Option ii) has been observed before in our lab using CLSM-studies, which showed that MCF-7 spheroids culture directly on the sensor foil surface changed their shape from a sphere to a half sphere like shape and a ring shaped monolayer was formed around the spheroid after attachment (Schmittlein 2018; Pütz 2022). However, we also showed before that this effect is reduced or almost not present when spheroids were cultured on permeable substrates (Frank 2023). Nevertheless, it cannot be fully excluded in this case. It is also possible, that the effect was a combination resulting from both options.

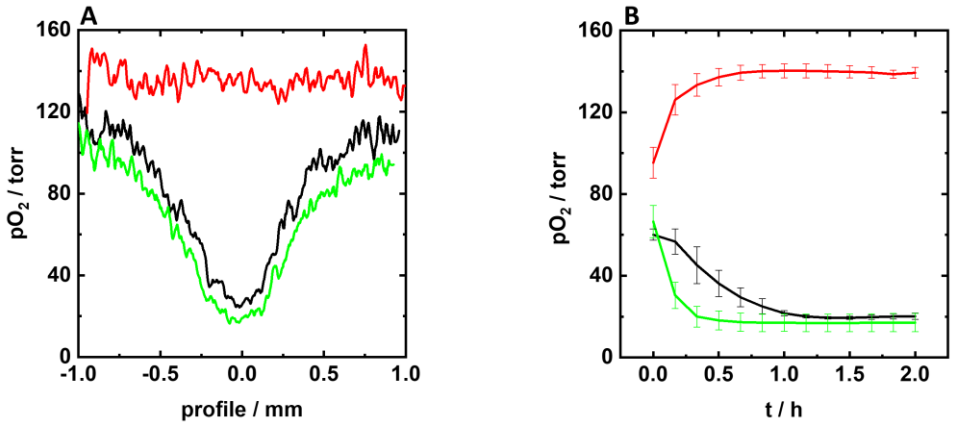

Figure 29: Influence of OxPhos modulators, antimycin A and malonoben, on respiratory activity of spheroids formed by MCF-7 spheroids cultured on permeable substrates (SFtl0.4). (A) Lateral oxygen profiles at t = 2 h and (B) partial oxygen pressure time courses (Mean ± SEM, n = 3) of MCF-7 spheroids treated with **L15 buffer (control)**, **antimycin A (2 µM)** and **malonoben (100 nM)**. Spheroids were formed using the liquid overlay technique for six days with an initial cell number of $20 \cdot 10^3$ cells. Data were recorded using the VisiSens TD mic system in a dry cell culture incubator at 37 °C and 0 % CO_2.

Effects of antimycin A and malonoben on U373 spheroids formed with an initial cell number of $6 \cdot 10^3$ cells were very similar (see Figure 30). Blocking the electron transport chain resulted in an impaired oxygen consumption by the cells within the tumor spheroid. This is expressed in the lateral oxygen profiles as well as the time courses of partial oxygen pressures within the tumor spheroids. The typical u-shaped trajectory of the lateral oxygen profile was not detected. Additionally, the partial oxygen pressure increased again to values around 145 torr across the entire spheroid. Malonoben treatment on the other hand enhanced the oxygen consumption of U373 cells. However, in contrast to the larger MCF-7 spheroids, the effects of malonoben were stronger present in the smaller U373 spheroids. In U373 spheroids, the lateral oxygen profile was broadened by Mal treatment and additionally, the partial oxygen pressure within the tumor spheroid was lower in spheroids treated with malonoben (around 70 torr) compared to control conditions (around 100 torr). The same trend was observed in the time courses of partial oxygen pressure. In addition, the spheroids cultured in buffer containing malonoben decreased continuously until reaching the equilibrium values around 70 torr. Spheroids cultured in pure L15 buffer resulted in a short increase of partial oxygen pressures within the 30 minutes before decreasing again to equilibrium values. The initial increase in partial oxygen pressure observed for spheroids cultured under control conditions and spheroids treated with AntA can be attributed to temperature effects. The fluorescence signal of the sensor foil is altered by small changes in temperature. These effects can be seen for systems without oxygen consumption (AntA or cell-free) or low oxygen consumption. In systems where oxygen is consumed faster, this effect is masked by the fast deprivation of oxygen due to cellular oxygen consumption. Compared to the lateral oxygen profiles above, the difference in partial oxygen pressures in the

spheroid surrounding medium was not present for these U373 spheroids. The spheroids were much smaller and consumed much less oxygen in general, supporting the hypothesis that the changes seen above result from the differences in overall oxygen consumption. However, previous studies also revealed, that U373 spheroids do not form an outgrowing monolayer when cultured on permeable substrates (Frank 2023). Therefore, it is again possible, that the effect seen for MCF-7 spheroids is resulting from outgrowing cells. Overall, both possibilities persist, and none can be fully excluded with the current data.

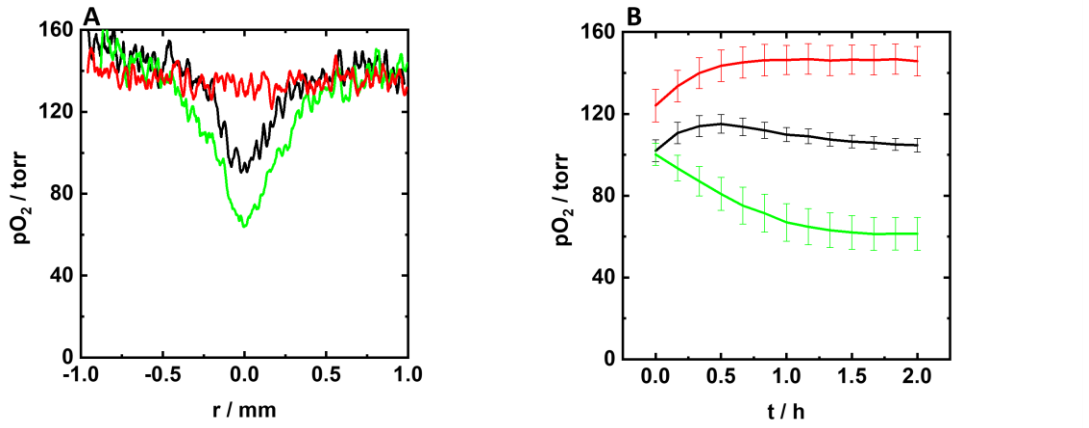

Figure 30: Influence of OxPhos modulators, antimycin A and malonoben, on respiratory activity of spheroids formed by U373 cells cultured on permeable substrates (SFtl0.4). (A) Lateral oxygen profiles at t = 2 h and (B) partial oxygen pressure time courses (Mean ± SEM, n = 3) of U373 spheroids treated with **L15 buffer (control)**, **antimycin A (2 µM)** and **malonoben (100 nM)**. Spheroids were formed using the liquid overlay technique for six days with an initial cell number of $6 \cdot 10^3$ cells. Data were recorded using the VisiSens TD mic system in a dry cell culture incubator at 37 °C and 0 % CO_2.

In addition to the results shown above, the influence of OxPhos modulators on two more initial cell numbers for MCF-7 cells and U373 cells as well as a single initial cell number forming SK-Mel spheroids was studied. The data was used to determine *apparent oxygen consumption rates* and aerobic profiles for the different conditions. The results obtained for the *apparent oxygen consumption rates* and the aerobic profiles for spheroids formed with different cell types and initial cell numbers are summarized in Figure 31. Addition of malonoben, resulted in a more than 2-fold increase in oxygen consumption rates regardless the initial cell number and cell line. Furthermore, the AEP exhibited a larger area for cells treated with malonoben confirming the enhanced oxygen consumption after treatment. In contrast, antimycin A treatment led to a shutdown of oxygen consumption. As the resulting time courses did not result in decreasing pO_2 courses, AOCR values could not be determined and were set to 0 pmol/s. The area enclosed by aerobic profiles for spheroids treated with antimycin A was strongly reduced upon treatment with the electron transport chain blocker. The underlaying time courses and lateral oxygen profiles can be seen above for MCF-7 cells and U373 cells seeded at initial cell

numbers of $20 \cdot 10^3$ cells and $6 \cdot 10^3$ cells, respectively (Figure 29 and Figure 30). The time courses and the lateral oxygen profiles of the other spheroid types are shown in the supplementary information, chapter 11.1, Figure S 6 to Figure S 8.

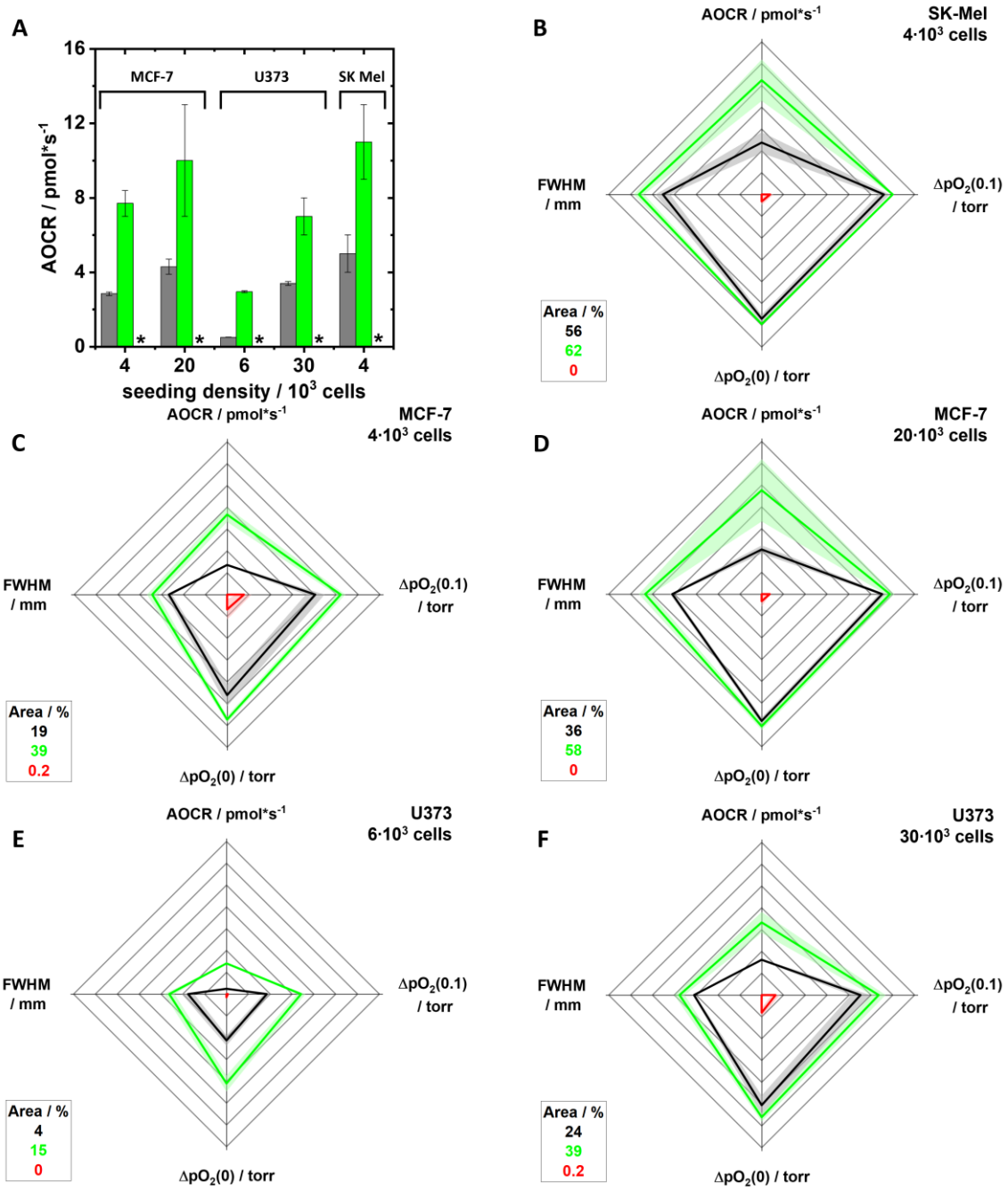

Figure 31: (A) Apparent oxygen consumption rates (AOCR) and (B-F) aerobic profiles of different spheroids treated with OxPhos modulators. Spheroids were seeded at given cell numbers and cultured for 6 d using the liquid overlay technique. After transfer to the filter substrates (SFtl0.4), spheroids were allowed to attach for 24 h on the porous substrates before transfer of the filter to the sensor foil. Spheroids were treated with a **control (L15 buffer)**, **malonoben (100 nM)** and **antimycin A (2 µM**, *). (A) *: As oxygen time courses for spheroids treated with antimycin A did not result in a decreasing pO_2, AOCR could not be determined. Therefore, the values were set to 0 pmol/s. Data were recorded using the VisiSens TD mic system in a dry cell culture incubator at 37 °C and 0 % CO_2 (Mean ± SEM, n = 3).

One might notice that the errors found for the highest two AOCR values were strikingly higher than the others. Relative errors of the AOCR of around 35 % were found for MCF-7 spheroids ($20 \cdot 10^3$ cells/well) and SK-Mel spheroids treated with malonoben. As already described in chapter 4.2.3 this was most likely a result of the fast oxygen consumption within these tumor spheroids. In these cases, oxygen was already depleted to a minimum after 20 mins or even less (Figure S 8), which resulted in difficulties during the fitting procedure. Therefore, it will be necessary to increase temporal resolution of the readout, especially when dealing with highly respirating samples.

4.2.5 Towards a higher throughput

The primary drawback of the method presented above might be the low throughput of the approach, especially when applications in drug testing are envisioned. Each spheroid must be measured in an individual experiment, resulting in time consuming and therefore labor intensive and expensive workflows. In a first attempt, to increase the throughput of the experiment, a new objective was implemented to the system. Instead of the high-magnification objective used before, an objective with less magnification and therefore a larger field of view (see chapter 3.3.2, VisiSens TD area ii) was applied. This allowed for the analysis of several spheroids on a single sensor spot or in a single filter substrate. A proof of principle experiment was performed, in which three SK-Mel spheroids seeded with a cell number of $4 \cdot 10^3$ cells were grown on a single porous substrate and the results measured using the new low-resolution objective were compared to the findings obtained with the high-resolution objective were every spheroid was cultured in a single well. Overall, the results obtained with the two different objectives were similar. The widths and the slope of the lateral and temporal profiles found with the different methods overlapped very well. However, the minimum partial oxygen pressure within the spheroids were slightly higher with values around 30 torr when tested with the new objective than values obtained with the high-resolution lens which decreased to approximately 20 torr. In addition, the time course of partial oxygen pressures within spheroids measured with the new objective was shifted as the partial oxygen pressure showed an initial increase during the first 20 mins of the experiment before decreasing again. However, this might not be resulting from the use of different lens systems but rather from batch differences in the spheroid formation and their areal density. To check on this hypothesis, further experiments with biological replicates must be performed in the future. Additionally, the presence of several spheroids in a single filter support affected oxygen levels throughout the whole filter area. This led to an overall alteration of oxygen levels observed in the oxygen maps (Figure 32 C) which showed reduced pO_2 values also in spheroid-free areas. The same effect was observed in the corresponding lateral oxygen

profiles (Figure 32 A). At the periphery of the tumor spheroid (r = 1 mm) average partial oxygen pressures were found to be 132 ± 4 torr for the spheroids, which were cultured separately from each other when studied with the high-resolution objective. These values were significantly higher than values found for the combination of spheroids, cultured together in a single culture vessel, measured with the new objective, 102 ± 7 torr. In future experiments this problem might be solved by using a filter substrate with a larger porous membrane area and additionally a better distribution of the spheroids across the filter surface. In the experiment shown in Figure 32 the spheroids were positioned close to each other which made rendered recording of independent lateral oxygen profiles more complicated.

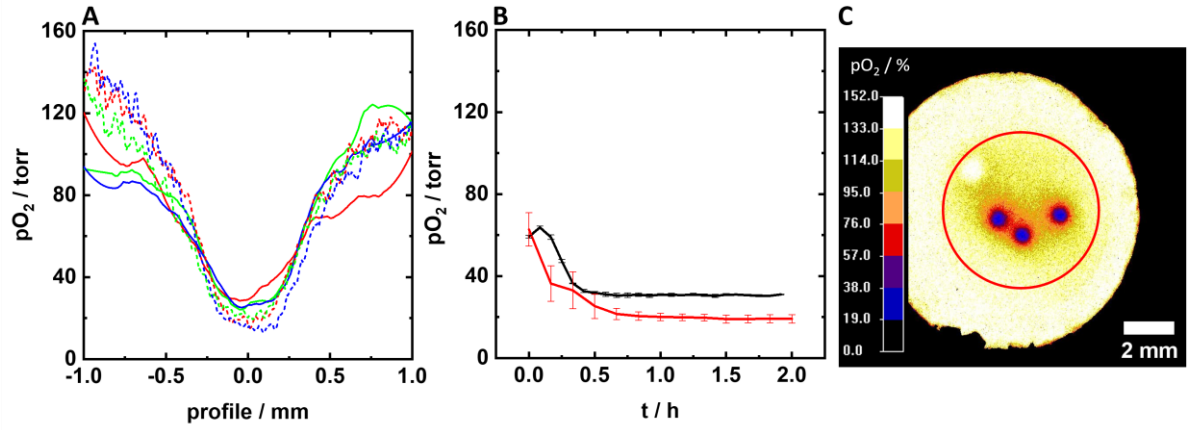

Figure 32: Comparison of ratiometric optical oxygen imaging of SK-Mel 28 spheroids cultured on permeable substrates using different objectives. (A) Lateral oxygen profiles of spheroids measured using high resolution objective **(**dashed lines, single experiments: **red**, **green**, **blue)** and a second objective with lower resolution **(**solid lines, single experiments: **red**, **green**, **blue)** but larger field of view at t = 2 h. Data were of low- and high-resolution objective were obtained from different spheroids. (B) Comparison of time resolved development of partial oxygen pressure within the tumor spheroid. **Black**: VisiSens TD area ii (low resolution); **Red**: VisiSens TD mic (high resolution). (C) Oxygen map of three spheroids monitored with the low-resolution objective. The red circle encloses the area of the porous filter substrate. Scalebar: 2 mm. Data were recorded using the VisiSens TD system in a dry cell culture incubator at 37 °C and 0 % CO_2.

4.2.6 Conclusion and Outlook

The data presented in this work showed, that the VisiSens TD system can be used to determine spatial and temporal development of local partial oxygen pressure across tumor spheroids cultured on permeable substrates. By introducing aerobic profiles, the combination of spatial and time domain data becomes easily interpretable. Oxygen imaging is hereby strongly dependent on the pore density and the overall porosity of the porous substrate. Comparison to spheroids cultured directly on the sensor foil revealed, that especially the pore density seemed to be a crucial factor to obtain results similar to the direct adhesion of spheroids on the sensor surface, which has been validated before as a tool to determine oxygenation across tumor spheroids using *finite element modeling* (Frank 2023). The spatial and the temporal resolution provided by the VisiSens TD setup was utilized to determine drug induced changes by the two

different modulators of oxidative phosphorylation, antimycin A and malonoben. Global *apparent oxygen consumption rates* of the spheroids were determined from time domain data. AOCR values differed depending on cell type, initial cell number and hence spheroid size, as well as the treatment with antimycin A and malonoben. Future experiments might be performed to determine the induced changes in a concentration dependent manner and to expand the approach to different drugs, for instance as used in cancer therapies. In addition, it was observed, that the use of time-resolved data needs further improvement in the future. A better time resolution and a shorter lack time between the application of the filter onto the sensor surface and the starting point of the measurement are inevitable, especially when working with biological systems characterized by high respiratory activity. This has already been adjusted in further experiments shown in this thesis (chapters 4.3, 5.1.3 and 5.2.3). Additionally, the filter-based approach as described here suffers from extremely low throughputs which is limiting in the use for drug development processes but also other applications. Therefore, further improvement of the method aimed for higher throughput by the application of a new objective. The objective was characterized by a lower spatial resolution but a larger field of view enabling the monitoring of several spheroids at the same time. The results proved that the new objective was suitable to obtain similar results as found for using the high-resolution objective. However, further research is needed to address issues such as the equal distribution of the spheroids across the surface of the filter substrates. Better distribution might provide the possibility to determine the lateral oxygen profiles more reliably. Future research might focus on the development of templates positioning the spheroids equally across the filter surface. The application of filter substrates with larger membrane areas might reduce the effect of adjacent spheroids on the overall oxygen levels. Despite these issues, the filter-based approach for monitoring of oxygen consumption of spheroids introduced in the previous chapters could strongly enhance the application of tumor spheroids in research and drug development. The suggested approach enables the possibility to determine several important parameters from the same 3D cell aggregates sequentially (e.g. pH; see chapter 5.2.3) and equally important in a label free and non-invasive manner with temporal resolution. This could strongly enhance the accessible depth of information and further increase knowledge on and the applicability of tumor spheroids in drug development and research.

4.3 Mapping of oxygen profiles underneath complex 3D cell culture models

In addition to the filter approach shown above, the use of VisiSens TD was expanded to monitor more complex cellular models called *organoids* and *precision cut tissue slices*. This work focused on the use of human cortical *organoids* and *precision cut lung slices* due to availability of the biological samples from collaboration partners. In a first step, the tissue models were cultured directly on the sensor foil.

4.3.1 Organoids and Tumoroids

The brain *organoids* and resulting *tumoroids* were prepared by Kim Krieg, Screening Port, Fraunhofer ITMP, Hamburg. The formation was performed using previously described protocols (Paşca et al. 2015; Birey et al. 2017) based on the STEMdiff™ Dorsal Forebrain Organoid Differentiation Kit (STEMCELL Technologies, Vancouver, Canada). *Organoids* were used for oxygen monitoring experiments after a 43-day growth period.

Organoids

In first experiments, brain *organoids* were directly cultured on the oxygen sensor foil glued into a 24 well cell culture plate and the development of the oxygen profile was monitored using VisiSens TD equipped with the area ii kit (low resolution). As *organoids* were between 1 mm and 2 mm in diameter the field of view offered by the VisiSens TD mic setup (high resolution) was two small and the magnification offered by the basal VisiSens TD area i imaging kit was too low. The *organoids* were transferred to the oxygen sensitive foil at day 43 of their growth phase. This time point was selected as the *organoids* are typically used for experiments between day 43 and day 50 of their growth period by our collaboration partners.

A heavily discussed problem in *organoid* research is the proper oxygenation of the inner areas of an *organoid* and the correlated formation of necrotic core zones (LaMontagne et al. 2022; Qian et al. 2019). In large and dense 3D aggregates the availability of oxygen is strongly limited by the oxygen consumption of cells in the outer zones. This might lead to hypoxic oxygen levels in the inner parts of the aggregate. Oxygen values below 10 to 20 torr (Grimes et al. 2014; Lee and Stantz 2016) can strongly promote the formation of necrotic or necrotic like cores. Together with collaboration partners we checked on the oxygen content within the brain *organoids* described above. The resulting profiles were similar to the u-shape described before for tumor spheroids. Oxygen levels in the inside were reduced due to the oxygen consumption of the cells in the outer zones. However, the oxygen pressure in the inner most part of the *organoid* did not fall below 35 torr, which is reported to be in the range of normal global oxygen levels in brain

tissue (Dings et al. 1998; Forcione et al. 2021). The cells in the inner zone of the *organoid* were therefore not exposed to hypoxic oxygen levels indicating the absence of a necrotic core in the organoid center. However, oxygen deprivation is not the only reason for formation of necrotic cores. Accumulation of metabolic waste products such as lactate and less availability of other important nutrients, e.g. glucose, may also induce necrotic core formation (Dirheimer et al. 2022). To fully exclude formation of necrotic zones further experiments would be necessary. Nevertheless, proof of proper oxygenation throughout the *organoid* is an important quality threshold, which was successfully monitored using ratiometric optical imaging.

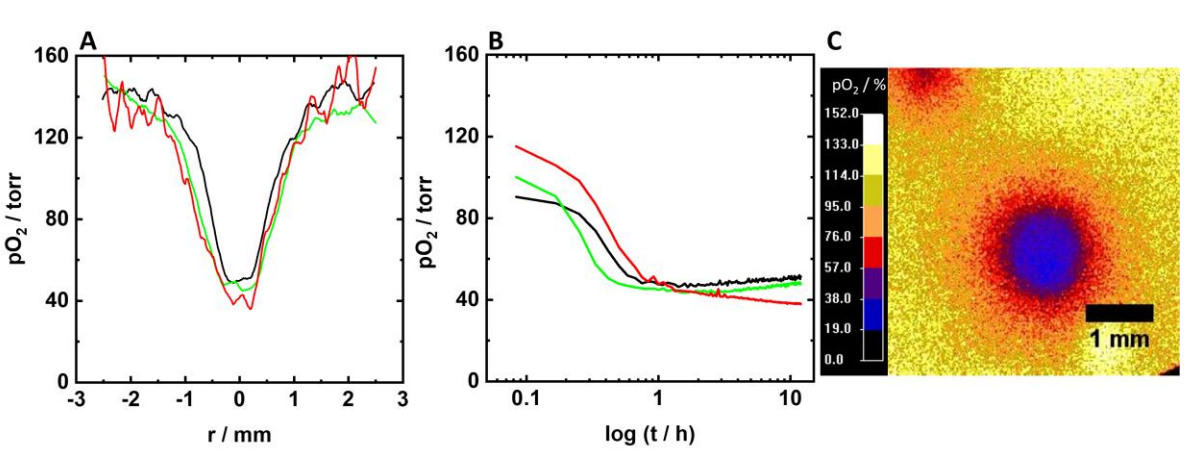

Figure 33: Ratiometric optical imaging of oxygen distribution in brain *organoids*. (A) Lateral profile of partial oxygen pressure through brain *organoids* from three individual differentiation procedures. Each color represents an *organoid* from a different independent differentiation. (B) Time course of partial oxygen pressure during the attachment phase of the *organoid* to the surface of the sensor foil. Each color represents an *organoid* from a different independent differentiation. (C) Oxygen map of a single brain *organoid*. *Organoids* were transferred to the sensor foil glued in a 24-well cell culture plate at day 43 of their growth phase. Data were recorded using VisiSens TD equipped with the area ii imaging kit in a dry cell culture incubator at 37 °C and 5 % CO_2.

As already shown for spheroids, it was possible to develop aerobic profiles for the studied *organoids* (Figure 34). The AEPs revealed, that the *organoids* were slightly different in size which resulted in different FWHM. Additionally, the AOCR values were different. As the *organoids* were cultured directly on the sensor foil and the measurement was started immediately after the *organoids* were placed in the wells, it is possible that the *organoids* attached to the substrate at different speeds. This might influence the development of partial oxygen pressures over time and the values found for the AOCR. The differences in the AOCR and the FWHM led to varying relative areas found for the three organoids, ranging from 34 % to 49 %. The AEPs of the cortical *organoids* were compared to an AEP obtained for a U373 spheroid formed by an initial cell number of $30 \cdot 10^3$ cells. U373 cells are cells originating from a glioblastoma. The AEP of U373 spheroids was overall much smaller (18 %) than the aerobic profiles found for the *organoids*. The oxygen values within the tumor spheroids indicated by $\Delta pO_2(0)$ and $\Delta pO_2(0)$ were similar to the values found for *organoids*. However, the spheroids

were much smaller in size (FWHM) and oxygen was consumed slower (AOCR). It is possible, that tumor spheroids form a denser aggregate than the studied cortical *organoids*, which could lead to the similar oxygen values within the center even though the overall size differs strongly.

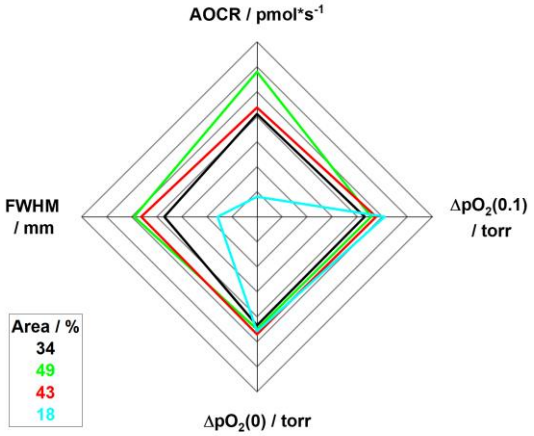

Figure 34: Aerobic profiles of cortical *organoids* of three different differentiations (black, green, red) compared to an AEP of a U373 spheroid formed from $30 \cdot 10^3$ cells using the liquid overlay technique. Data were recorded in a dry cell culture incubator at 37 °C and 5 % CO_2 using the VisiSens TD area ii setup.

After showing oxygenation of *organoids* was accessible using VisiSens TD, *organoids* were treated with antimycin A (2 µM) to further validate the approach. Therefore, two *organoids* at day 43 were cultured on the oxygen sensor foil. After measuring the basal oxygen consumption in medium for 6 h, antimycin A (2 µM) was added and the *organoids* were monitored for an additional 6 h. The AEPs of both *organoids* prior to antimycin A addition and 2 h after AntA treatment can be seen in Figure 35. In both cases the areas of the aerobic profiles diminished after addition of AntA from 26 % to 0 % for the first organoid and from 42 % to 0 % in the second case. Therefore, blocking of the electron transport chain resulted in the expected shut down in oxygen consumption and the following increase in partial oxygen pressure (Slater 1973). The full reoxygenation of the tissue model showed that oxygen was able to diffuse into the center of the organoid – a factor ensuring the sufficient oxygenation of the cells throughout the *organoid*.

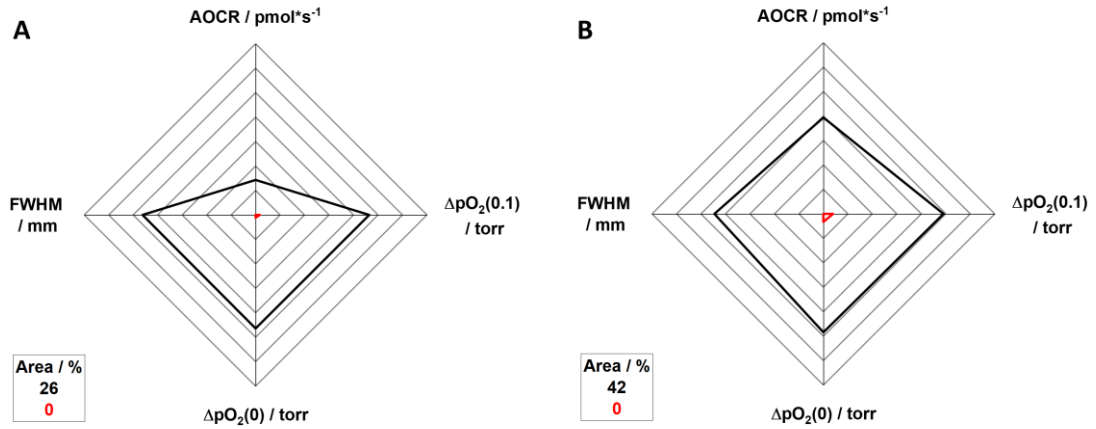

Figure 35: Aerobic profiles of individual *organoids* treated with electron transport chain blocker antimycin A. *Organoids* were measured in **medium** (**black**) and in **antimycin A (2 µM, red)**. (A) Organoid 1. (B) Organoid 2. *Organoids* were transferred to the sensor foil glued in a 24-well cell culture plate at day 43 of their growth phase. Data were recorded using VisiSens TD equipped with the area ii imaging kit in a dry cell culture incubator at 37 °C and 5 % CO_2.

Tumoroids

In a further series of experiments, brain *organoids* were used as niche model for A375 cancer cells, a malignant melanoma cell line derived from a 54 year old female (Giard et al. 1973). The resulting co-culture is considered as a model for cancer metastasis into the brain. The co-culture was obtained by inoculating suspended A375 cells to the *organoids* at day 43, resulting in so called *tumoroids*. The *tumoroid* was then cultured on non-adhesive substrates for 5 more days before oxygen imaging was performed. To show that the *tumoroids* result in different oxygen footprints than *organoids*, we applied an *organoid* at day 48 and a *tumoroid* at day 43 + 5 on the same sensor surface and measured them simultaneously. The comparison of the results can be seen in Figure 36. Oxygen partial pressures within *organoids* were stable after full formation. This was observed for lateral oxygen profiles, time courses of partial oxygen pressure, as well as the original oxygen distribution maps. The oxygen maps showed that there were clear differences in the oxygen distribution across the *tumoroid* at t = 6 h and the oxygen map for the *tumoroid* after 30 hours. We observed that the oxygen deprived area grew in case of the co-culture model whereas it stayed stable in case of the pristine *organoid*. In addition, the co-culture model seemed to change from a circular shape to a more irregular shape with areas of outgrowth. Similar observations were made when looking at the corresponding lateral oxygen profiles. While the lateral profile of the *organoid* did not change significantly between 6 h and 30 h, the lateral profile of the *tumoroid* under study broadened over time. Additionally, to the enlargement a second minimum at approximately r = 1 mm from the center of the *tumoroid* formed. Most importantly, however, the partial oxygen pressures in the center of the *tumoroid* did not significantly decrease due to the application of the cancer cells. In other words, the

quality criterium of proper oxygenation was still given after co-culture with cancer cells. Closer analysis of the time-resolved data revealed similar trends. Partial oxygen pressures within the pristine *organoid* and the *tumoroid* reached stable values around six hours after application to the sensor foil surface. However, oxygen levels in the rim areas of both models behaved differently. The partial oxygen pressure at the edge of the *organoid* reached stable values after six hours, whereas oxygen levels in the rim area of the *tumoroid* decreased continuously until the end of the measurement, indicating that the *tumoroid* was gaining size over the course of the measurement. Partial oxygen pressure in the area of the outgrowth behaved similar to the oxygen levels in the rim area. We could therefore distinguish between the *organoid* and the *tumoroid* using ratiometric optical imaging through analyzing the lateral oxygen profiles as well as the temporal development of oxygen in different zones of the models. We believe that the areas of outgrowth and the enlargement of the oxygen profile was caused by cancer cells infiltrating the periphery of the niche forming new cancer cell aggregates. However, final prove for this theory is ongoing research.

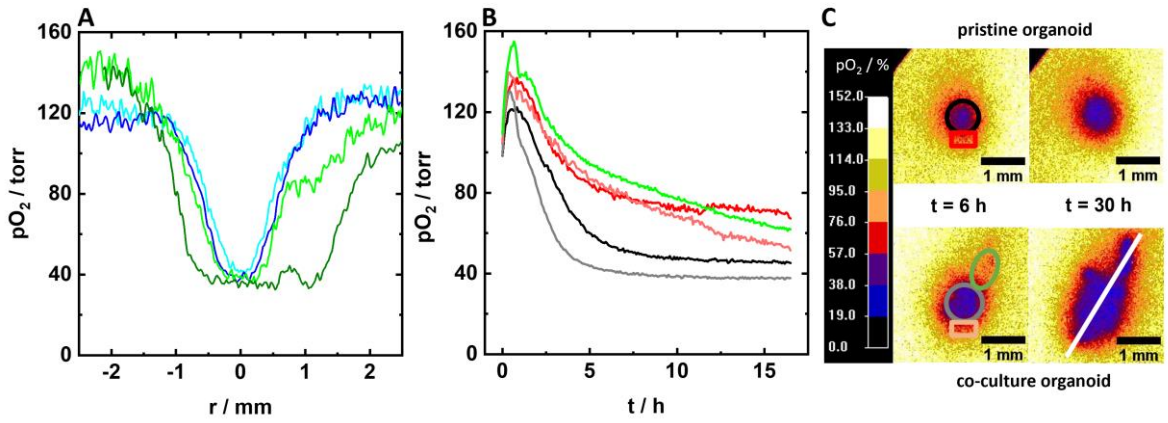

Figure 36: Ratiometric optical imaging of oxygen distribution in a brain *organoid* co-cultured with A375 cancer cells and a pristine brain *organoid*. (A) Comparison of lateral oxygen profile of **plane organoid at t = 6 h**, **a plane organoid at t = 30 h**, **a tumoroid at t = 6 h** and a **tumoroid at t = 30 h**. (B) Time courses of partial oxygen pressure within different regions of the *organoid* and the co-culture model after addition to the sensor foil. The results were obtained by a z-stack analysis of the regions of interest depicted in (C): **center organoid**, **rim organoid**, **center co-culture**, **rim-co-culture**, **outgrowth co-culture**. (C) Oxygen maps derived from an *organoid* and a *tumoroid* at t = 6 h and t = 30 h after application to the sensor foil surface. The white line indicates the direction in which the lateral oxygen profiles for (A) were determined. Scalebar: 1 mm. The *organoids* were transferred to the sensor foil glued in a 24-well cell culture plate at day 48 of their growth phase. A375 cells were supplemented to *organoids* at day 43 of the organoid growth phase. Cancer cells and *organoids* were co-cultured for 5 days in respective growth plates before transfer to the sensor foil at day 43 + 5. Experiment was performed in a dry cell-culture incubator at 37 °C and 5 % CO_2.

The time resolved development of partial oxygen pressure shown in Figure 36 B can be used to determine *apparent oxygen consumption rates* for the different regions of the pristine *organoid* and the co-culture model, the *tumoroid*. However, there were two different phases in the time domain data. Therefore, two AOCR values were determined for each region in Table

6. During the first six hours, partial oxygen pressure decreased linearly regardless the model. The consumption rate of the center region of the *tumoroid* was faster (9.85 pmol · s^{-1}) than the rate found for the organoid (6.67 pmol · s^{-1}). This could result from the combination of cancer cells and the original *organoid* material in the co-culture which in addition consumed oxygen faster than the cells in the pristine *organoid*. The AOCR values in the rim of the *organoid* and the rim and outgrowth area of the *tumoroid* did not differ strongly during the first six hours. However, in the time frame between 6 h and 16 h, partial oxygen pressure in these zones of the *organoid* reached an equilibrium status, while the values decreased further in the *tumoroid*. AOCR values in the rim and the outgrowth area of the *tumoroid* were 4-fold higher for *tumoroids* than the AOCR value found for the rim region of the *organoid* (Table 6). This supports the hypothesis stated above, that the rim area of the *tumoroid* is colonized by the A375 cells, which resulted in further decrease of partial oxygen pressure. The AOCR values found for the center region of *organoids* and *tumoroid* in the time frame between 6 h and 16 h was equally low, as partial oxygen pressures stayed stable in both cases.

Table 6: Apparent oxygen consumption rates of the different zones established during oxygen monitoring of organoids and tumoroids. Data were recorded using the VisiSens TD area i setup. In case of the organoid, no outgrowth was detected, therefore no AOCR was determined in this case.

	$AOCR_{0\text{-}6\ h}$ / pmol · s^{-1}		**$AOCR_{6\text{-}16\ h}$ / pmol · s^{-1}**	
model	**organoid**	**tumoroid**	**organoid**	**tumoroid**
center	6.67	9.85	0.21	0.11
rim	5.44	4.44	0.26	1.08
outgrowth	-	5.17	-	1.06

4.3.2 Precision-cut tissue slices

Along with monitoring of organoids we developed a process to characterize *precision cut tissue slices* with regard to their oxygenation using VisiSens TD area ii setup in a label-free and non-invasive manner. Therefore, *precision cut lung slices* (PCLS) where directly applied onto the surface of the oxygen sensor foil that had been glued into a 12-well cell-culture plate before.

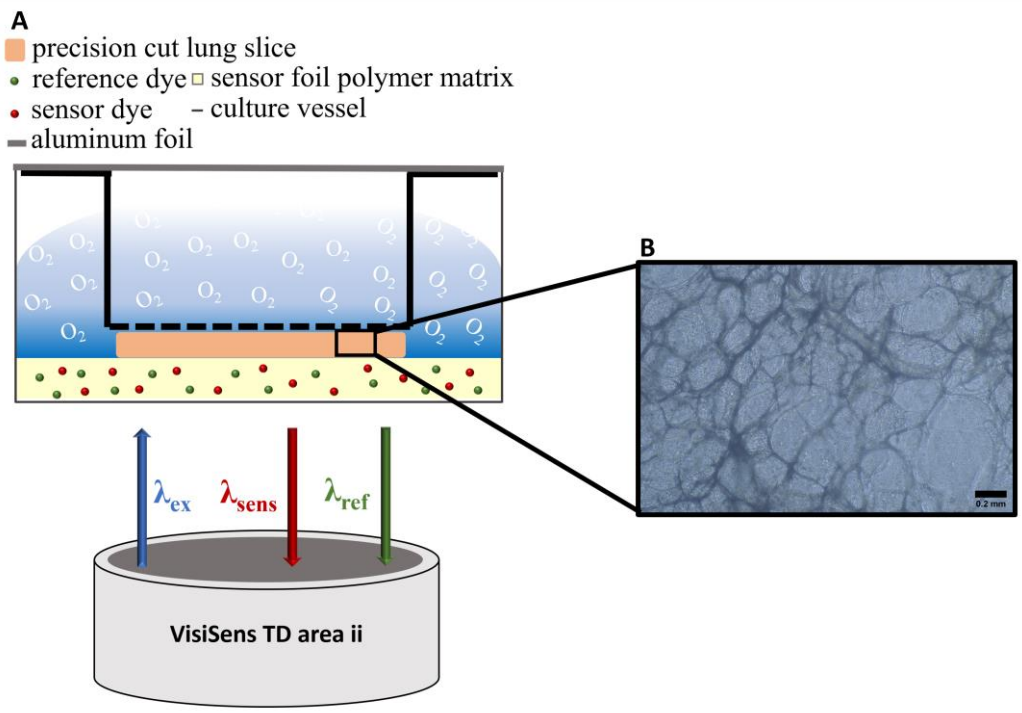

Figure 37: Monitoring of the oxygen profile underneath a *precision cut lung slice*. (A) Schematic setup used to monitor the oxygen content underneath a *precision cut lung slice*. Slices were directly applied on the surface of the sensor foil and were pinned down using a 24-well cell culture insert with a permeable membrane. (B) Picture of a *precision cut lung slice* taken via phase contrast microscopy. Scalebar: 0.2 mm.

Precision cut lung slices were obtained from the group of Armin Braun, Fraunhofer ITEM Hannover. The tissue slices were transported at 4 °C from Hannover to Regensburg. Upon arrival, the tissue slices were transferred to a 24-well cell culture plate filled with 500 µL of fresh culture medium. Each well held two tissue slices. Afterwards, the plate was incubated in a standard cell culture incubator (37 °C, 5 % CO_2. 95 % relative humidity) for at least 3 h before use. After a maximum of six days, the remaining slices were autoclaved and disposed of. For the measurements, a circular piece of oxygen was glued to the bottom of a 12-well cell culture plate. The well was filled with 1 mL of the culture medium before one lung slice was transferred onto the sensor foil. To ensure that the lung slice did not lift off the sensor foil, a 24-well filter substrate was pushed downwards to hold the lung slice in place. The apical compartment of the filter substrate was filled with 500 µL of cell culture medium (Figure 37 A). Finally, the well was sealed with a self-adhesive aluminum foil (Greiner Bio-One GmbH, Kremsmünster,

Austria), preventing further oxygen input from the surrounding atmosphere. The system was labeled as semi-closed, as there was still a certain volume of air above the cell culture medium. This step was necessary, as it was not possible to measure any oxygen signature in an open setting (Supplementary information, chapter 11.1, Figure S 9). Time resolved oxygen distribution maps of a *precision cut lung slice* cultured in the semi-closed system are depicted in Figure 38. Oxygen imaging revealed local differences of oxygen levels within the tissue slice. The different oxygen levels at different positions could result from i) varying cell densities within the tissue slice or ii) differences in oxygen consumption characteristics of the various cell types present in the ex-vivo tissue model. Looking at a phase contrast picture of a precision cut tissue slice it is clear, that the cellular distribution in the lung slices was extremely heterogenous (Figure 37 B), supporting the theory that the heterogeneity in the oxygen maps was caused by the same heterogeneity in the distribution of the cells. The higher the cellular density at a certain spot within the tissue slice, the higher is presumably the oxygen consumption resulting in lower oxygen levels.

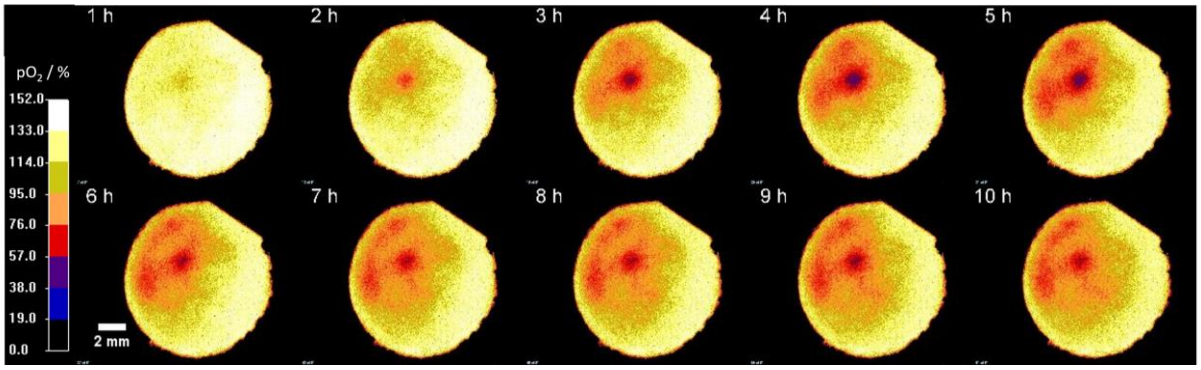

Figure 38: Oxygen distribution maps of an individual *precision cut lung slice* in L15 buffer over the course of 10 h. The PCLS was applied directly on the sensor foil surface and fixed using a 12-well filter insert (d_{pore} = 0.4 µm, $\delta_{pore} = 100 \cdot 10^6$ pores/well) in a semi-closed system. Scalebar: 2 mm (valid in every picture). Experiment was performed in a dry standard cell culture incubator at 37 °C and 0 % CO_2.

After measuring the basal respiratory activity of the tissue slice in L15, the tissue slice was treated with malonoben (100 nM). As expected, the oxygen levels strongly decreased due to the enhanced respiratory activity of the cells within the *precision cut lung slice* (see Figure 39). The respiratory activity was increased following the uncoupling of the electron transport chain by malonoben (Terada 1990). Despite the overall enhanced oxygen consumption, the heterogeneity in the spatial distribution of oxygen underneath the tissue slice remained similar to the distribution measured in L15 buffer (compare Figure 38). Areas with higher oxygen consumption under control conditions resulted in lower oxygen values even after malonoben addition.

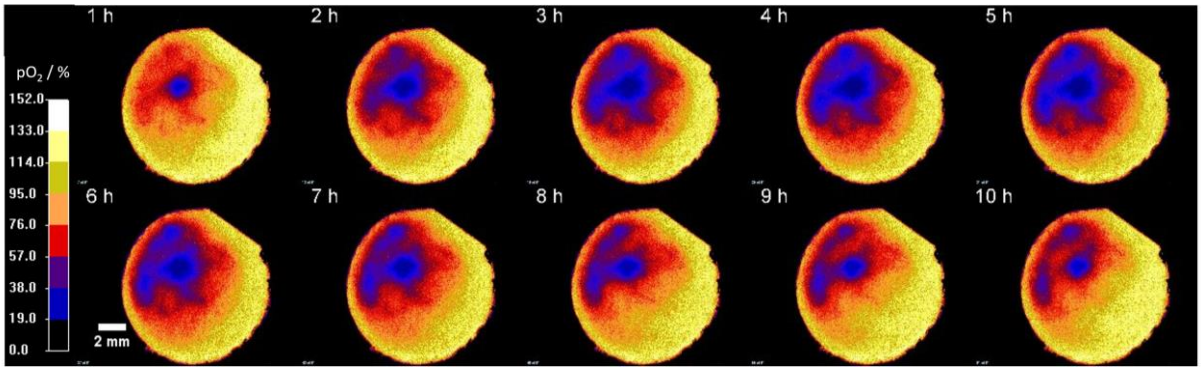

Figure 39: Oxygen distribution maps of an individual *precision cut lung slice* in L15 buffer supplemented with malonoben (100 nM) over the course of 10 h. The PCLS was applied directly on the sensor foil surface and fixed using a 12-well filter insert (d_{pore} = 0.4 µm, δ_{pore} = 100 · 10^6 pores/well) in a semi-closed system. Scalebar: 2 mm (valid in every picture). Experiment was performed in a dry standard cell culture incubator at 37 °C and 0 % CO_2.

In a last experiment, we supplemented the same tissue slice with antimycin A (2 µM) after malonoben treatment. As described in previous chapters, the electron transport chain blocker inhibited oxygen uptake by the cells (Slater 1973). Consequently, the areas which revealed oxygen depletion before were reoxygenated almost immediately (also see Figure 41 B) and there was no further oxygen uptake recognizable. Oxygen levels increased to approximately 149 torr within the first 2 h and stayed stable for at least 10 h.

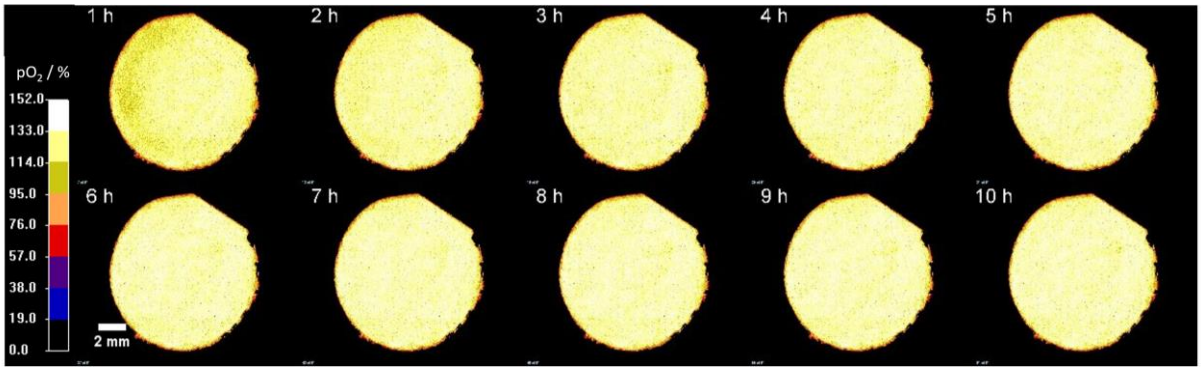

Figure 40: Oxygen distribution maps of an individual precision cut lung slice in L15 buffer supplemented with antimycin A (2 µM) over a time-course of 10 h. The PCLS was applied directly on the sensor foil surface and fixed using a 12-well filter insert (d_{pore} = 0.4 µm, δ_{pore} = 100 · 10^6 pores/well) in a semi-closed system. Scalebar: 2 mm (valid in every picture). Experiment was performed in a dry standard cell culture incubator at 37 °C and 0 % CO_2.

To further quantify the changes of partial oxygen pressure within the tissue slice described above, the partial oxygen pressure time courses of two regions of interest were determined (Figure 41 B). As regions of interest, a region with presumably high cellular density and a region with presumably low cell density were chosen. In addition, the time courses were used to calculate *apparent oxygen consumption rates* for the tissue slice. The results confirm the findings described above. The heterogeneity of cell density within the lung slice resulted in regions with overall different *apparent oxygen consumption rates*. Treatment with malonoben enhanced oxygen consumption of the cells, leading to a decrease in overall oxygen levels and

increased *apparent oxygen consumption rates* regardless the cell density. Application of antimycin A (2 µM) shut down cellular oxygen consumption and partial oxygen pressures increased to around 140 torr, which is close to the maximum of 149.3 torr. The AOCR for the AntA treatment was not calculated, as the partial oxygen pressure time courses did not result in decreasing oxygen levels needed for the calculation. As before, the values were set to 0 pmol · s^{-1}.

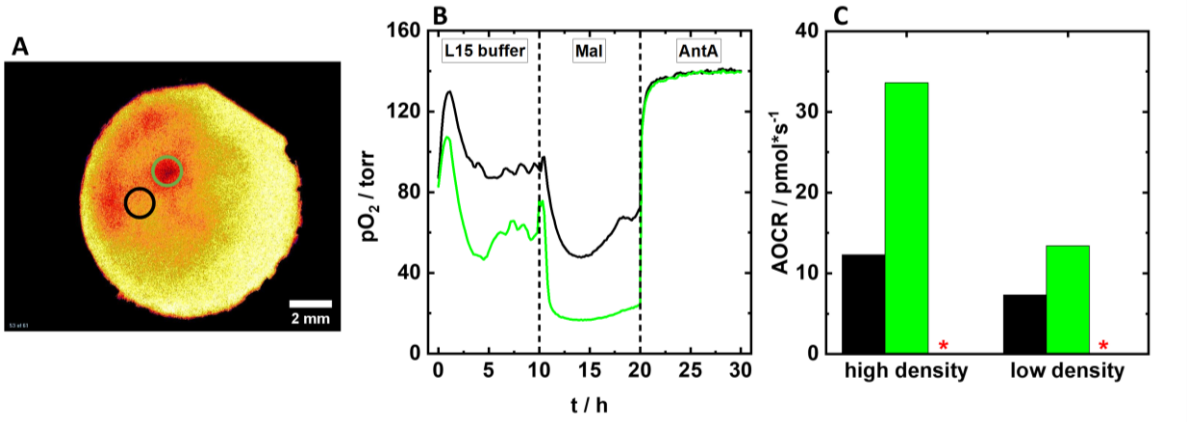

Figure 41: Time resolved analysis of partial oxygen pressure of PCLS at two different regions of interest. (A) Regions of interest chosen for time resolved analysis of PCLS. **Green: High density of cells**, **Black: Low density of cells**. (B) Partial oxygen pressure time courses of the two ROIs shown in (A). Before first dashed line: PCLS in L15 buffer. After first dashed line: PCLS in malonoben (100 nM). After second dashed line: PCLS in antimycin A (2 µM). (C) Apparent oxygen consumption rates of the cells in the different ROIs of the PCLS cultured in **L15 buffer**, **malonoben (100 nM)** or **antimycin A (2 µM)**. *: As oxygen time courses for spheroids treated with antimycin A did not result in a decreasing pO_2, AOCR could not be determined and was set to 0 pmol · s^{-1}. Experiment was performed in a dry standard cell culture incubator at 37 °C and 0 % CO_2.

4.3.3 Conclusion and Outlook

The previous chapters successfully demonstrated that monitoring of *organoids* and *precision cut tissue slices* is possible with ratiometric optical imaging of oxygen. The VisiSens TD area ii setup was used to perform quality control experiments of brain *organoids* derived from human induced pluripotent stem cells. Thereby the experiments provided proof that no hypoxic cores have formed during the culture phase of the *organoid*. Furthermore, antimycin A addition revealed that the oxygen deprivation in the center of these 3D aggregates originates from the oxygen consumption of the outer cell layers rather than diffusion limitation – similar to what has already been observed for tumor spheroids. Additionally, we were able to distinguish oxygen consumption signatures from *organoids* and *organoids* co-cultured with A375 cancer cells (*tumoroids*). Future research might focus on the treatment of *tumoroids* with chemotherapeutics. This could pave the way to use VisiSens TD as a label-free platform for hit validation of anti-cancer or anti metastasis drugs together with the presented metastasis model. Further, *organoid* models might also be investigated while cultured on permeable filter

substrates offering the possibility to monitor several parameters within the same 3D aggregates. In addition, it will be important to prove, that the areas of outgrowth observed in the oxygen maps of the *tumoroids* are formed by the supplemented cancer cells. This might be achieved by fixing measured 3D aggregates on the sensor foil, followed by an antibody staining towards a tumor-specific marker and further analysis by fluorescence microscopy. A spatial correlation between fluorescent microscopy and ratiometric optical imaging by VisiSens TD would prove the hypothesis given in chapter 4.3.1.

In addition to the determination of oxygenation within brain *organoids*, an assay procedure enabling the label-free and non-invasive monitoring of *precision cut lung slices* was established. As already discussed for the co-culture models above it will be crucial to validate cell containing areas determined by oxygen maps with the use of a second approach such as fluorescent microscopy after cell staining. We successfully showed that the setup might be used to reveal drug induced changes of the oxygen distribution within the tissue slice. Application of antimycin A and malonoben resulted in the expected changes in oxygen levels. Going ahead, the setup could be used during cultivation of the tissue slices closely monitoring the oxygenation of the slices. Currently, *precision cut tissue slices* can only be used for a limited amount of time, due to instability of certain cell types within the slices. Improved cultivation protocols such as microfluidic approaches coupled with close monitoring of nutrient and oxygen supply is being pursued as a solution to better long-term stability (Garcia-Garcia et al. 2022). A possibility might also be to co-culture tissue slices with cancer cells, giving rise to a second metastasis model monitored by ratiometric optical imaging. In addition, monitoring of tissue slices obtained from lung tissue with metastatic intrusions could be of interest.

5 Ratiometric Optical pH Imaging of 2D and 3D cell culture models

One of the overall goals of this work was the development of an assay concept to determine oxygenation and extracellular acidification of the same cellular model. The next step was to develop a protocol for the determination of extracellular pH of 2D cell layers as well as spheroids cultured on permeable substrates. The following chapters will focus on different aspects important during the monitoring of extracellular acidification.

5.1 pH monitoring of 2D cell layers cultured on permeable substrates

5.1.1 Influence of cell-to-sensor distance

In a first step the determination of the extracellular acidification using VisiSens TD for simple 2D cell layers cultured on permeable substrates was developed. During routine culture, the filter substrates are hanging in cell culture plates enabling nutrient supply from both sides of the cell layer. The volume of the medium created between the cell layer and in this case the surface of the sensor foil will likely influence the correct determination of the extracellular acidification. To determine the influence of the cell-to-sensor distance and the resulting gap volume, we compared the results found for three different distances to direct placement of the filter onto the sensor surface. Distances were adjusted with the help of polydimethylsiloxane (PDMS) spacers with defined thicknesses. Setups with different gap volumes were tested using two different cell lines, MCF-7 cells and SK-Mel cells. The results can be seen in Figure 42. Both, the time courses and the *extracellular acidification rates* (EAR) of MCF-7 cells and SK-Mel cells revealed a dependency of the measurement on the distance between sensor surface and cell layer. The maximum of acidification was measured for the direct placement of the filter onto the sensor surface. Additionally, the time courses showed that the pH at the beginning of the experiment was already lower for the direct placement than for the filters hanging in distance to the sensor surface. With increasing gap distance, the overall acidification of the medium surrounding the sensor foil decreased. The *extracellular acidification rate* of SK-Mel cells was only slightly altered by hanging the filter above the sensor foil in a standard 24-well cell culture plate (300 µm) compared to the direct placement. The values very similar in both cases with EAR = 24.7 ± 0.8 mpH·min^{-1} for the direct approach and EAR = 22.3 ± 0.4 mpH·min^{-1} for the hanging filter. However, increasing the gap distance further, resulted in hardly measurable changes in pH. This led to a strong decrease of the EAR to values of EAR = 7 ± 0.2 mpH·min^{-1} and EAR = 2.45 ± 0.07 mpH·min^{-1} for distances of 500 µm and 1500 µm, respectively. In case of the MCF-7 cells, the normal distance between a hanging filter

to the surface of the sensor (300 µm) significantly altered the time courses and the resulting *extracellular acidification rates*. Acidification rates found for MCF-7 cells decreased from values of EAR = 37 ± 1 mpH·min^{-1} for the direct placement of the filters to values of EAR = 9.9 ± 0.1 mpH·min^{-1} for a gap distance of 300 µm. Bigger gap distances resulted in even lower acidification rates with values of EAR = 3.7 ± 0.4 mpH·min^{-1} and EAR = 2.9 ± 0.1 mpH·min^{-1} for the gap distances of 500 µm and 1500 µm, respectively. While this development would be favorable in routine culture (better medium supply), the trend leads to the necessity of a direct placement of the filter substrate onto the sensor surface for reliable determination of the extracellular acidification.

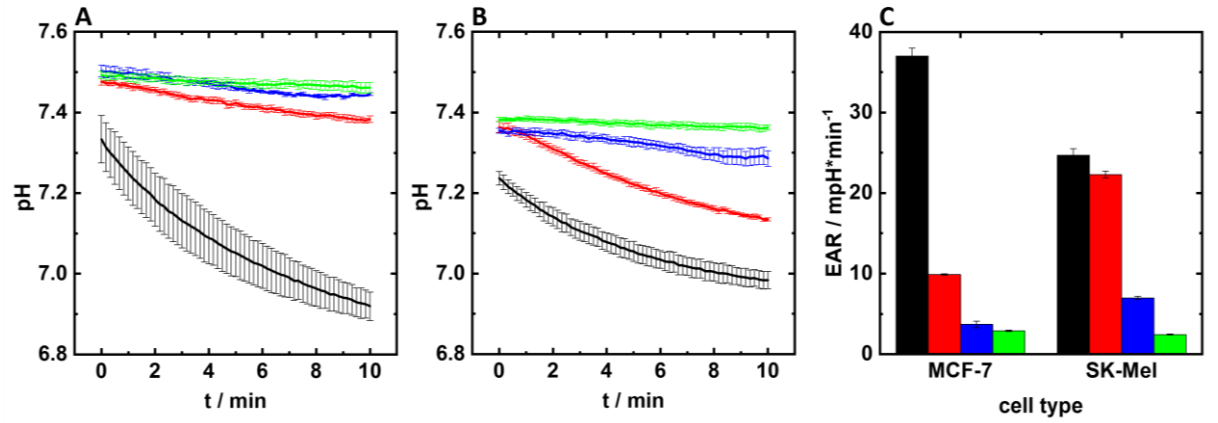

Figure 42: Influence of gap distance on monitoring of extracellular acidification of cells cultured on permeable substrates using VisiSens TD. Extracellular pH of MCF-7 cells (A) and SK-Mel cells (B) cultured on permeable substrates (SFtl0.4) as function of time. Cells were inoculated 48 hours prior to the experiment. Filter substrates were placed with different distances between sensor and cell layer using PDMS spacers: **black: no gap**, **red: 300 µm**, **blue: 500 µm**, **green: 1500 µm**. *Extracellular acidification rates* (C) determined from time courses shown in (A) and (B). Data were obtained using the VisiSens TD area i imaging kit. All experiments were performed in L15 supplemented with glucose (4.5 g/L) in a dry standard cell culture incubator at 37 °C and 0 % CO_2 (Mean ± SEM, n = 3).

5.1.2 Impact of glucose deprivation and oxidative phosphorylation modulators on EAR

In a second set of experiments, the influence of glucose deprivation and treatment with OxPhos modulators antimycin A and malonoben on the *extracellular acidification rates* was studied. Therefore, three different cell lines – MCF-7 cells, SK-Mel cells and U373 cells – were monitored over a course of 24 hours. The cells were either cultured under control conditions in L15 buffer supplemented with 4.5 g/L glucose, in pure L15 buffer without glucose, or under the influence of malonoben (100 nM) or antimycin A (2 µM). The results are depicted in Figure 43. In the first hours after the addition the pH decreased underneath cells cultured in all conditions. The extracellular pH of MCF-7 cells and SK-Mel cells treated with malonoben and antimycin A decreased faster and to lower values within the first hours of the experiment compared to the cells under control condition. In case of the U373 cells only addition of AntA resulted in a

stronger pH decrease compared to the control within the first 5 hours. After the first few hours, the further development of extracellular pH differed strongly for the individual conditions. Extracellular pH of cells cultured in L15 without supplements increased after reaching a minimum value for all cell types. Same holds true for cells cultured under the influence of antimycin A. The increase might result from the cell death induced by antimycin A (Ogita et al. 2009). The missing (anaerobic) cellular metabolism due to cell death or lack of glucose and the diffusion of the fresh medium towards the sensor surface resulted in the slow increase of the pH. In contrast, cells under control conditions in L15 supplemented with glucose and cells treated with malonoben did not show this increase. MCF-7 cells and SK-Mel cells continuously acidified the extracellular liquid during the measurement time. Both cell types reached the lowest pH value faster when treated with malonoben. U373 cells under control conditions and U373 cells treated with malonoben reached a constant equilibrium pH after approximately two hours. Malonoben as an uncoupler of the electron transport chain reduces ATP produced by the oxidative phosphorylation. In consequence, the cells react by an increased glycolytic rate and therefore an increased extracellular acidification (Turcios et al. 2020). The effect was stronger for the electron chain blocker antimycin A as these cells completely switch to glycolytic energy production whereas cells treated with the uncoupler malonoben only partly switch their phenotype (Mookerjee et al. 2017).

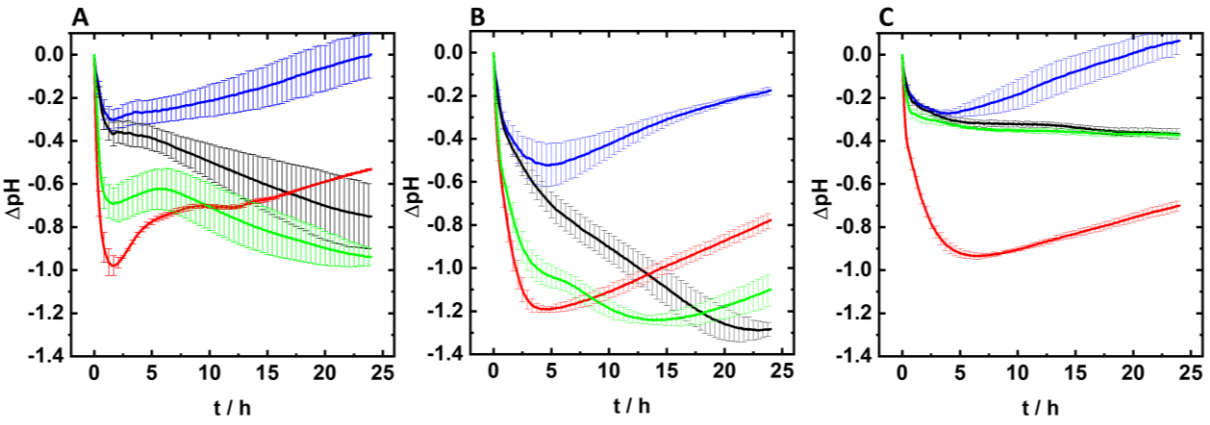

Figure 43: Monitoring of extracellular pH of cells cultured on permeable substrates (SFtl0.4). Time course of normalized extracellular pH of (A) MCF-7 cells, (B) SK-Mel 28 and (C) U373 cells treated with a **glucose supplemented L15 buffer used as control (+ 4.5 g/L glucose)**, **L15-buffer**, **malonoben (100 nM)** and **antimycin A (2 µM)**. pH was normalized to the value at t = 0 h. Data were obtained using the VisiSens TD area i imaging kit in a dry cell culture incubator at 37 °C and 0 % CO_2 (Mean ± SEM, n = 3).

To quantify these effects, the *extracellular acidification rates* for all conditions were calculated. The EAR results from the slope of the decrease within the first few hours of the measurement. Therefore, two different time frames with different temporal resolution were analyzed:

i) measurement time: 10 min; temporal resolution: 10 s

ii) measurement time: 30 min; temporal resolution: 1 min

The results are summarized in Figure 44, Figure 45 and Figure 46 for MCF-7 cells, SK-Mel cells and U373 cells, respectively. As already seen in the measurements over 24 hours, SK-Mel cells showed overall the highest basal *extracellular acidification rate* during the 10-minute frame followed by MCF-7 cells and U373 cells with 10.9 ± 0.3 mpH·min^{-1}, 8.4 ± 0.2 mpH·min^{-1}, and 7.2 ± 0.2 mpH·min^{-1} respectively. Same held true for the values found in the 30-minute time frame with 6.6 ± 0.1 mpH·min^{-1}, 5.3 ± 0.1 mpH·min^{-1}, and 4.23 ± 0.08 mpH·min^{-1}. The values found using our approach were in range of extracellular acidification rates reported before in literature for these cell lines a shown in Table 7 (Plitzko and Loesgen 2018; Agilent Technologies 2016; Hujber et al. 2018).

Table 7: Comparison of basal EAR values for MCF-7 cells, U383 MG cells and SK-Mel 28 cells to values reported in literature. EAR_{10min} is the EAR calculated from the linear decrease in the first 10 min of the measurement. EAR_{30min} is the EAR calculated from the linear decrease in the first 30 min of the measurement.

Cell Line	**EAR_{10min} / mpH·min^{-1}**	**EAR_{30min} / mpH·min^{-1}**	**$EAR_{Literature}$ / mpH·min^{-1}**	**Literature**
MCF7	8.4 ± 0.2	4.23 ± 0.08	15-20	(Agilent Technologies 2016)
U373 MG	7.2 ± 0.2	5.3 ± 0.1	4 - 13	(Hujber et al. 2018)
SK-Mel 28	10.9 ± 0.3	6.6 ± 0.1	10 - 15	(Plitzko and Loesgen 2018)

As depicted in Figure 44, depriving MCF-7 cells of glucose resulted in a marginal decrease of the extracellular acidification rate in both time frames of analysis. According to literature, a stronger influence of glucose deprivation on the *extracellular acidification rate* was expected. Glucose starvation leads to a metabolic reprogramming including the reduction of glycolysis (Ren and Shen 2019). A decreased contribution of glycolysis should lead to a decreased output in lactate and therefore a smaller change in pH. However, the cells were cultured in glucose containing medium until immediately before the measurement. In addition, L15 contains galactose providing an alternative carbon source for glycolysis. These factors might help the cells to overcome the lack of glucose for a certain period. As seen above, longer measurement times revealed that the extracellular acidification was weakened after about 5 hours for cells cultured in pure L15, which supports the given explanation. Malonoben treatment led to the

expected increase of the EACR values found for MCF-7 cells. The acidification rates increased 2-fold during the 10-min frame and almost 3-fold during the 30-min measurement period. Uncoupling of the oxidative phosphorylation led to a decreased energy output by oxidative phosphorylation which resulted in a switch of the cell towards a more glycolytic metabolism and therefore increased extracellular acidification (Samudio et al. 2009). Addition of antimycin A to MCF-7 cells resulted in 4.5-times higher acidification rates measured in the 10-min period and 4-times higher rates during the 30-min frame. The shut-down of the electron transport chain and the resulting lack of ATP-production required the cells to solely rely on energy produced by glycolysis which strongly increased the extracellular acidification (Hytti et al. 2019).

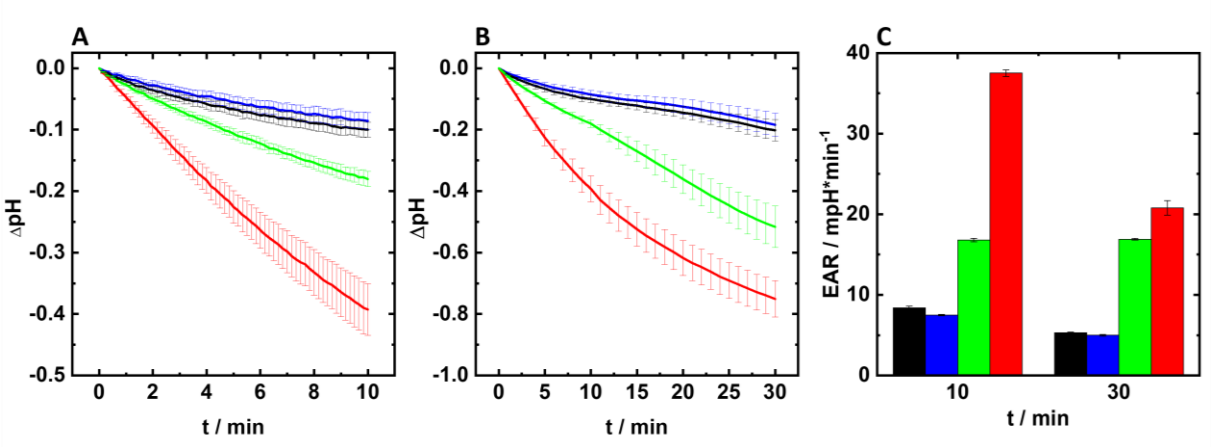

Figure 44: Comparison of different measurement intervals and time resolutions for monitoring of extracellular acidification of MCF-7 cells cultured on permeable substrates (SFtl0.4). Time courses of extracellular pH of MCF-7 cells monitored for (A) 10 min with an interval of 10 s and (B) 30 mins with an interval of 1 min. (C) Extracellular acidification rates of MCF-7 cells determined for the different measurement intervals. Cells were treated with a **glucose supplemented L15 buffer used as control (+ 4.5 g/L glucose)**, **L15-buffer**, **malonoben (100 nM)** and **antimycin A (2 µM)**. pH was normalized to the value at t = 0 h. Data were obtained using the VisiSens TD area i imaging kit in a dry cell culture incubator at 37 °C and 0 % CO_2 (Mean ± SEM, n = 3).

Similar trends were found for the treatment of SK-Mel 28 cells (Figure 45). Deprivation of glucose resulted in a slight but insignificant decrease of the extracellular acidification rates in both time frames. Addition of malonoben increased the acidifications rates by 1.8-fold and by 1.9-fold during the 10-min and 30-min periods, respectively. AntA treatment resulted in a 2.2-fold increase for both time frames. In comparison to the differences found for MCF-7 cells, the drug induced changes in SK-Mel cells were smaller which might result from overall different phenotypes of the cells.

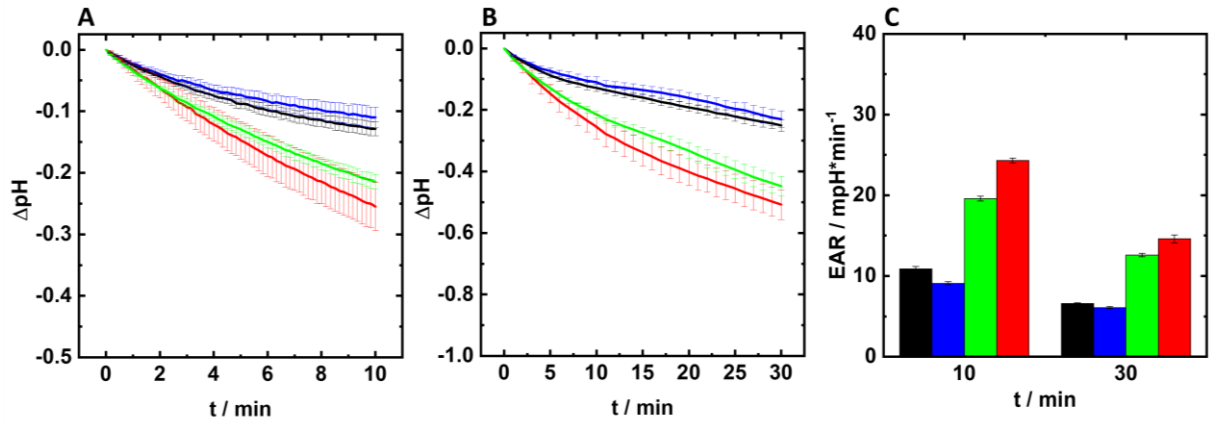

Figure 45: Comparison of different measurement intervals and time resolutions for monitoring of extracellular acidification of SK-Mel cells cultured on permeable substrates (SFtl0.4). Time courses of extracellular pH of SK-Mel cells monitored for (A) 10 min with an interval of 10 s and (B) 30 mins with an interval of 1 min. (C) Extracellular acidification rates of SK-Mel cells determined for the different measurement intervals. Cells were treated with a **glucose supplemented L15 buffer used as control (+ 4.5 g/L glucose)**, **L15-buffer**, **malonoben (100 nM)** and **antimycin A (2 µM)**. pH was normalized to the value at t = 0 h. Data were obtained using the VisiSens TD area i imaging kit in a dry cell culture incubator at 37 °C and 0 % CO_2 (Mean ± SEM, n = 3).

Finally, U373 cells were treated with the four culture conditions (Figure 46). In comparison to the other cells before, glucose deprivation did not lead to changes of the extracellular acidification rates. However, as already described before alterations in the time course of the pH were found after longer measurement times, suggesting that the cells were able to overcome the deprivation in the time frame under study. In the future a pre-incubation with medium deprived of glucose could overcome these issues by a phase of pre-equilibration. In contrast to the glucose deprivation, malonoben and antimycin A addition led to the expected changes in extracellular acidification characteristics. Malonoben treatment resulted in a 1.7-fold increase in the EAR during the 10-min frame and a 1.4-fold increase during the 30-min frame. Addition of antimycin A increased the acidification rates by 3-fold and by 2.6-fold for the 10-min and the 30-min time frame, respectively.

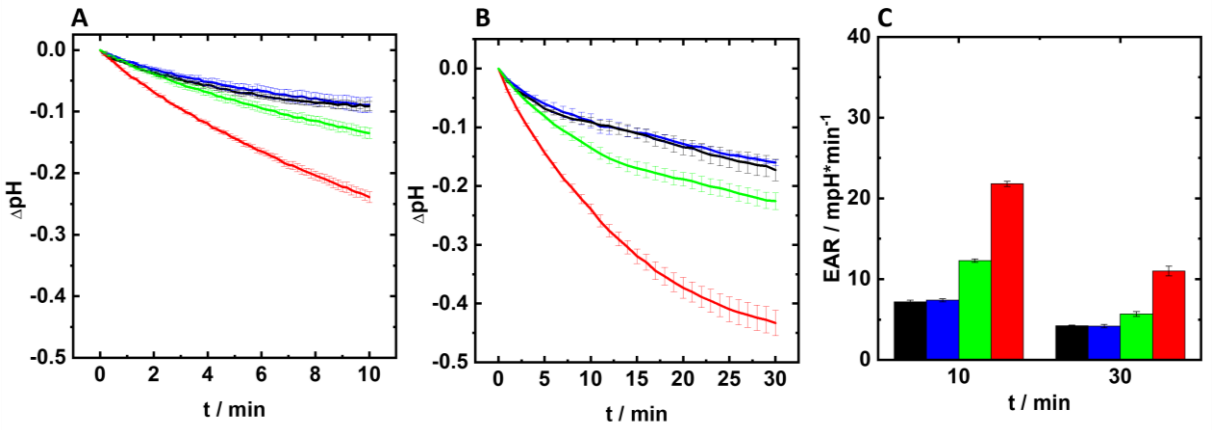

Figure 46: Comparison of different measurement intervals and time resolutions for monitoring of extracellular acidification of U373 cells cultured on permeable substrates (SFtl0.4). Time courses of extracellular pH of U373 cells monitored for (A) 10 min with an interval of 10 s and (B) 30 mins with an interval of 1 min. (C) Extracellular acidification rates of U373 cells determined for the different measurement intervals. Cells were treated with a **glucose supplemented L15 buffer used as control (+ 4.5 g/L glucose)**, **L15-buffer**, **malonoben (100 nM)** and **antimycin A (2 µM)**. pH was normalized to the value at t = 0 h. Data were obtained using the VisiSens TD area i imaging kit in a dry cell culture incubator at 37 °C and 0 % CO_2 (Mean ± SEM, n = 3).

In conclusion, a time frame of ten minutes was chosen for further experiments designed to determine extracellular acidification rates of 2D monolayers cultured on permeable substrates. In addition to the general trend associating shorter measurement times with enhanced efficiency, the relative changes upon treatment addition were either similar, only slightly smaller or even higher during the 10-min time frame compared to the 30-min period. The shorter time frame allows for shorter wait times between subsequent measurements over time and therefore a more effective workflow of the assay. Furthermore, changes in the extracellular pH itself can affect the cellular metabolism which in return may influence the determination of extracellular acidification rates (Pütz 2022; Teixeira et al. 2018; Fellenz and Gerweck 1988). Finally, the extracellular pH in the 30-min time frame especially for samples with higher acidification rates did not decrease linearly anymore resulting in worse linear fits important for the determination of accurate extracellular acidification rates for these conditions.

5.1.3 Sequential analysis of oxygen consumption and extracellular acidification

A proof of principle experiment was conducted to demonstrate sequential monitoring of extracellular acidification and oxygen consumption of a single population of cells cultured on a permeable substrate (SFtl0.4). Therefore, SK-Mel cells were seeded on permeable substrates and the pH was monitored using the same approach as depicted in chapter 5.1.2 using a 10-min observation time. After the 10-minute time frame used for pH monitoring, the filters were transferred to the oxygen sensor and partial oxygen pressure was monitored for 3 hours. The 3-hour frame was chosen based on previous experience with oxygen monitoring of 2D cell layers cultured on permeable substrates. The results were then further analyzed as described in chapter

3.3.4 and *extracellular acidification rates* as well as *apparent oxygen consumption rates* were determined. The trends found for both, the extracellular acidification and the respiratory rates were in line with the results obtained in individual experiments before. The influence of malonoben and antimycin A have already been discussed in preceding chapters in detail. However, it was now possible to address the influences for a single population of cells rather than analyzing individual populations. This allows direct correlation of the different phenotypes. Deprivation of glucose led to a slightly increased oxygen consumption and a reduced extracellular acidification. The AOCR for cells deprived from glucose (0.30 ± 0.07 pmol·(s·cell)$^{-1}$) where similar to the values found for cells cultured in L15 supplemented with glucose (0.24 ± 0.07 pmol·(s·cell)$^{-1}$). Extracellular acidification reduced from 13.4 ± 0.4 mpH·min^{-1} observed for cells cultured in glucose containing buffer to a value of 9.9 ± 0.3 mpH·min^{-1} for cells deprived of glucose. Lack of glucose generally results in a metabolic phenotype which is less glycolysis driven and therefore the observed changes in oxygen consumption and extracellular acidification (Ren and Shen 2019). As expected, uncoupling of the electron transport chain strongly enhanced oxygen consumption of the cells. The *apparent oxygen consumption rate* increased to 0.52 ± 0.06 pmol·(s·cell)$^{-1}$. At the same time, the *extracellular acidification rate* of the cells increased to a value of 20.5 ± 0.4 mpH·min^{-1}. It has been reported that cells react to the decreased energy output of the oxidative phosphorylation in two ways. First, the cells try to restore the H^+-ion gradient along the inner mitochondrial membrane driving the ATP-synthase by an enhanced oxygen uptake. Secondly, the decreased energy gained by oxidative phosphorylation leads to a higher glycolytic rate which resulted in a higher acidification of the extracellular surroundings observed in the experiment (Plitzko and Loesgen 2018; Samudio et al. 2009). Complete blockage of the electron transport chain by addition of antimycin A is generally followed by a switch to an energy production relying on high glycolytic rates, as the oxidative phosphorylation is not functional anymore (Mazibuko-Mbeje et al. 2021; Hytti et al. 2019). Consequently, we observed an enhanced extracellular acidification for the cells treated with AntA, 28.5 ± 0.5 mpH·min^{-1}, compared to the cells cultured under the other conditions. The oxygen consumption of the cells was shut down which resulted in an increase of the partial oxygen pressure to cell-free levels around 149 torr. Therefore, calculation of *apparent oxygen consumption rates* was impossible and the AOCR was set to 0 pmol·(s·cell)$^{-1}$.

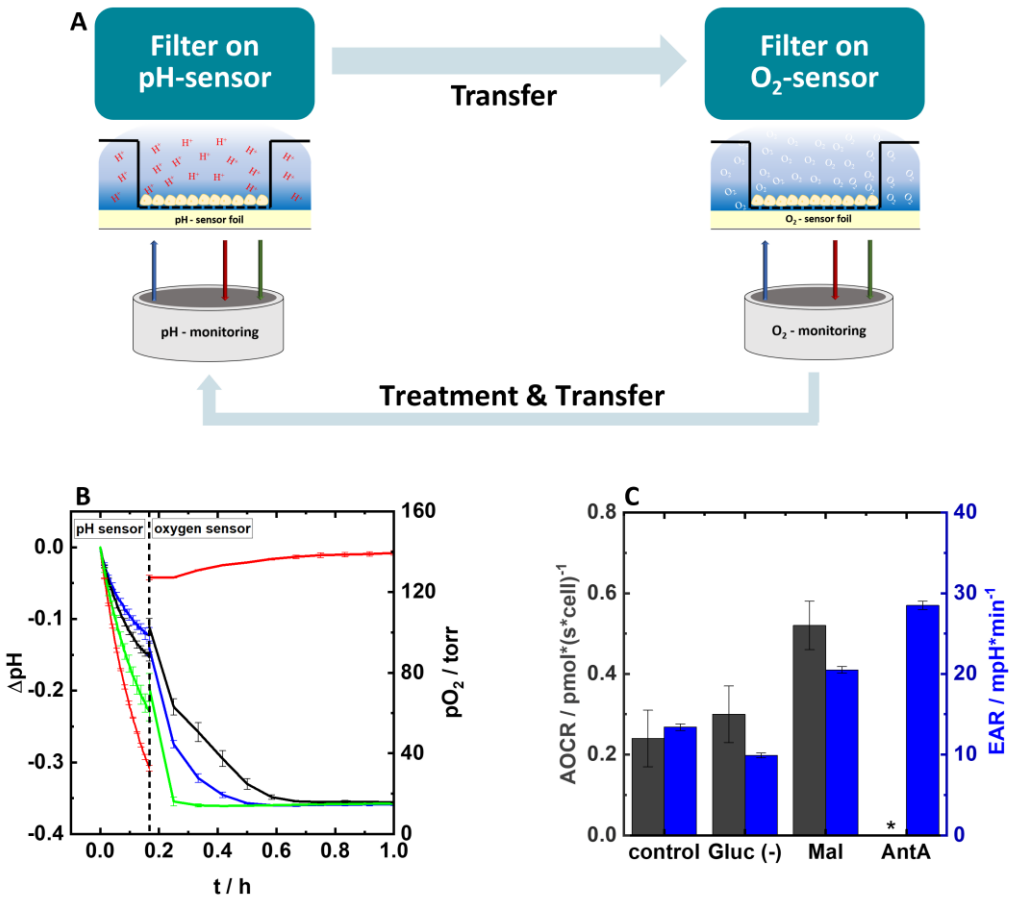

Figure 47: Sequential analysis of extracellular acidification and respiratory activity of SK-Mel cells. (A) Schematic of the process applied for sequential monitoring of extracellular pH and extracellular oxygen levels of 2D cell layers cultured on permeable substrates (SFtl0.4). (B) Time resolved pH changes and partial oxygen pressure of SK-Mel cells cultured on permeable filter substrates. Cells were treated with a **glucose supplemented L15 buffer used as control (+ 4.5 g/L glucose)**, **L15-buffer**, **malonoben (100 nM)** and **antimycin A (2 µM)**. Substrates initially placed on the pH sensor and pH was measured for 10 minutes. Afterwards cells were transferred to the oxygen sensor and partial oxygen pressure was monitored for 3 hours. (C) *Apparent oxygen consumption rate* and *extracellular acidification rate* resulting from the time courses shown in (A). Data were obtained using the VisiSens TD area i imaging kit in a dry cell culture incubator at 37 °C and 0 % CO_2 (Mean ± SEM, n = 3).

5.2 Monitoring of pH gradients underneath tumor spheroids

In the next step the concept of monitoring extracellular pH was transferred to 3D cellular aggregates, monitoring tumor spheroids. Therefore, tumor spheroids of the two tumor cell lines, MCF-7 cells and SK-Mel 28 cells, were cultured directly on a pH sensor foil. The spheroids were treated with electron transport chain modulator antimycin A. In addition, spheroids of SK-Mel cells were cultured on permeable filter substrates and the results were compared to the direct approach. In a last experiment the idea of sequential analysis of partial oxygen pressure and extracellular pH was expanded from 2D cell layers to tumor spheroids cultured on permeable substrates.

5.2.1 pH mapping underneath tumor spheroids cultured directly on the sensor foil

Accumulation of metabolic waste in the inner zones of a tumor spheroid leads to a pH gradient within the cellular aggregate. To analyze these gradients in more detail we cultured MCF-7 spheroids and SK-Mel 28 spheroids directly on a pH sensitive sensor foil glued into a 96-well cell culture plate. Before spheroid placement, the sensor foil was incubated overnight in L15 buffer allowing the hydrogel to swell. The pH gradients underneath the spheroids were subsequently monitored using the VisiSens TD mic setup. The resulting pH distribution maps are depicted in Figure 48 A and B. Both spheroids acidified the medium, creating a detectable pH footprint visible in the pH maps. The acidification can be seen in more detail in the lateral pH profiles (cross-sections) gained from the pH distribution maps. pH levels gradually decreased towards the center of the spheroids and both spheroids acidified their center region by approximately 0.5 pH points. Similar pH differences have been found before for other tumor cell lines forming spheroids in the same size range using invasive microneedles. Acker et al. and Gorlach et al. found pH changes of around 0.5 in spheroids formed by HT29 cells, U118MG cells as well as C6 cells, ranging from 600 µm to 900 µm in size (Acker et al. 1987b; Gorlach et al. 1995). However, the overall pH levels found for the two cell lines were different. In case of the MCF-7 spheroids, the basal pH surrounding the spheroid was approximately 7.5 and the pH in the center region reduced to approximately pH = 7.0. For the SK-Mel cells, a surrounding pH value of around pH = 7.0 was found. The pH underneath the center of the spheroid was reduced to pH = 6.5. These findings could result from different acidification rates of the cells within the spheroid. After the transfer of the spheroids onto the sensor foil, the spheroids were incubated for 24 hours for attachment to the sensor foil. The spheroids were imaged in the buffer used during the attachment phase as a medium exchange often detached the spheroids from the sensor foil. In chapter 5.1.2 we observed higher acidification rates for SK-Mel cells in comparison to MCF-7 cells in 2D cell culture. Presuming that the enhanced acidification rate

translates to cells cultured in spheroids, these findings support the explanation outlined above. In general, the pH profiles and maps seemed to be noisier in comparison to the oxygen maps and profiles presented in this work. This might be explained by a more heterogenous distribution of fluorophores within the hydrogel of the pH sensor foil compared to the polymer matrix used for oxygen sensing.

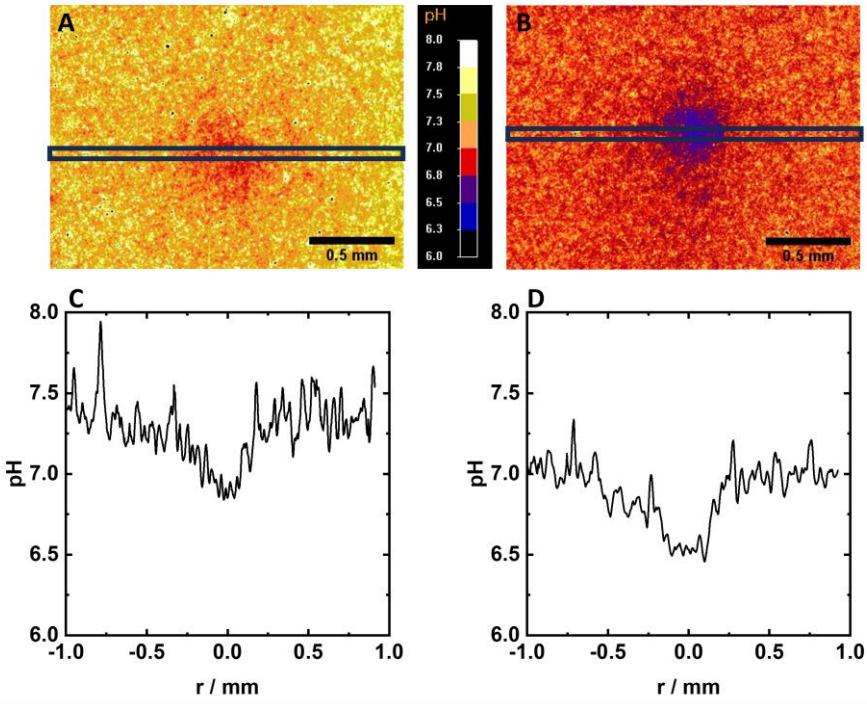

Figure 48: Ratiometric optical pH imaging of tumor spheroids cultured directly on the sensor foil surface. pH distribution map and lateral pH profile of spheroids formed by MCF-7 cells (A&C) and SK-Mel 28 cells (B&D). (A&B) Scalebar: 0.5 mm. (B&D) ROIs used to determine lateral pH profiles. MCF-7 cells were seeded at an initial cell number of $20 \cdot 10^3$ cells and SK-Mel cells at an initial cell number of $12 \cdot 10^3$ cells using the liquid-overlay technique. Spheroids were grown for 6 days and afterwards transferred to the pH sensor foil. After attachment for 24 hours, data were recorded using the VisiSens TD mic setup in a dry cell culture incubator at 37 °C and 0 % CO_2.

In a second step, the spheroids were exposed to antimycin A (2 µM) directly before the measurement. The spheroids were allowed to attach under control conditions in L15 buffer and antimycin A was added with extreme care to prevent the detachment of the spheroids. As already explained in chapter 5.1.2, antimycin A addition generally leads to an increased extracellular acidification by blocking the electron transport chain. The lateral pH profiles are shown in Figure 49. The increase of extracellular acidification was observed for both cell lines. The profiles resulting from cells treated with AntA were more pronounced. Spheroids formed by MCF-7 cells treated with AntA decreased the pH by approximately 0.7 in comparison to 0.5 pH points when cultured in the control buffer. The same change was found for SK-Mel cells. In addition, the general change of the pH in the medium from pH = 7.5 for MCF-7 cells and pH = 7.0 for SK-Mel cells was observed again.

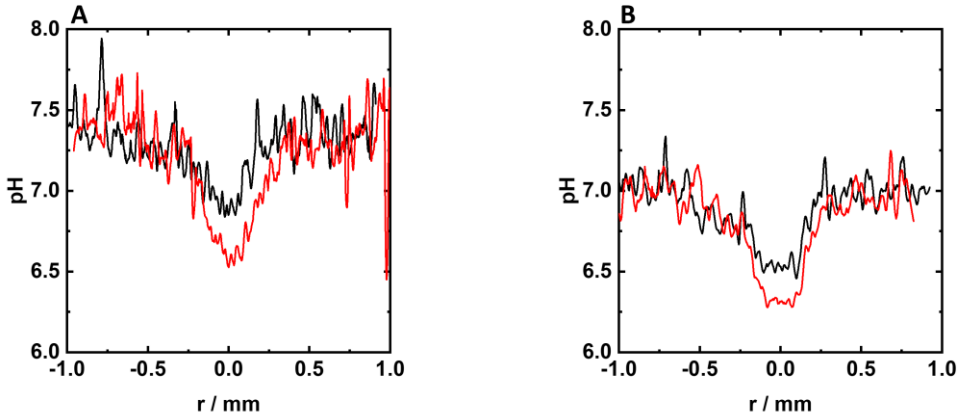

Figure 49: Treatment of spheroids with electron chain blocker antimycin A. Lateral pH profiles of a (A) MCF-7 spheroid and (B) a SK-Mel-spheroid treated with **L15 (+ glucose 4-5 g/L)** or **antimycin A (2 µM)**. MCF-7 cells were seeded at an initial cell number of $20 \cdot 10^3$ cells and SK-Mel cells at an initial cell number of $12 \cdot 10^3$ cells using the liquid-overlay technique. Spheroids were grown for 6 days and afterwards transferred to the pH sensor foil. After attachment for 24 hours, data were recorded using the VisiSens TD mic setup in a dry cell culture incubator at 37 °C and 0 % CO_2.

5.2.2 pH mapping underneath tumor spheroids cultured on permeable substrates

The next step was to culture the spheroids on filter substrates and to compare the results with the direct approach. Therefore, SK-Mel spheroids seeded at an initial cell number of $12 \cdot 10^3$ cells were transferred on the SFtl0.4 filter or directly onto the sensor foil after 6 days and analyzed using the VisiSens TD mic system. We chose to use the SFtl0.4 filter type based on the observations described for oxygen monitoring of spheroids in chapter 4.2.1. To compare both approaches, the lateral pH profiles are depicted in Figure 50. The lateral profile obtained for the spheroid cultured on the permeable substrate is indistinguishable from the results obtained via the direct approach. Both culture methods led to a reduction of the pH towards the center of the spheroid by approximately 0.5 pH units. Therefore, the filter approach was well suited to use for further experiments monitoring SK-Mel spheroids in particular for measuring EAR and AOCR of the same spheroid.

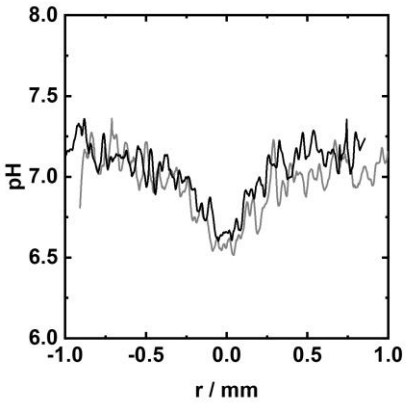

Figure 50: Comparison of lateral pH profiles from SK-Mel spheroids cultured **directly on the sensor foil** and on a **permeable substrate (SFtl0.4)**. SK-Mel cells were seeded at an initial cell number of $12 \cdot 10^3$ cells using the liquid-overlay technique and spheroids were grown for 6 days. Afterwards spheroids were transferred to the pH sensor foil or the SFtl0.4 filter substrate. After attachment for 24 hours, data were recorded using the VisiSens TD mic setup in a dry cell culture incubator at 37 °C and 0 % CO_2.

To show that the filter approach is also suitable to determine drug induced changes on the *extracellular acidification rate* of tumor spheroids, SK-Mel spheroids were treated with the electron transport chain blocker antimycin A. After the 24-hour attachment phase, the spheroids were either treated with L15 (+ glucose 4.5 g/L) as control condition or antimycin A (2 µM) in control buffer. As expected, AntA treatment resulted in an increased acidification of the extracellular environment which can be observed in the more pronounced lateral pH profiles measured for spheroids treated with AntA (see Figure 51 A). However, the changes were not as pronounced as in the direct approach. In addition to the lateral pH profiles, it is possible to determine the development of the pH underneath an attached tumor spheroid over time. The time courses are depicted in Figure 51 B. Extracellular pH of cells treated with AntA decreased

faster and to lower pH values after 1 h of measurement time. *Extracellular acidification rates* were determined from the time courses. EAR increased from 13.3 ± 0.7 mpH·min^{-1} for spheroids cultured in the control, to and EAR of 25.0 ± 0.6 mpH·min^{-1} measured for spheroids under the influence of antimycin A. This was in line with the results found for the lateral profiles.

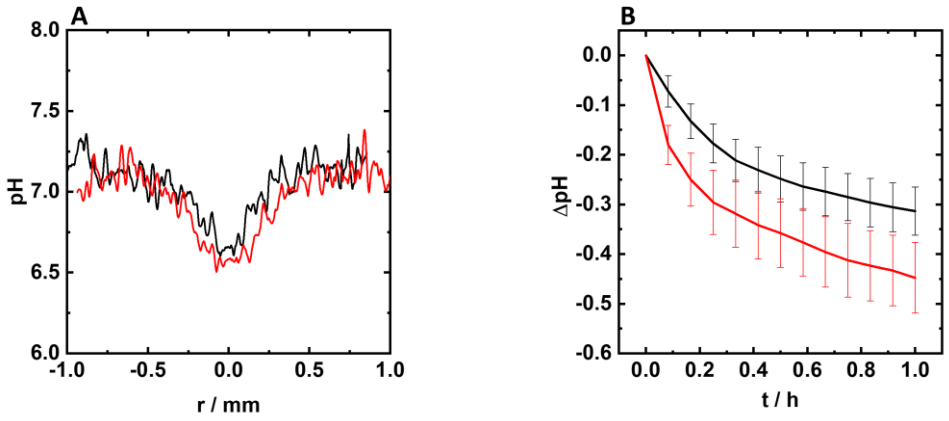

Figure 51: Treatment of SK-Mel spheroids with electron chain blocker antimycin A. (A) Lateral pH profiles and (B) pH time courses (Mean ± SEM, n = 3, pH values were normalized to the pH at time point t = 0 h) of SK-Mel spheroids treated with **L15 (+ glucose 4-5 g/L)** or **antimycin A (2 µM)**. SK-Mel cells were seeded at an initial cell number of 12·10^3 cells using the liquid-overlay technique and spheroids were grown for 6 days and afterwards transferred to the SFtl0.4 filter substrate. After attachment for 24 hours, data were recorded using the VisiSens TD mic setup in a dry cell culture incubator at 37 °C and 0 % CO_2.

Similar to the analysis of the aerobic profile from different, independent parameters of oxygen consumption an anaerobic profile was developed, combining temporal and spatial results of the pH monitoring approach. Time course data was represented by the global extracellular acidification rates. In addition, the lateral pH profile was evaluated similar to the approach described for oxygen. Differences of the pH were calculated at the two distinct positions $r^0 = 0$ mm and $r^+ = 0.1$ mm of the lateral pH profile relative to a bulk pH of 7.4 resulting in the values ΔpH(0) and ΔpH(0.1), respectively. Additionally, the FWHM was determined. These values were combined with the EAR value and are depicted in the anaerobic profile in Figure 52. An increase in the area enclosed by the anaerobic profile correlated with an increase in extracellular acidification. The increased area found for the spheroids treated with antimycin A indicated enhanced extracellular acidification, which was in line with the mechanism of action of this compound. However, in comparison to the graphs above, the anaerobic profile showed the results in combination and provides a comprehensive integration of spatial and temporal information within one graph as a unique way of data presentation. The larger the enclosed area of the anaerobic profile, the stronger the extracellular acidification of the analyzed spheroid under study.

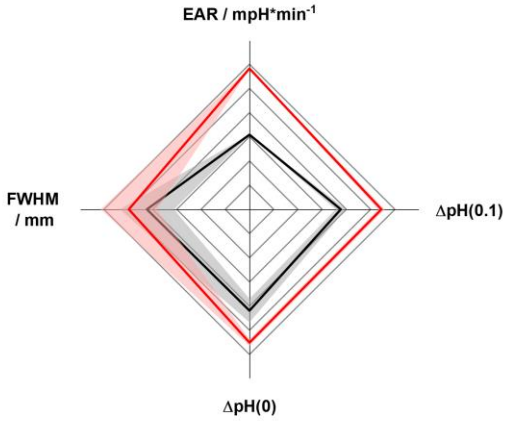

Figure 52: Treatment of SK-Mel spheroids with electron chain blocker antimycin A. Anaerobic profile of SK-Mel spheroids treated with **L15 (+ glucose 4-5 g/L)** or **antimycin A (2 µM)**. SK-Mel cells were seeded at an initial cell number of $12 \cdot 10^3$ cells using the liquid-overlay technique and spheroids were grown for 6 days. Afterwards spheroids were transferred to the SFtl0.4 filter substrate. After attachment for 24 hours, data were recorded using the VisiSens TD mic setup in a dry cell culture incubator at 37 °C and 0 % CO_2 (Mean ± SEM, n = 3).

5.2.3 Sequential analysis of oxygen and pH gradients underneath tumor spheroids

The concept of sequential monitoring of extracellular acidification and oxygen consumption was applied to SK-Mel spheroids. Therefore, SK-Mel spheroids initially formed from $12 \cdot 10^3$ cells were cultured on a permeable filter substrate (SFtl0.4). The filter holding the SK-Mel spheroid was then placed upon the oxygen sensor for monitoring aerobic respiration, before it was placed on the pH sensor for monitoring extracellular acidification. After supplementation of antimycin A (2 µM) this procedure was repeated (Figure 53 A). The procedure provided both, an aerobic and an anaerobic profile, for the same tumor spheroid, enabling detailed evaluation and correlation of respiratory activity and glycolytic activity and the resulting metabolic phenotype of the cells within the spheroid (Figure 53 B & C). As described before, addition of antimycin A led to a shutdown of the electron transport chain and therefore a lack of energy production via oxidative phosphorylation. To meet the energy demand, the cells switched to anaerobic energy production mainly relying on enhanced glycolytic rates. Glycolysis as a main driver of extracellular acidification resulted in the enhanced extracellular acidification indicated by the enlargement of the relative area enclosed by the anaerobic profile of spheroids treated with AntA (65 %) in comparison to spheroids cultured in the L15 buffer control (27 %). At the same time, the experiments showed the expected decrease in oxygen uptake as the aerobic profile almost vanished for cells treated with AntA, resulting in a relative area of 0 %. The sequential analysis of aerobic and anaerobic characteristics of the spheroids offers the possibility to create a metabolic profile of spheroids. The metabolic profile is the combination of the aerobic and the anaerobic profile and is shown in Figure 53 D for the SK-Mel spheroid described above. The ratio between area covered by the aerobic parameters and the area covered

by the anaerobic parameters describes the metabolic phenotype of the spheroid. Higher values result from a metabolism based on aerobic processes, while lower values describe an anaerobic phenotype. As expected, the ratio of the SK-Mel spheroid strongly decreased after AntA treatment. While spheroids under control conditions showed a ratio of 1.16, the ratio reduced to 0.0006 after addition of antimycin A. The experiment served as proof-of-principle of the presented assay platform capable of monitoring the energy-producing phenotypes of cells cultured as tumor spheroids.

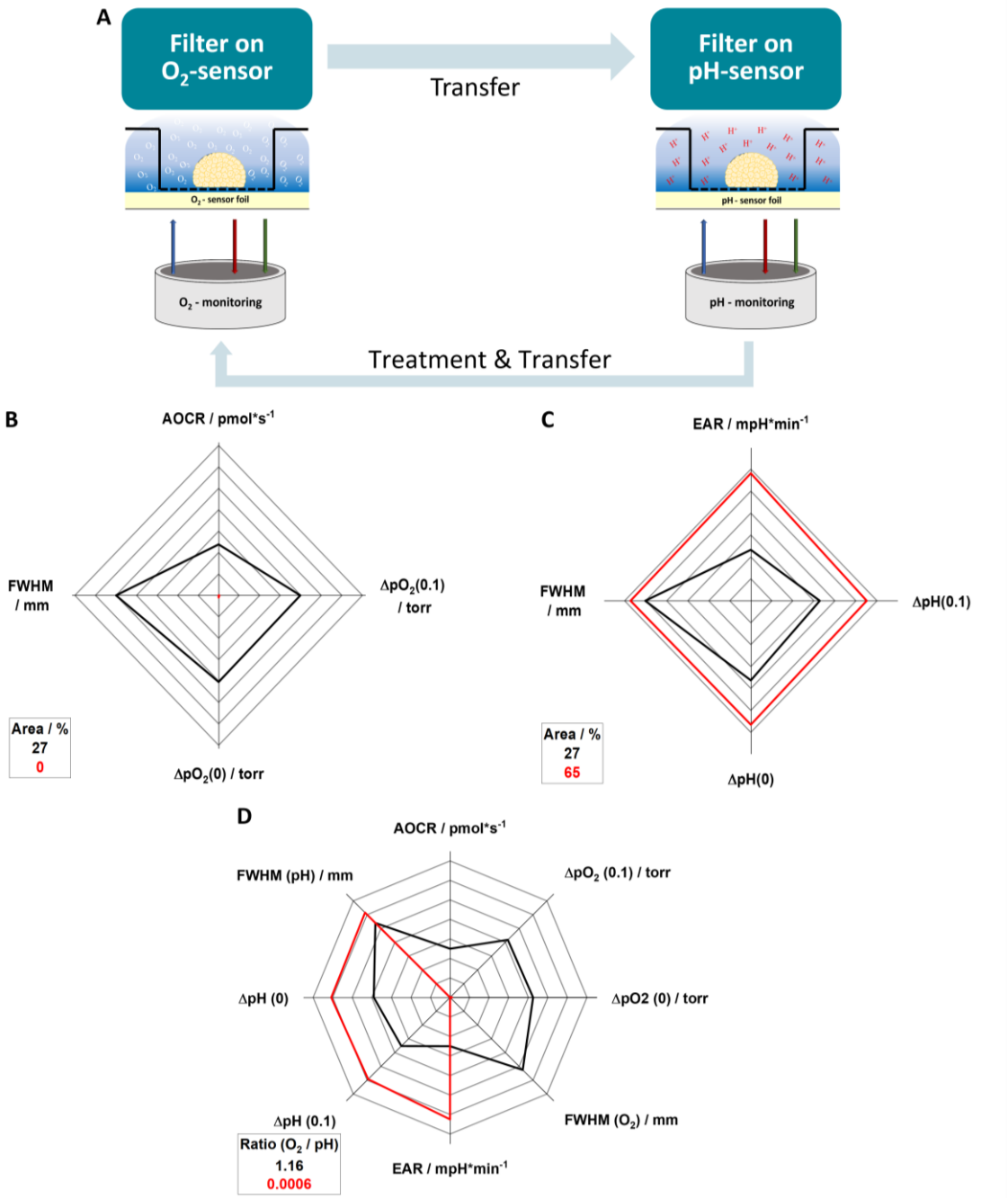

Figure 53: Sequential analysis of oxygen consumption and extracellular acidification of a tumor spheroid. (A) Workflow of sequential analysis of extracellular pH and dissolved oxygen underneath a tumor spheroid cultured on a permeable substrate. (B) Aerobic profile, (C) anaerobic profile and (D) metabolic profile of a SK-Mel spheroid treated with **L15 (+ glucose 4-5 g/L)** or **antimycin A (2 µM)**. SK-Mel cells were seeded at an initial cell number of $12 \cdot 10^3$ cells using the liquid-overlay technique and spheroids were grown for 6 days. Afterwards spheroids were transferred to the SFtl0.4 filter substrate. After attachment for 24 hours, data were recorded using the VisiSens TD mic setup in a dry cell culture incubator at 37 °C and 0 % CO_2.

5.3 Conclusion & Outlook

The experiments of the previous chapter showed that ratiometric optical imaging is a valid tool to determine the extracellular acidification of 2D cell layers cultured on permeable substrates. The *extracellular acidification rate* for three different cell lines, MCF-7 cells, U373 cells and SK-Mel cells cultured on permeable substrates was successfully determined. The cells were furthermore treated with modulators of the oxidative phosphorylation, antimycin A and malonoben. pH monitoring of the treated cells was performed over the course of 24 hours. Thereby different time periods for the determination of the extracellular acidification rate were compared. A measurement period of only 10 minutes was sufficient to resolve the *extracellular acidification rate* resulting from drug treatment. Finally, a sequential analysis of extracellular acidification and oxygen consumption of the cell layers cultured on permeable substrates was generally possible. Therefore, a monolayer of SK-Mel cells was grown on permeable substrates and the dissolved oxygen as well as the extracellular acidification was monitored under the influence of glucose deprivation, antimycin A and malonoben. To the best of our knowledge, this is the first approach enabling the in-detail characterization of cellular metabolism for cells cultured on permeable substrates.

In addition to the 2D approach, ratiometric optical pH mapping laid the experimental foundation for the use of VisiSens TD as a tool for the analysis of extracellular acidification of 3D tissue models. It was shown in this thesis that it is possible to determine pH gradients formed in tumor spheroids using ratiometric optical pH mapping. MCF-7 and SK-Mel spheroids cultured on the sensor foil (direct approach) were analyzed regarding their *extracellular acidification rates* under control conditions and under the influence of electron transport chain blocker antimycin A. The pH gradients within the spheroids as well as the AntA induced changes were in line with results reported before by others using invasive methods. In a final step, spheroids cultured on permeable substrates were monitored by VisiSens TD. The results showed that the lateral pH profiles found for SK-Mel spheroids cultured on permeable substrates were indistinguishable from the results found for SK-Mel spheroids cultured directly on the sensor foil. The results of the spatial analysis and the temporal analysis were combined to form the newly developed anaerobic profile of tumor spheroids. The maps were subsequently used to determine AntA induced changes on the extracellular acidification of the spheroids. In a proof-of-principle experiment the idea of a platform technology determining respiratory activity and extracellular acidification of the same cell model was transferred to tumor spheroids cultured on permeable substrates. Therefore, a SK-Mel spheroid was applied to a permeable filter substrate. The spheroid was then analyzed regarding the extracellular acidification and the

oxygen consumption in subsequence to each other. As already presented for 2D layers this offered the possibility to determine the metabolic phenotype of the cells within the tumor spheroid. This was shown by the analysis of drug induced changes of AntA using the described assay platform. The results depicted as novel metabolic map were in line with the trends reported in literature.

Future research might aim to further develop the sequential analysis of 2D cell layers. Therefore, the measurement time of the oxygen monitoring might be reduced to periods shorter than the three-hour measurement conducted in the experiments so far. For further validation, the assays principle has to be applied to additional cell lines. In addition, a closer look into the results obtained for cells deprived of glucose will be necessary. A pre-incubation period in glucose free medium might lead to the expected influence of glucose deprivation. This theory was supported by the decreased extracellular acidification of these cells during the 24-hour time frame. Finally, a substance reducing the extracellular acidification such as 2-Desoxy-D-glucose should be applied to show that also drugs inhibiting the extracellular acidification can be characterized. Analysis of tumor spheroids cultured directly on the sensor foil and on filter substrates using ratiometric optical imaging has to be expanded to additional cell lines, varying seeding densities as well as different spheroid sizes as previously shown for oxygen consumption measurements in chapter 4.2. Moreover, additional substances should be tested. In general, the method currently suffers from a low throughput rate which needs improvement in future approaches. To improve the throughput the camera setup could be adjusted (see chapter 4.2.5). Moreover, it might be possible to develop a setup with a movable sample holder. Thereby, several filters containing the spheroids could be analyzed using the same setup. The use of the filter assay offers the possibility to expand the workflow to further analytes, such as glucose or lactate readings or impedimetric analysis of the spheroids. However, it would be necessary to develop suitable sensor principles for further analytes as well as a (semi-) automized transfer of the permeable substrates between the different sensors. The expansion to further analytes could strongly enhance the information of depth accessible with label-free and time resolved analysis approaches.

6 TER-Ox: Simultaneous monitoring of epithelial barrier function (TER) and respiration (Ox)

The data shown in chapters 6.1 and 6.2.1 as well as the TER-Ox setup including the novel TER-ox chamber have been published during the course of this thesis (Naber et al. 2025). Description, interpretation and figures in the following chapters were mostly adopted from this publication.

Alterations in epithelial barrier function and cellular respiration are hallmarks in many pathological disorders. Accordingly, the molecular drivers are targeted extensively in drug development using appropriate disease models *in vitro*. A prominent example is the epithelial-to-mesenchymal-transition, which is a main driver of cancer metastasis and fibrosis (Kalluri and Weinberg 2009; Lovisa 2021). So far, quantification of barrier function and metabolic respiration had to be conducted in individual phenotypic assays, making it impossible to track changes simultaneously in the same population over longer periods. To determine both of these parameters on a single cellular model the TER-Ox platform was developed.

6.1 Establishment of the TER-Ox platform

6.1.1 Characterization of different cell types using TER-Ox

In order to demonstrate the functionality of the TER-Ox assay using the novel platform, three epithelial cell lines with different barrier function have been studied:

i) A549 cells
ii) MDCK-II cells
iii) MDCK-I cells

A549 cells form leaky barriers and are widely used in assays investigating mitochondrial respiration. TER-values of around 6 Ωcm^2 were observed in this thesis for mature cell monolayers (Figure 54) which is in line with literature, reporting TER values below 30 Ωcm^2 (Hermanns et al. 2004; Ren et al. 2016). Quantification of the *transepithelial electrical capacitance* resulted in values around 1.4 $\mu F/cm^2$ indicating expression of membrane protrusions like microvilli or invaginations (Figure 54 F). Independently of the cell type, an entirely flat membrane shows a membrane capacitance of 1 $\mu F/cm^2$ (Wegener et al. 2004). The current has to pass two membranes on the transcellular path across the cell layer - namely the apical and the basal membrane. Since the two membrane capacitances C_{Ap} and C_{bl} are in series, the total capacitance of a *cell layer* with entirely flat membranes TEC is 0.5 $\mu F/cm^2$ (1/TEC =

$1/C_{Ap} + 1/C_{bl}$). These TEC values have been often found for endothelial cells (Wegener et al. 2004; Wegener et al. 1999). If we now assume, that both membranes contribute equally, a cell layer capacitance of TEC = 1.4 µF/cm^2 as found for A549 cells translates to an average membrane capacitance of $C_{ap} = C_{bl} = 2.8$ µF/cm^2 for apical and basolateral membranes, respectively. Additionally, membrane capacitance is not affected significantly by other parameters standardized in animal cell culture (Gentet et al. 2000). Therefore, since capacitance scales with the area, either side of the membrane surface area is enlarged approximately three times compared to its "footprint". These enlargements are typically found for transporting epithelia (Wegener et al. 1999).

The time resolved data for the second cell line, MDCK-II cells, are shown in Figure 54 B. As described previously, MDCK-II cells are heavily used as model for moderately tight barriers and active transcellular solute transport (Dukes et al. 2011). Formation of moderately tight barriers was confirmed using the TER-Ox setup, resulting in TER values around 50 Ωcm^2 which is slightly lower than published values but still in the same order of magnitude (Urban et al. 2020; Hajek and Wegener 2017). The average *transepithelial electrical capacitance* was quantified to TEC = 1.7 µF/cm^2 which is even higher than observed for the A549 cells but again slightly lower than reported in literature (Urban et al. 2020; Hajek and Wegener 2017). Experience of our working group shows that MDCK-II cells are easy to grow and maintain in culture for weeks or even months without re-starting the culture from a fresh cryopreserved stock culture. However, TER and TEC values may drift or scatter along an extended time in culture for reasons that one can only speculate about. Thus, an independent impedance analysis with established devices of all cell lines under study was performed to ensure correct readings with the TER-Ox device. The results are shown in chapter 6.1.2.

The last cell line, MDCK-I cells, are commonly used to mimic tight epithelial barriers resulting in high TER values and low permeability coefficients (Stevenson et al. 1988). Accordingly, TER-Ox studies returned by far the highest TER values for MDCK-I cell layers. After a strong decrease of the TER in the first 2 hours of a typical time course experiment, values equilibrate around 1400 Ωcm^2 (Figure 54 C). To the best of our knowledge, this initial strong decrease in TER from more than 5000 Ωcm^2 to 1400 Ωcm^2 shortly after the cells have been transferred into the TER-Ox setup, is a response of the cells to (i) liquid handling, (ii) the inevitable change of incubation buffers from serum-containing cell culture medium to L-15 minimal medium together with (iii) the associated temperature disturbances. MDCK-I cells responded dramatically to a change of the incubation buffer and the L-15 medium had to be supplemented with 4.5 g/L glucose for cell layer stabilization. Without the addition of glucose, the TER values

dropped continuously below 1000 Ωcm^2 (Supplementary information, chapter 11.1, **Figure S 12**). However, the change of incubation buffer was necessary since measurements with the TER-Ox setup in our lab currently require a CO_2 free atmosphere and buffer systems adapted thereto. Similar results were obtained when an independent impedance analysis device (cellZscope®) was used. These studies returned similar time courses for MDCK-I cells (supplementary information, chapter 11.1, **Figure S 11**). TEC of MDCK-I cell layers was quantified to 1.6 µF/cm² on average. It is slightly lower than TEC of MDCK-II cells as reported before (Hajek and Wegener 2017).

The time courses of the oxygen partial pressure pO_2 showed a similar curve characteristic for all three cell lines starting at values of cell culture fluid fully equilibrated with ambient air (app. 120 torr). Differences for the individual cell lines arose in the slope of the time course within the first 4 hours as well as the equilibrium values (Figure 54). As indicted in Figure 11, the *apparent oxygen consumption rate* (AOCR) is individually determined from the slope of the linear part of the curve after the temperature-induced transient maximum. AOCR for A549 cells amounted to 25.1 ± 0.6 amol·(s·cell)$^{-1}$. MDCK-II cells showed an average oxygen consumption rate of 37 ± 5 amol·(s·cell)$^{-1}$. Measurements returned a rather similar respiration rate for MDCK-I as for MDCK-II cells, which is 38 ± 8 amol·(s·cell)$^{-1}$. These AOCRs were all within the range of results reported in literature. The values indicated for all three cell lines that their energy consumption relies to a significant part on aerobic metabolism (Wagner et al. 2011; Molter et al. 2009).

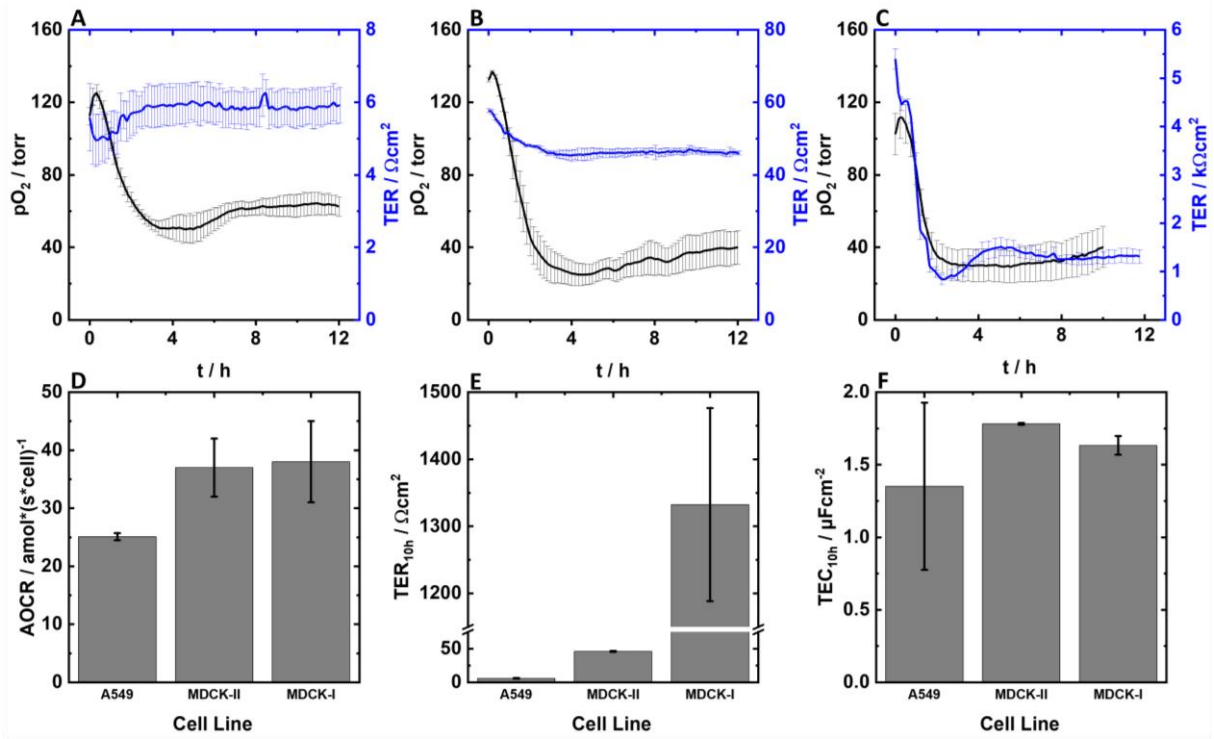

Figure 54: Simultaneous monitoring of epithelial barrier function and respiratory activity of A549, MDCK-II and MDCK-I. Partial oxygen pressure (**black**) and transepithelial electrical resistance (**blue**) time courses of (A) A549 cells, (B) MDCK-II cells and (C) MDCK-I cells. (D) Apparent oxygen consumption rates, (E) TER values at t = 10 h and (F) TEC after t = 10 h of A549 cells, MDCK-II and MDCK-I cells. (D) – (F) were extracted from the time courses shown in (A) – (C). TER and pO_2 were monitored simultaneously using the TER-Ox setup in a dry cell culture incubator at 37 °C and 0 % CO_2 (Mean ± SEM, n=3).

6.1.2 Comparison of TER-Ox to established platforms

For further validation of the results measured with TER-Ox, the values for AOCR, TER and TEC were compared to data recorded with established commercial devices: (i) VisiSens TD for respiration and (ii) cellZscope® for barrier integrity and membrane capacitance. The apparent oxygen consumption rates reported by TER-Ox were in line with the results found by VisiSens TD monitoring supporting the hypothesis that neither oxygen monitoring nor the cellular respiration were affected by the presence of stainless-steel electrodes or other elements of the TER-Ox setup (Figure 55 A). TER values of A549 and MDCK-II cells obtained in TER-Ox experiments were also in agreement with corresponding cellZscope® assays (Figure 55 B). It is important to note, that TER values respond very sensitive to slight mechanical disturbances, temperature drifts or any kind of liquid handling. In comparison to the pool of TER values of these two cell lines recorded in our laboratory, the observed differences were within regular data scattering recorded with different devices. For MDCK-I cells, significant differences between TER values recorded with TER-Ox or cellZscope® were observed. However, as already described above, TER is rather sensitive to slight variations in experimental parameters. This holds particularly true for very tight epithelial or endothelial cell layers with high TER values. Similar observations have been made for endothelial cells derived from brain capillaries

forming blood-brain barrier *in vivo* (Hoheisel et al. 1998) or other tight barrier forming cell species. This can be seen by looking at the time course of the TER readings reported in Figure 54 C. Immediately after introducing the cell-covered filter inserts into the TER-Ox setup, TER values of the MDCK-I cells were close to 5 kΩcm^2. During equilibration, the values decreased and stabilized around 1.3 kΩcm^2. At the same time, the oxygen consumption was not significantly different compared to MDCK-I cells studied independently in the VisiSens setup indicating that the cells have not been treated differently compared to other assays. Despite the differences found for MDCK-I cells, the general trend of TER values was similar for both methods clearly distinguishing between low (A549), moderate (MDCK-II) and tight (MDCK-I) barrier function.

Comparing the cell layer capacitances, differences in the values measured for A549 cells were found, whereas the results for MDCK-II and MDCK-I cells were in line (Figure 55 C). As explained above (chapter 6.1.1), the values for the MDCK cell lines showed, that intact cell layers with the expression of microvilli and/or other convolutions of the plasma membrane have been formed. The differences found for A549 cells are most likely attributed to the extremely leaky barrier formed by these cells. The low contribution of the cell layer to the total impedance induces problems during the fitting procedure as the impedance of the cell layer is masked by the impedance of the bulk. For a more sensitive measurement of impedance spectra of A549 cells and other cells forming very leaky barrier, the active area of the filter support needs to be decreased in future measurements, providing a more robust basis for sensitive TER determination.

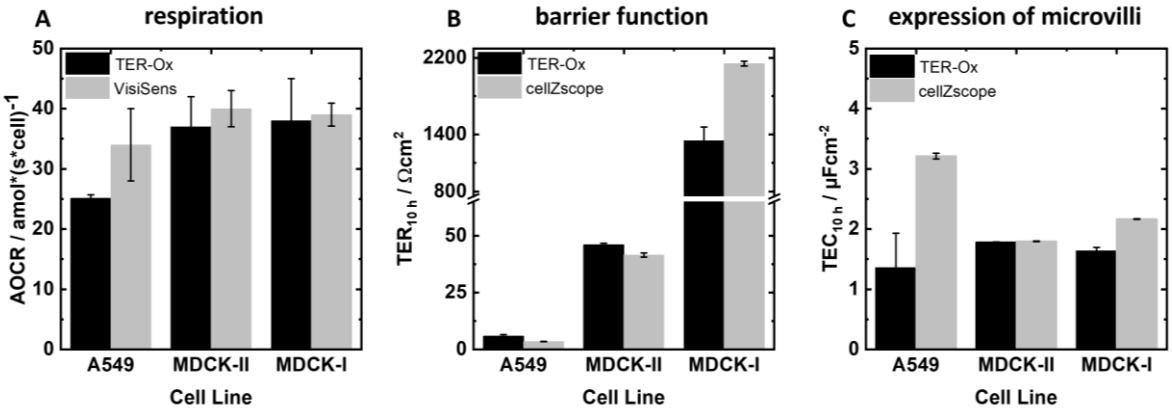

Figure 55: Comparison of results obtained in TER-Ox measurements to the established VisiSens TD (cellular respiration) and cellZscope® (barrier function) assays. (A*) Apparent oxygen consumption rates* determined by TER-Ox and VisiSens experiments. (B) TER values and (C) capacitance values after 10 h, resulting from TER-Ox and cellZscope® measurements. All results were obtained in a dry cell culture incubator at 37°C and 0 % CO_2 in three individual experiments (Mean ± SEM, n = 3).

6.2 Application of the TER-Ox platform

In order to portray potential applications of the TER-Ox platform three proof-of-principle experiments were performed. In a first experiment different drugs were added to cell layers cultured on permeable substrates. In a second experiment, TER-Ox was applied to monitor changes in cellular phenotype following epithelial-to-mesenchymal transition. and lastly, TER-Ox was used to monitor an indirect co-culture model of a monolayer cultured on a filter and a tumor spheroid. All three examples were performed to prove that a device based on the TER-Ox approach increases information depth and decreases experimental efforts to unravel cellular changes during disease progression as well as in drug development processes.

6.2.1 Monitoring of drug induced changes

In a first application example, MDCK-II cells were treated independently with two modulators of the oxidative phosphorylation and a barrier function modulator (Figure 56). Antimycin A is a blocker of complex III of the electron transport chain leading to a minimization of cellular respiration (Slater 1973). The TER-Ox results showed that MDCK-II cells stopped oxygen consumption immediately when treated with antimycin A (2 µM) as the time course of oxygen partial pressure did not show a decrease but an increase to levels of the maximum partial pressure of oxygen in the cell media at 37 °C (149.3 torr). Thus, AOCR cannot be calculated anymore and is set to 0 amol·(s·cell)$^{-1}$ (Figure 56 A). Antimycin A also showed strong influences on the barrier integrity. After addition, cells seemed to react to the treatment by a tightening of the cellular barrier leading to a strong increase of the TER. Additionally, cells seemed to partially lose their pre-established microvilli indicated by a decrease in cell layer capacitance with time. Subsequent to the initial reaction, antimycin initiates cell death, leading to a complete loss of the TER followed by a strong increase in the capacitance due to cell detachment. When cell layers get highly permeable, readings of the capacitance fail in all devices that rely on impedance analysis. Malonoben, an uncoupler of the oxidative phosphorylation, is reported to enhance cellular oxygen consumption to a maximum by short-circuiting the proton gradient which is established across the inner mitochondrial membrane by the ETC (Terada 1990). Accordingly, using TER-Ox a strong increase in the AOCR was detected, while neither epithelial barrier nor the membrane topography was affected after exposure to malonoben (10 nM). Cytochalasin D is a disruptor of actin filament polymerization while depolymerization is unaffected. Treatment of epithelial or endothelial cells with Cytochalasin D leads to a loss of cell-cell contacts as well as a reduction of microvilli on the apical surface (Schliwa 1982). Accordingly, using TER-Ox a decrease of TER values and TEC values of the MDCK-II cells with time after cytochalasin D (5 µM) addition was found. However, in comparison to

Antimycin A, cells did not detach from the surface of the filter inserts and the monolayer stayed intact as indicated by the rather stable values of the cell layer capacitance towards the end of the treatment. Moreover, the respiratory activity of MDCK-II cells was not affected by cytochalasin D addition.

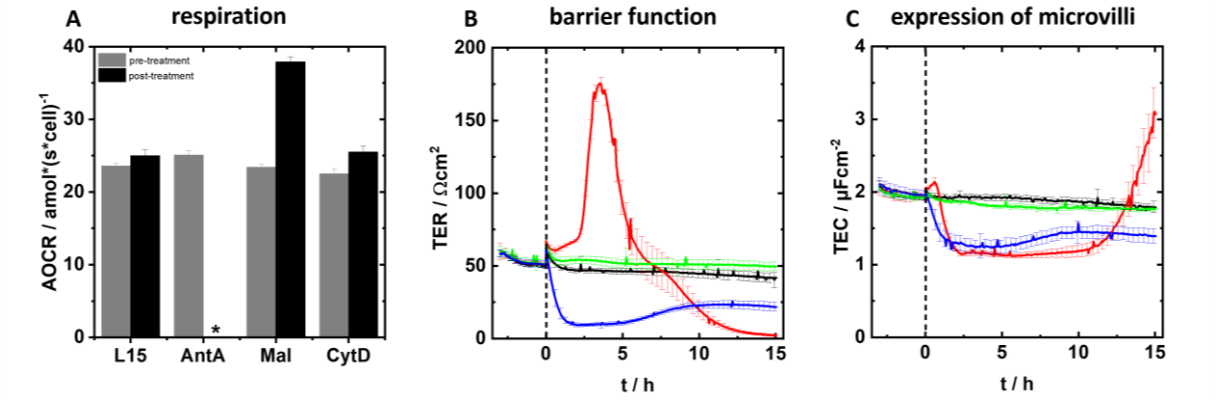

Figure 56: Treatment of confluent MDCK-II cell layers with OxPhos and barrier function modulators. Cells were treated with an L15 buffer control, antimycin A (2 µM), malonoben (10 nM), or cytochalasin D (5 µM), respectively. (A) Influence of antimycin A (AntA), malonoben (Mal), and cytochalasin D (CytD) on respiratory activity of MDCK-II cells as measured by the apparent oxygen consumption rate (AOCR). Time courses used to determine AOCR values can be found in in the supplementary information in chapter 11.1 in Figure S 11 (B), (C) Influence of L15 buffer control, antimycin A, malonoben, and cytochalasin D on barrier integrity and membrane topography of MDCK-II cells as reported by TER and TEC. The modulating compounds were added at t = 0 h (dashed line). All results were obtained using TER-Ox in three individual experiments in a dry cell culture incubator at 37°C and 0 % CO_2 (Mean ± SEM, n = 3).

6.2.2 Monitoring of epithelial-to-mesenchymal transition

Epithelial-to-mesenchymal transition (EMT) is an important driver in diseases such as cancer and many types of fibrosis. During EMT, epithelial cells change to a phenotype dominated by mesenchymal characteristics. In the process, amongst many other characteristics, the affected cells lose their ability to form proper barriers and undergo a reprogramming of cellular metabolism. In this work, TER-Ox was used to monitor three cell lines during different stages of EMT. The different cells were kindly provided by the group of Prof. Dr. Thomas Brabletz (University of Erlangen, Germany). The first cell line, KPC792, is a cell line with epithelial phenotype. Accordingly, TER was quantified using TER-Ox resulting in TER values around 15 Ωcm^2 for a mature cell layer, indicating a rather leaky barrier formed by these cells. TEC was quantified to values around 1 µFcm^{-2}, indicating the formation of an intact monolayer with some apical microvilli and/or basolateral membrane intrusions (Figure 57 B&C). KPC792 cells triggered to undergo EMT by TGF-ß treatment resulted in a second cell line with fully mesenchymal characteristics, KPC550. The loss of barrier function was correctly resolved by TER-Ox studies. While TER values were below 5 Ωcm^2, the transepithelial electrical capacitance resulted in a fluctuating time course. As already described above, impedance

analysis of cell layers with very low or no barrier function leads to non-reliable results for the transepithelial electrical capacitance. To gain more insight into the EMT mechanism, in a third cell line called KPCZ 346, the transcription factor Zeb1 was knocked down. Zeb 1 is an important transcription factor during EMT. It has been previously shown, that Zeb1 can initiate and/or promote EMT (Zhang et al. 2015) and therefore also cancer metastasis (Krebs et al. 2017). Additionally, Zeb1 is involved in mediating the formation and destruction of tight junctions. An upregulation of Zeb1 generally leads to a lower expression of tight junction proteins such as ZO-1 (wu et al. 2023). Using TER-Ox, high TER values above 800 Ωcm^2 were observed for the Zeb1 knockout line KPCZ 346 which is in line with the role of Zeb1 described above. The TEC was stable around 1.5 $\mu F cm^{-2}$ proving the presence of an intact monolayer during the measurement. The values are slightly higher than the TEC found for KPC792 cells indicating, that the formation of membrane invaginations and/or microvilli is enhanced in these cells. Both, tight barrier function and formation of membrane extrusions, are an indicator for epithelial cell types. These results were in line with expectations, as Zeb1 which promotes EMT is knocked down and therefore EMT cannot efficiently occur using this pathway.

Apart from barrier function, lower respiratory activity was found for the mesenchymal cells compared to the two epithelial cell lines (Figure 57 A). It is known that cells undergo metabolic reprogramming during EMT changing from an ATP production mainly based on oxidative phosphorylation towards an energy production strongly relying on glycolysis (Jiang et al. 2015; Takegahara et al. 2021). This lead to the observed changes in respiratory activity (Bhatia et al. 2021).

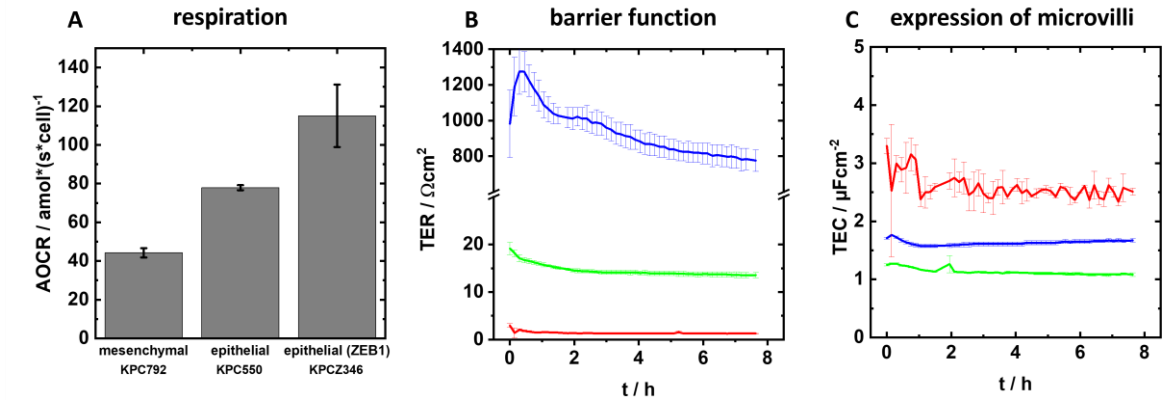

Figure 57: Monitoring of cells in different states of the epithelial to mesenchymal transition. (A) Oxygen consumption rate of the epithelial cell line KPC792, the ZEB1 Knockout cell line KPCZ346 and the mesenchymal cell line KPC550. (B) Barrier function of the cell lines KPC792 (green), KPCZ346 (blue), KPC550 (red) cultured on permeable substrates (Corning filter, d = 0.4 µm, $100 \cdot 10^6$ pores·cm^{-2}). (C) TEC monitored for the three different cell lines KPC792 (green), KPCZ346 (blue), KPC550 (red) cultured on permeable substrates. All experiments were performed in a standard cell culture incubator at 37 °C at 0 % CO_2 (n = 2, Mean ± SD).

6.2.3 Characterization of complex tissue models

In a last application example, we used TER-Ox to monitor a barrier forming cell layer of MDCK-II cells co-cultured on a filter hanging above a tumor spheroid of U373 cells cultured on the oxygen sensor foil. Therefore, the barrier forming cells were inoculated on the filter substrate as before. However, the gap between cell layer and oxygen sensor was enlarged by introducing a PVC spacer with a thickness of 1 cm on top of the stainless-steel block of the bottom chamber. The influence of the monolayer on the oxygen measurement was excluded due to the increased gap to the sensor. Instead of measuring the oxygen consumption of the cell layer, it was now possible to introduce a tumor spheroid placed directly on the sensor foil. Oxygen monitoring was then used to follow the development of the oxygen profile of the spheroid. After a baseline monitoring in L15 buffer, antimycin A was added to the apical compartment. As seen before for the monolayers, AntA had an influence on both, the cellular respiration of the spheroid and the barrier function of the MDCK-II cells (Figure 58). The results show that AntA penetrated the barrier formed by MDCK-II cells immediately which resulted in the fast increase of the partial oxygen pressure within the tumor spheroids. Additionally, antimycin A interfered with the barrier function in a similar way as described above in chapter 6.2.1. After AntA addition, the barrier seemed to tighten correlated to an increase of the TER. After reaching a maximum, the TER value decreased, reaching levels below baseline values, which indicates a loss in barrier function. At the same time, the *transepithelial electrical capacitance* decreased after AntA addition. The decrease can be attributed to the loss of microvilli and membrane extrusion. After maintaining a stable level for several hours, TEC started to increase sharply. Loss in barrier function and increase of capacitance suggest that the monolayer was destroyed and cells detached from the substrate.

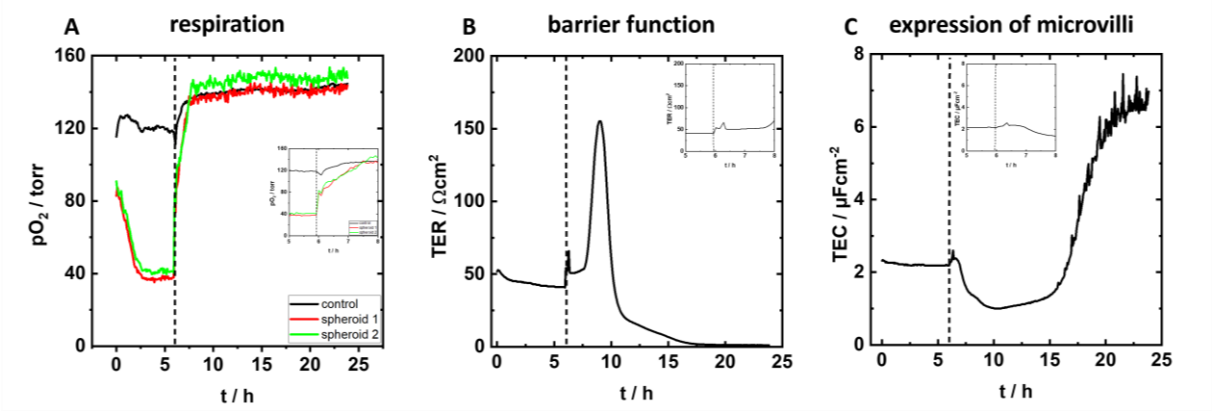

Figure 58: Monitoring of a complex co-culture model using TER-Ox. MDCK-II cells were cultured on the permeable substrates. Two tumor spheroids formed of U373 cells are cultured directly on the oxygen sensor foil underneath the MDCK-II cells on the filter insert. (A) Respiratory activity of the U373 spheroids cultured on the sensor foil surface (red, green) and oxygen time course of a cell-free sensor spot next to the spheroid (black). (B) TER time course of the MDCK-II cell layer cultured on the filter insert (Corning filter, d = 0.4 µm, $100 \cdot 10^6$ pores·cm^{-2}) representing the barrier function of the cell layer. (C) Time course of the TEC of the MDCK-II cell layer cultured on the permeable substrate. TEC indicates the formation of microvilli and/or other membrane intrusions. Small windows show a closer look on the development around the time of treatment. Experiment was performed in a dry incubator at 37 °C and 0 % CO_2.

6.3 Conclusion and Outlook

In this work an experimental platform capable of monitoring cellular respiration and barrier integrity of cell layers cultured on permeable substrates was successfully developed. Therefore, the two fundamental principles of ratiometric optical oxygen imaging and impedance spectroscopy were combined in a single setup. To the best of our knowledge, TER-Ox is the first device to allow for microphysiometric measurements on interfacial cell layers. The results suggest that the novel TER-Ox platform provided similar results as state-of-the-art methods used for individual and independent quantification of oxygen consumption (VisiSens TD) and epithelial barrier function (cellZscope®) as well as trends reported in literature. However, cells forming leaky barriers require particular attention during equivalent circuit modeling. To overcome this issue, the membrane area of the filter inserts can be reduced, leading to a significantly higher sensitivity of the impedance readout. In addition, we used the novel TER-Ox assay to monitor three different example applications. It was shown that TER-Ox can be used to determine drug-induced changes within a cell layer's barrier integrity and respiratory activity. Predicted influences of the OxPhos modulators antimycin A and malonoben as well as the cytoskeleton active cytochalasin D were reproduced by TER-Ox readings. In a second example phenotypes of cells representing different stages of epithelial-to-mesenchymal transition, a key driver of many pathological disorders, were determined. These examples demonstrate that the use of TER-Ox offers the possibility to resolve influences on the barrier function and respiratory activity of the identical cell population, leading to a more reliable, fact based, and multi-parametric interpretation of the observed biological response. Moreover, the simultaneous quantification of the three parameters TER, TEC and AOCR results in a reduction of assay time and cost. A third proof-of-principle application showed that TER-Ox is applicable to study several biological systems cultured together simultaneously. Instead of the biologically less relevant MDCK-II cell layer, blood brain barrier (BBB) models cultured above a tumor cell spheroid might be of interest. TER-Ox could then be used to determine changes on the barrier integrity of a cancer drug on the BBB as well as the cancer cells/tumor spheroid cultured underneath. This concept might also be transferred to other drug treatments limited by drug delivery across a strict biological barrier. The spatial resolution of the oxygen imaging might also offer the possibility to determine local changes in cellular respiratory activity within mixed 2D cell layers. Finally, the setup is adaptable to higher throughputs, which is particularly important to become attractive for drug screening campaigns. Overall, the results show that a device based on the TER-Ox approach is suitable for drug development processes as well as for

the use in assays targeting mechanisms in diseases altering cellular respiration and barrier integrity of cells.

7 CIS-TER: Impedance Spectroscopic monitoring of indirect co-cultures

The ability of drugs to cross epithelial or endothelial barriers is a crucial factor for drug targeting. Assessing this ability is therefore of great interest during drug discovery processes (Abbott 2013; Lee et al. 2023; Yang et al. 2017). This chapter focuses on the development of a platform capable of monitoring two cell layers cultured in proximity of each other. Combination of a barrier forming cell layer and a second cell layer representing diseased cells offers the possibility to study drug targeting and efficacy in a single setup. Thereby the first layer is directly cultured on a set of basolateral thin-film gold electrodes which are used to determine the cellular impedance of this layer (CIS-mode). The second cell layer is cultured on a permeable substrate hanging above the first layer. By introducing a dipping electrode to the apical compartment above the permeable substrate and combining it with the two electrodes in the basolateral compartment, the cellular impedance of the cell layer cultured on the filter substrate is determined (TER-mode). By using both modes in combination, the two indirectly co-cultured cell layers are monitored in parallel.

7.1 Development of electrode setups for impedance sensing of the basolateral cell layer

The first aim was to identify an electrode setup for monitoring cells in the basolateral compartment. Therefore, two different electrode layouts were compared. The first layout was a set of two interdigitated electrodes (IDE-setup) whereas the second layout consisted of a small circular working electrode and a large horseshoe counter electrode (WE/CE-setup, see chapter 3.2.4 Figure 7). The results for both electrode types are summarized in Figure 59. In general, the spectra shifted to a higher impedance range when using the WE/CE setup (Figure 59 B & D) compared to the IDE-setup (Figure 59 A & C). The impedance range of the spectra changed from 10^2 Ohm – 10^5 Ohm for the interdigitated electrodes to values between 10^3 Ohm – 10^7 Ohm for the WE/CE-setup. The range of the impedance values increased from approximately 3 decades for the IDE-setup to over 4 decades for the WE/CE-setup. The working electrode of the WE/CE-setup has the same area as the working electrode of the commercially available 8W1E ECIS® arrays. As shown in previous studies, impedance spectroscopy of these arrays without cells resulted in impedance spectra with similar characteristics. The spectra of both, the WE/CE-setup of CIS-TER and the 8W1E electrodes, ranged from 10^3 Ω at 100 kHz to $3 \cdot 10^5$ Ω at 100 Hz (Zinkl 2022). Technically, the CIS-TER device could not measure the high impedance values found in the low frequency range for the

WE/CE-setup, which led to a smaller frequency range for analysis and interpretation. The overall higher impedance values obtained for the WE/CE-setup are a consequence of the differences in the electrode areas of the two setups. The area of the working electrode of the WE/CE setup (0.049 mm^2), which determines the impedance values, is 500 times smaller than the area of the electrodes in the IDE-setup (0.25 cm^2). The smaller area restricts current flow and leads to an increase in impedance found for the cell free electrodes. The cell lines under study differ with respect to their barrier function. MDCK-I cells form very tight barriers, MDCK-II cells moderately tight barriers, whereas NRK cells form very leaky barriers. U373 cells are characterized by a mesenchymal cell shape and do not form a barrier. The formation of the tightest layers by MDCK-I cells was correctly resolved by measuring impedance spectra. The cellular influence in the mid frequency range was most pronounced for MDCK-I cells using both electrode setups. This is most obvious from the normalized impedance $Z_{norm} = |Z|/|Z_0|$ where the highest maximum was measured for MDCK-I cells in both cases with values of $Z_{norm} = 8.5 \pm 0.2$ and $Z_{norm} = 6.7 \pm 0.2$ for the IDE- and the WE/CE-setup, respectively. However, it was expected that the use of the WE/CE-setup would result in a higher sensitivity which would have resulted in a higher value of the normalized impedance. Taking a closer look at the impedance spectra, one can see that the cellular influence of the MDCK-I cells was strongly shifted to lower frequencies in comparison to the cell-free spectrum, which could explain the lower values in normalized impedance. The second cell line within this study, the MDCK-II cell line, is generally used as a model for cell layers forming barriers with intermediate tightness. This was again nicely depicted in the impedance spectra of both electrode setups, as the cellular influence of MDCK-II cells in the mid frequency range was less pronounced than the effect seen for MDCK-I cells but stronger than the effect observed for NRK cells and U373 cells. In the case of the spectra recorded using the IDE-setup this was also observed in the normalized impedance. The second highest value was found for MDCK-II cells ($Z_{norm} = 6.6 \pm 0.2$). Impedance monitoring of MDCK-II cells using the WE/CE-setup resulted in a maximum of the normalized impedance of $Z_{norm} = 3.75 \pm 0.08$. Again, this value was much smaller than the value found using the interdigitated electrodes. Similar to the findings of the MDCK-I cells, this might be explained by the shift of the cellular influence on the spectra. This effect even resulted in a less pronounced normalized impedance for MDCK-II cells in comparison to NRK cells. In comparison to MDCK-I and MDCK-II cells the sensitivity of the measurement strongly increased for NRK cells and U373 cells. The normalized impedance for NRK cells increased from $Z_{norm} = 3.1 \pm 0.1$ for interdigitated electrodes to $Z_{norm} = 4.75 \pm 0.08$ for the small electrode setup. The influence in the impedance spectra of U373 cells on interdigitated electrodes was hardly measurable and resulted in an extremely low normalized

impedance of Z_{norm} = 1.44 ± 0.04. Application of the U373 cells onto the WE/CE-setup resulted in a much stronger and better detectable change in impedance. The normalized impedance increased to Z_{norm} = 2.8 ± 0.2. The results suggested that it strongly depends on the application which electrode setup should be used. Future assays determining the impedance of cells characterized by the expression of barrier forming cell junctions, including epithelial or endothelial cell lines, are best performed using the IDE-setup. Cells not expressing these cell junctions on the other hand, such as fibroblasts or glioblastoma cells as used here, should be studied using the WE/CE-setup.

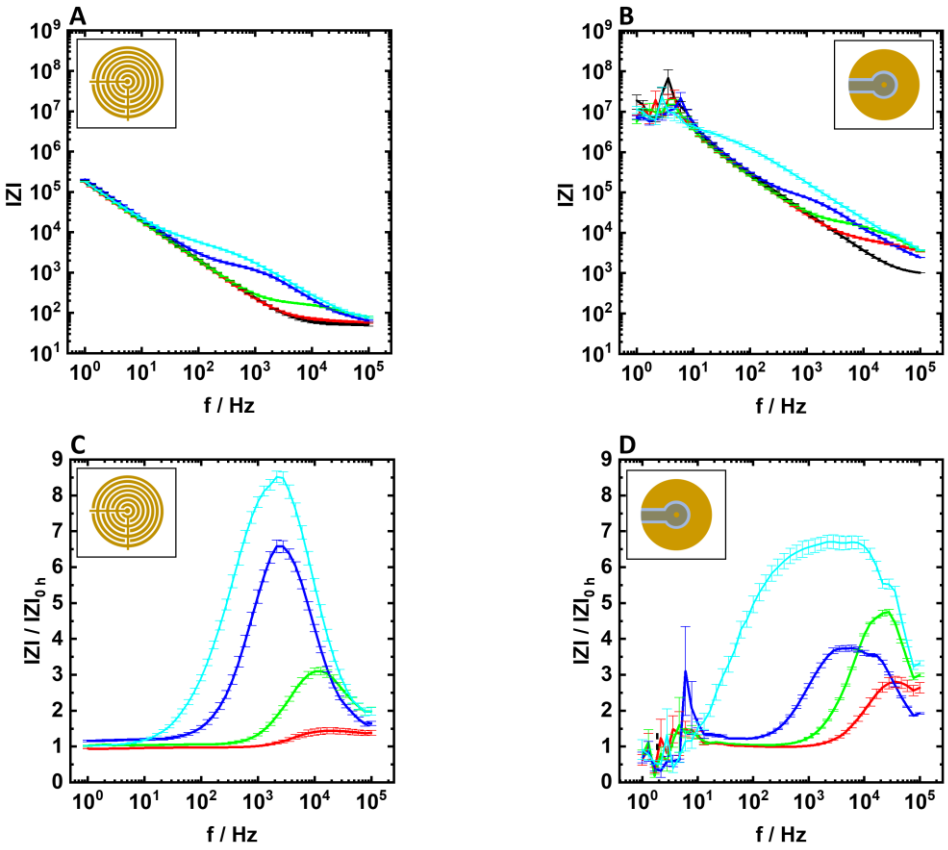

Figure 59: Comparison of two different layouts for the set of basolateral electrodes of the CIS-TER setup. Impedance spectra and normalized impedance spectra for the set of IDE-setup (A & C) as well as the WE/CE-setup (B &D) for **MDCK-I cells**, **MDCK-II cells**, **NRK-cells** and **U373 cells** cultured directly on the basolateral electrodes. Black curves are cell-free electrodes. Data were recorded using the CIS-mode of the CIS-TER setup in a standard cell culture incubator at 37 °C and 5 % CO_2 (Mean ± SEM, n = 3).

In addition to the cellular impedance discussed above, the spectra obtained with the two electrode setups revealed some unexpected features. Regardless of the electrode layout, the normalized impedance showed an increase for the highest frequency of f = 10^5 Hz. This effect might be parasitic effects of the cellZscope M hardware and requires further evaluation. In addition, the impedance spectra and the normalized impedance spectra showed a disturbance at frequencies above 10^4 Hz when using the WE/CE-setup. Theses disturbances may be a

consequence of the large area of the gold spot partially covered with photopolymer combined with an insufficiently thick photopolymer coating. According to the equation below, the capacitance is directly proportional to the electrode area and indirectly proportional to the photopolymer thickness:

$$C = \frac{\varepsilon_0 \varepsilon_r A}{d}$$

With C: capacitance, ε_0: dielectric constant of vacuum, ε_r: dielectric constant of gold, A: area of the electrode and d: thickness of the passivating photopolymer. In other words, the area of the circular gold structure covered by the photopolymer is too large and the thickness of the passivating layer to small. This results in an additional contribution to the impedance which can be seen in the spectra. To overcome these problems, the area of the gold spot could be reduced, and/or the photopolymer thickness increased. However, this reinforces the point made earlier: at the current stage of development, monitoring of cells that are characterized by the expression of barrier forming junctions are best analyzed using the interdigitated setup.

7.2 Histamine treatment of U373 cells cultured underneath barrier forming cell lines

The CIS-TER setup provides the ability to assess the state of two cell layers simultaneously. To portray this feature, three cell lines known to form differently tight cell layers were cultured on permeable substrates. Additionally, U373 cells were inoculated on the basolateral electrode setup. U373 cells cultured in the basolateral compartment endogenously express the H1-receptor and can therefore be stimulated by histamine (Hernández-Angeles et al. 2001). After 48 hours, the filters containing barrier forming cells were introduced into the setup above the layer of U373 cells and a baseline was measured for the TER of the cells cultured on the filters as well as the impedance of U373 cells growing on the basolateral electrodes. Afterwards, the cells were treated with histamine (200 µM) which was applied to the apical filter compartment. Depending on the tightness of the barrier, histamine diffuses at different rates through the barrier forming cell layers. However, histamine must first pass the cell layer cultured on the filter substrates before an interaction with the U373 cells can occur. The state of the barriers formed by the cell layers on the permeable substrates was determined using the TER mode. To activate this mode, the two basolateral electrodes were connected in parallel and used as a combined basolateral electrode against the apical dipping electrode as depicted in Figure 60 A. Figure 60 B and C show TER time courses after histamine treatment and after application of the control buffer L15, respectively. The TER results prior to treatment were in line with the trends reported in literature. MDCK-I cells are commonly used as model for tight barriers (Stevenson et al. 1988). This was observed using the CIS-TER setup with TER values around 2000 $\Omega \cdot cm^2$. MDCK-II cells are known to form moderately tight barriers resulting in TER values between 40 and 100 $\Omega \cdot cm^2$ (Dukes et al. 2011). The values measured using the novel CIS-TER setup were around 70 $\Omega \cdot cm^2$ which is in the range reported in literature. Lastly, we studied NRK cells which formed very leaky cell layers with TER-values around 10 $\Omega \cdot cm^2$. Values reported in literature for NRK cells are within the same range (Prozialeck et al. 2006). Addition of histamine did not lead to changes in the TER which were not also observed for cells cultured in L15 buffer. As cell lines cultured on the filters do not express the needed histamine receptor H1 a cellular reaction of these cells to histamine addition was not expected.

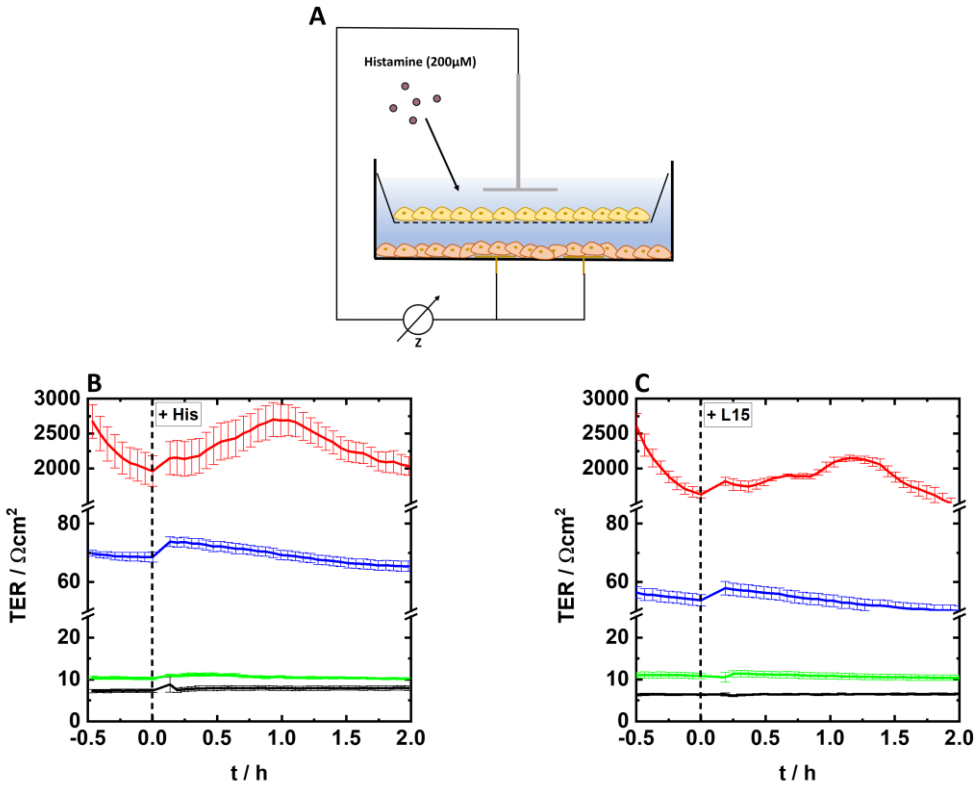

Figure 60: Evaluation of the effect of histamine treatment on barrier forming cells measured using the TER-mode of the CIS-TER setup. (A) Schematic illustration of the experiment and electrical connections in TER-mode. TER time course of **MDCK-I cells**, **MDCK-II cells**, **NRK cells** and **cell-free filters** treated with (B) histamine (200 µM) or (C) L15 buffer at t = 0 h. Histamine (His) and fresh buffer were added to the apical compartment of the filter. Data were recorded using the CIS-TER setup in a standard cell culture incubator at 37 °C and 0 % CO_2 (Mean ± SEM, n = 3).

Simultaneously, the CIS mode of the setup was used to examine the influence on the U373 cells cultured beneath the filter substrate on the basolateral electrodes. The distance between the two cell layers was approximately 1.4 mm. As depicted in Figure 61 A, in the CIS-mode two basolateral electrodes are measured against each other without using the apical dipping electrode. With regard to the results discussed in chapter 7.1, the experiment was conducted using the WE/CE setup, characterized by a better sensitivity for U373 cells. In addition, the impedance of the basolateral cell layer was monitored in single frequency / time mode (SFT mode) to obtain a better time resolution. A sensitive frequency was determined with the help of the normalized impedance spectrum shown in Figure 59 D. For the measurement a frequency of 21 kHz was chosen, as the sensitivity at this frequency was good and the frequency was below the influences on the measurement discussed above. Depending on the properties of the barrier formed by the cells on the porous substrates, histamine can now pass the cell layer from the apical to the basolateral compartment and trigger a stimulation of the U373 cells. Figure 61 B and C depict the results obtained after the application of histamine and pure L15 buffer, respectively. Application of histamine to the apical compartment of cell-free filters resulted in

an immediate increase within the first 30 mins after addition of the normalized impedance of the U373 cell layer. The same observation was made for NRK cells which formed a very leaky barrier according to the TER values shown above. Previous studies by Lieb et al. revealed similar changes upon histamine addition to U373 cells using ECIS (Lieb et al. 2016). Lieb et al. observed an increase in the impedance between 800 Ω and 1000 Ω within 30 mins after histamine addition. Considering, that the volume within the filter used in the CIS-TER approach was 200 µL and the total volume of a well of the CIS-TER setup was 1.1 mL, the histamine concentration added during the CIS-TER assay reduced from 200 µM to approximately 40 µM due to the diffusion into the basolateral compartment. This concentration is in a similar range used by Lieb et al. (30 µM). The increase in normalized impedance observed in the CIS-TER setup from 1.0 (appr. 5000 Ω) to 1.2 translates to a difference in impedance of approximately 1000 Ω which is similar to the values reported by Lieb et al. The normalized impedance of U373 cells cultured underneath filters with MDCK-II and MDCK-I cells did not increase but stayed stable after histamine addition. At the same time, the addition of L15 to the apical compartment did not trigger any significant changes in $Z_{norm.}$ regardless of the cell type. This suggests that in the case of the cell-free filters and the filters covered by a very leaky NRK cell layer, histamine was able to pass from the apical to the basolateral compartment triggering GPCR stimulation and a subsequent morphological change of the U373 cells cultured in these compartments. MDCK-II and MDCK-I cells which formed stronger barriers compared to the NRK cells, inhibited the diffusion of histamine towards the basolateral compartment which was indicated by the absence of any morphological changes of the U373 cells cultured underneath.

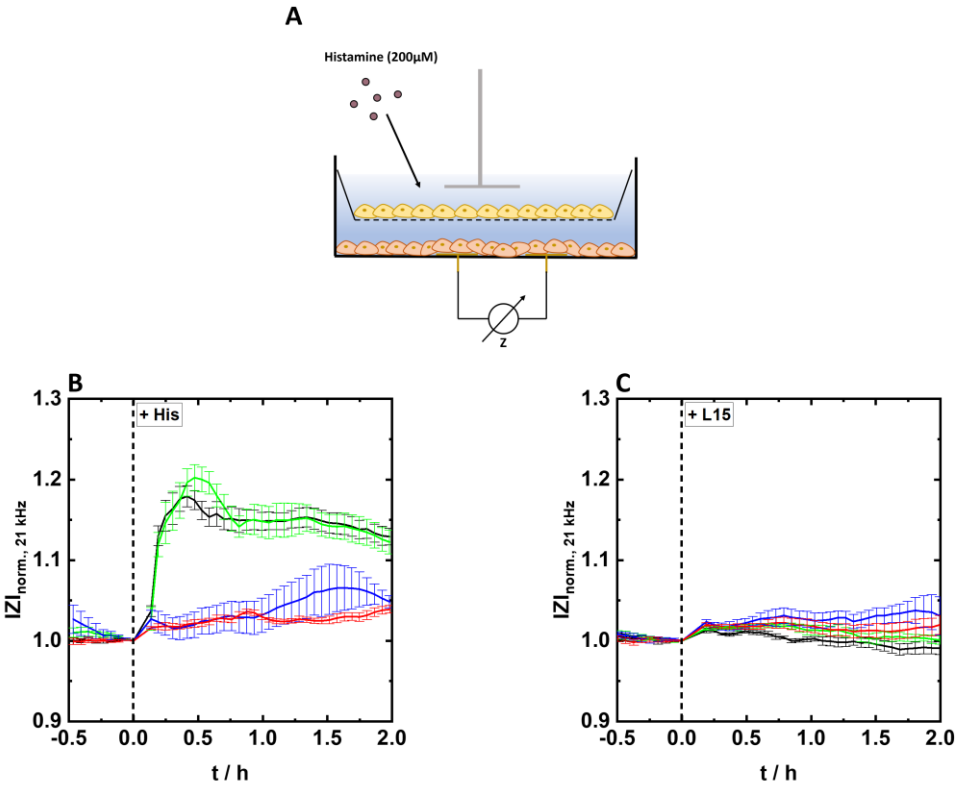

Figure 61: Evaluation of the effect of histamine treatment on U373 cells measured using the CIS-mode of the CIS-TER setup. (A) Schematic illustration of the experiment and electrical connections in CIS-mode. Z_{norm} time course of U373 cells cultured underneath filter substrates with **MDCK-I cells**, **MDCK-II cells**, **NRK cells** and **cell-free filters** treated with (A) histamine (200 µM) or (B) L15 at t = 0 h. Histamine (His) and L15 were added to the apical compartment of the filter. Data were recorded using the CIS-TER setup in a standard cell culture incubator at 37 °C and 0 % CO_2 (Mean ± SEM, n = 3).

To confirm that the increase in normalized impedance of U373 cells cultured underneath cell free filters and filters cultured with NRK cells resulted from a specific activation of the H1 receptor, a second experiment in which U373 cells were pre-treated with mepyramine (5 µM) prior to histamine addition was performed. Mepyramine is an antagonist of the histamine H^1-receptor (Hishinuma and Young 1995). The results are depicted in Figure 62. Mepyramine addition did not result in any changes of the normalized impedance of U373 cells as well as the TER of NRK cells. After attaining renewed equilibrium values, histamine (200 µM) was added to the apical compartment. Similar to before, the addition of histamine did not result in changes of the TER of the NRK cells. However, in comparison to the results described above, the normalized impedance of the U373 cells did not increase for both conditions but stayed stable at baseline levels until the end of the measurement. The addition of mepyramine prevented the histamine from binding to the H^1-receptor and the morphological changes observed before were not triggered. Combined with the previously presented results, this validated the theory described in the beginning of this chapter: Depending on the tightness of the barrier formed by the cells cultured in the apical compartment, histamine can diffuse to the basolateral

compartment and trigger a morphological change of U373 cells cultured on the basolateral set of electrodes.

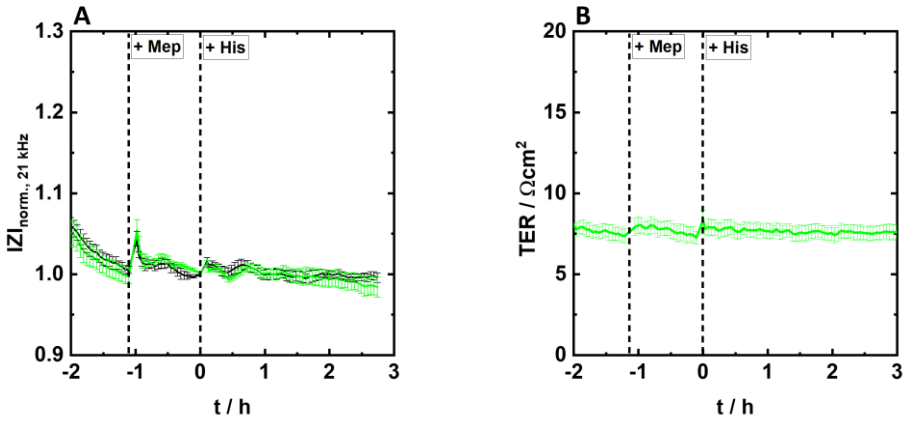

Figure 62: Evaluation of the effect of histamine treatment on U373 cells after mepyramine treatment measured using the CIS-TER setup. (A) Z_{norm} time course of U373 cells cultured underneath filter substrates with **NRK cells** and **cell-free filters**. (B) TER time course of NRK cells cultured on permeable substrates (SFtl0.4). U373 cells were treated with mepyramine (Mep, 5 µM) at the first dashed line. At t = 0 h (second dashed line) histamine (200 µM) was added to the apical compartment of the filter. Data were recorded using the CIS-TER setup in a standard cell culture incubator at 37 °C and 0 % CO_2 (Mean ± SEM, n = 3).

7.3 Conclusion & Outlook

A setup, called CIS-TER, for the simultaneous monitoring of the impedance of two indirectly co-cultured cell layers was developed. A set of three electrodes enabled the characterization of two cell layers within the same well: a cell layer cultured on a set of basolateral thin-film gold electrodes and a second cell layer cultured on a permeable substrate. The second cell layer was placed above the first layer. The setup can be used in a medium-high throughput, measuring 24 combined layers at the same time. In addition, the basolateral electrodes can either be used in a multi-frequency mode allowing the determination of impedance spectra as well as a single frequency mode, with higher time resolution. Impedance characteristics for different layouts of the basolateral electrodes were determined for 4 different cell lines, MDCK-I cells, MDCK-II cells, NRK cells and U373 cells. The cell lines are differently characterized with regard to their barrier strength. The use of interdigitated electrodes was specifically sensitive for cell lines characterized by a strong impedance signal, such as epithelial or endothelial cells. For the characterization of cells lines with small influences on the impedance signal it was beneficial to use a small working electrode in combination with a larger horseshoe counter electrode. Furthermore, the functionality of the novel assay was demonstrated by determining the influence of histamine on U373 cells cultured together with different barrier forming cells. Therefore, NRK, MDCK-II and MDCK-I cells were cultured on filter substrates and histamine was added to the apical compartment of these filters. Using the TER-mode of the setup, it was

possible to monitor the barrier strength of these cells and the changes due to histamine addition. The CIS-mode was applied simultaneously to determine the changes in cell morphology of the U373 cells due to the diffusion of histamine from the apical part of the setup into the basolateral chamber. Thereby, the influence of histamine on the basolateral cell layer was dependent on the barrier strength of the apical layer. The experiments showed that the CIS-TER setup is suitable to monitor a wide range of different cell types in the TER and in the CIS mode. The two different designs of the basolateral electrode arrangement, offer the possibility to determine holistic changes in a cell monolayer (IDE setup) as well as cells with very weak influences on impedance signals such as fibroblasts (WE/CE setup). The novel CIS-TER mode enables the simultaneous analysis of an indirect co-culture of two monolayers. Analysis based on the suggested setup could strongly contribute to the investigation of drug delivery across cellular barriers, an important factor for drug efficacy.

Future experiments might aim to further develop the setup of the basolateral electrodes to eliminate the parasitic effects obtained in the high frequency range. Apart from necessary improvements to the setup, further experiments demonstrating the biological relevance of the CIS-TER assay will be performed. In the first step, a histamine experiment can be performed in a concentration dependent manner. Furthermore, other examples with clear biological relevance will be conducted. Therefore, first experiments were started to combine blood-brain barrier models with metastatic cancer cells which could be a model to help determine novel drugs targeting brain metastasis. Previous studies in our laboratory focused on the analysis of a co-culture of two cell layers grown on both sides of the filter membrane using impedance spectroscopy (Hajek and Wegener 2017). Combining this approach and the here developed CIS-TER assay would enable the simultaneous analysis of three indirectly co-cultured cell layers. This would enable the study of more complex models of the blood-brain barrier, containing endothelial cells on the apical side of the filter, astrocytes and pericytes on the basolateral side of the membrane and finally neurons cultured directly on the basolateral electrode setup (Storck and Pietrzik 2018).

8 Summary

Advanced cellular models will play a key role in future drug development processes and fundamental disease research. Apart from further improvements of the advanced and more complex tissue models, it is necessary to provide assay platforms capable of monitoring these models without the use of labels or the need for invasiveness, allowing for repeated and time-resolved observation. This work introduces several approaches which may pave the way for a better understanding and characterization of advanced cell culture options. Therefore, the scope of imaging microphysiometry as well as the measurement of cellular impedance was expanded by several new assay platforms and entirely new concepts.

The focus of this work was the development of a microphysiometric assay platform to determine the metabolic phenotype of tumor spheroids. A platform technology was designed enabling the subsequent monitoring of oxygen consumption and extracellular acidification by ratiometric optical oxygen and pH imaging of the same spheroid. Therefore, the applicability of imaging microphysiometry was expanded to tumor spheroids cultured on permeable substrates. The permeable substrates enabled the transfer of the spheroids between different sensor surfaces and subsequent analysis of the spheroid's oxygen consumption and extracellular acidification. Aerobic, anaerobic and metabolic profiles of spheroids were introduced to enable a more integral and comprehensive data interpretation. Furthermore, the novel approach is suitable to determine drug induced changes in the samples, as demonstrated by monitoring the influence of oxidative phosphorylation modulators (antimycin A and malonoben) on the metabolic phenotype. Future research focusing on higher throughputs and the analysis of pharmaceuticals will enhance the applicability of the novel platform for drug development processes.

Additionally, imaging microphysiometry was implemented as a tool to determine the oxygen distribution within:

a) stem cell derived brain organoids and brain organoids co-cultured with metastatic cancer cells and

b) precision-cut lung slices.

Metabolic profiling of organoids and precision cut tissue slices is still in its infancy but is considered as a new analytical micro technique with significant potential.

In a second approach, imaging microphysiometry was combined with impedance spectroscopy to enable simultaneous monitoring of epithelial barrier function (TER) and respiratory activity

(Ox). A novel measurement chamber was designed for this assay (TER-Ox) and monitoring of three different cell lines resulted in similar values compared to the established devices, cellZscope® and VisiSens TD, for transepithelial electrical resistance, transepithelial electrical capacitance as well es *apparent oxygen consumption rates*. Several applications of the TER-Ox platform were demonstrated in this thesis. This work depicted the suitability of TER-Ox to determine drug induced changes on cellular respiration and barrier function. Furthermore, TER-Ox was used to determine the different phenotypes of cells in different stages of the epithelial-to-mesenchymal transition. Finally, the use of TER-Ox to monitor a tumor spheroid and a barrier forming cell line grown in indirect co-culture was implemented. This approach enables the study of drug delivery into solid tumor entities across biological barriers such as the blood brain barrier. Summarizing, a platform based on the novel TER-Ox assay lays the foundation of a more in detail label-free analysis during drug discovery processes and the unraveling of disease progression. Future development on TER-Ox will mainly focus on achieving higher throughput.

In the final project, two fundamental approaches of impedance spectroscopy were combined to monitor two monolayers cultured in indirect co-culture (CIS-TER assay). The upper cell layer was cultured on a permeable substrate and characterized via TER and TEC readings, whereas the bottom layer was cultured underneath the first layer directly on an array of basolateral thin-film gold electrodes. The specialized electrode design of the novel CIS-TER device allowed simultaneous monitoring of both cell layers. A proof-of-principle experiment portrayed the functionality of the suggested assay. The assay platform offers a medium to high throughput, monitoring up to 24 culture models simultaneously. Moreover, the assay is fully integrable into the cellZscope M device commercialized by nanoAnalytics GmbH. Expanding the use of this assay to more biological relevant problems will be the focus of future research.

The platforms depicted in this thesis demonstrate that the use of imaging microphysiometry combined with impedance analysis is an effective tool for characterizing advanced tissue and disease models. The suggested platforms improve the applicability of advanced tissue models by offering label-free, non-invasive and time-resolved characterization of complex biological *in-vitro* models. Approaches as presented here will contribute to a deeper understanding, a higher feasibility and a better applicability of advanced disease models in drug development processes.

9 Zusammenfassung

Die Anwendung fortgeschrittener *in-vitro* Modelle wird in Zukunft bei der Arzneimittelentwicklung als auch bei der Erforschung grundlegender Krankheiten weiter zunehmend an Bedeutung gewinnen. Neben der Entwicklung fortschrittlicher und komplexer Gewebemodelle ist es notwendig, Assay-Plattformen und analytische Technologien bereitzustellen, die in der Lage sind, diese Modelle zu charakterisieren, ohne die Verwendung von chemischen Labeln oder der Notwendigkeit von Invasivität. In dieser Arbeit wurden mehrere bioanalytische Ansätze entwickelt, die zu einer besseren Charakterisierung fortgeschrittener Zellkulturmodelle beitragen. Dazu wurde der Anwendungsbereich der ratiometrischen optischen Bildgebung von pH und Sauerstoff sowie der Messung der Zellimpedanz durch mehrere neue Assay Plattformen sowie Konzepte erweitert.

Zunächst wurde eine Plattform dargestellt, die es ermöglicht den metabolischen Phänotyp von zellulären Monolayern und Tumor-Sphäroiden zu bestimmen. Dafür wurde ein Workflow erarbeitet, der es erlaubt, den Sauerstoffverbrauch und die Ansäuerung des extrazellulären Raumes durch bildgebende Microphysiometrie desselben Zellmodells zu analysieren. Dazu wurde das Konzept des ratiometrischen Sauerstoff und pH Monitorings auf Zellschichten und Sphäroide, welche auf permeablen Substraten kultiviert wurden, erweitert. Die Kultivierung auf permeablen Substraten ermöglicht dabei den Transfer der Gewebemodelle zwischen verschiedenen Sensoren. Um eine einfachere und intuitivere Interpretation der Daten zu ermöglichen, wurde das „aerobische Profil“ und das „anaerobische Profil“ eingeführt. Diese ermöglichen die Analyse von räumlicher und zeitlicher Datenlage auf einen Blick. Darüber hinaus wurde gezeigt, dass der neue Ansatz zur Untersuchung von substanzinduzierter Veränderung der Zellmodelle verwendet werden kann, indem der Einfluss von Modulatoren der oxidativen Phosphorylierung, Antimycin A und Malonoben, auf den metabolischen Phänotyp untersucht wurde. Neben der Sphäroid Analyse, wurde der mikrophysiometrische Ansatz als Instrument zur Bestimmung der Sauerstoffverteilung in Organoiden aus humanen, induzierten, pluripotenten Stammzellen sowie in Präzisions-Gewebeschnitten eingeführt. In zukünftigen Experimenten soll der Durchsatz der Assay-Plattform verbessert werden. Die Messungen an Organoiden und PCLS sollen auf Basis der hier dargestellten Ansätze weiterentwickelt werden. Außerdem liefert die entwickelte Assay Plattform die Möglichkeit die Wirkprofile von klinisch eingesetzten Substanzen genauer zu charakterisieren.

In einem weiteren Ansatz wurde das Konzept der bildgebenden Mikrophysiometrie mit der Impedanzspektroskopie kombiniert, um eine gleichzeitige Charakterisierung der epithelialen

Barrierefunktion (TER) und Atmungsaktivität (Ox) zu ermöglichen. Die Verwendung der neu entwickelten TER-Ox Kammer ergab im Vergleich zu den einzelnen Ansätzen, cellZscope® und VisiSens TD, ähnliche Werte für den transepithelialen elektrischen Widerstand, die Zellschichtkapazität sowie die Sauerstoffverbrauchsraten von drei verschiedenen Zelllinien. Mehrere Anwendungen der TER-Ox Plattform wurden demonstriert. TER-Ox ermöglicht es substanz-induzierte Veränderungen der Zellatmung und der Barrierefunktion zu bestimmen. Darüber hinaus wurde TER-Ox verwendet, um Phänotypen von Zellen in verschiedenen Stadien der epithelial-mesenchymalen Transition zu bestimmen. Zum Abschluss konnte TER-Ox genutzt werden, um eine indirekte Co-Kultur aus einem Tumor-Sphäroid und einer barriere-bildenden Zelllinie zu untersuchen. Dieses Assay ermöglicht es den Übergang von Medikamenten über zelluläre Barrieren und die anschließende Wirkung auf Tumore zu untersuchen. Abschließend lässt sich sagen, dass eine Plattform, die auf der Verwendung von TER-Ox basiert, einen wichtigen Beitrag zur Entdeckung von Medikamenten und zur Entschlüsselung von Krankheitsverläufen leisten kann. Die künftige Entwicklung von TER-Ox wird sich hauptsächlich auf die Erzielung höherer Durchsätze konzentrieren.

In einem abschließenden Projekt wurden zwei grundlegenden Ansätze der Impedanzspektroskopie kombiniert, um zwei indirekt ko-kultuvierte zelluläre Monoschichten gleichzeitig zu überwachen. Die obere Zellschicht wurde auf einem permeablen Substrat kultiviert und durch TER- und TEC-Messungen charakterisiert, während die zweite Schicht unterhalb der ersten Schicht direkt auf dem basolateralen Elektrodenaufbau kultiviert wurde. Das spezielle Elektrodenlayout des CIS-TER-Aufbaus ermöglicht es die Parameter beider Zellschichten gleichzeitig zu überwachen. In einem Proof-of-Principle-Experiment wurde die Funktionalität des vorgeschlagenen Assays dargestellt. Der entwickelte Ansatz liefert schon jetzt einen mittelhohen Durchsatz, mit der Möglichkeit 24 Co-Kulturmodelle simultan zu analysieren. Darüber hinaus ist der Assay vollständig in das von nanoAnalytics GmbH vertriebene cellZscope M Gerät integrierbar. Die Ausweitung der Anwendung dieses Assays auf weitere biologisch relevante Fragestellungen wird der Schwerpunkt zukünftiger Forschung sein.

Zusammenfassend zeigen die dargestellten Technologien, dass die Verwendung von mikrophysiometrischen Ansätzen und Impedanz-Analyse einen wichtigen Beitrag zur Charakterisierung komplexer Gewebe- und Krankheitsmodelle leisten kann. Der Einsatz dieser Plattformen verbessert den Nutzen komplexerer Zellmodelle, da sie eine markierungsfreie und nicht-invasive Charakterisierung mit guter zeitlicher Auflösung bieten. Dies kann zu einem

tieferen Verständnis, einer verbesserten Genauigkeit und somit einer besseren Prädiktivität von fortgeschrittenen Krankheitsmodellen in der Arzneimittelentwicklung führen.

10 Publication Bibliography

Abbott, N. Joan (2013): Blood-brain barrier structure and function and the challenges for CNS drug delivery. In *Journal of inherited metabolic disease* 36 (3), pp. 437–449. DOI: 10.1007/s10545-013-9608-0.

Acker, H.; Carlsson, J.; Holtermann, G.; Nederman, T.; Nylén, T. (1987a): Influence of glucose and buffer capacity in the culture medium on growth and pH in spheroids of human thyroid carcinoma and human glioma origin. In *Cancer Research* 47 (13), pp. 3504–3508.

Acker, H.; Carlsson, J.; Holtermann, G.; Nederman, T.; Nylén, T. (1987b): Influence of Glucose and Buffer Capacity in the Culture Medium on Growth and pH in Spheroids of Human Thyroid Carcinoma and Human Glioma Origin1. In *Cancer Research* 47 (13), pp. 3504–3508.

Agilent Technologies (2016): Identifying Metabolic Phenotype Switches in Cancer Cells Using the Agilent Seahorse XF Analyzer in an Hypoxic Environment Application.

Ahn, Jinchul; Ohk, Kyungeun; Won, Jihee; Choi, Dong-Hee; Jung, Yong Hun; Yang, Ji Hun et al. (2023): Modeling of three-dimensional innervated epidermal like-layer in a microfluidic chip-based coculture system. In *Nature communications* 14 (1), p. 1488. DOI: 10.1038/s41467-023-37187-4.

Alexander, Frank; Eggert, Sebastian; Price, Dorielle (2019): Label-Free Monitoring of 3D Tissue Models via Electrical Impedance Spectroscopy. In Joachim Wegener (Ed.): Label-Free Monitoring of Cells in vitro, vol. 2. Cham: Springer International Publishing (Bioanalytical Reviews), pp. 111–134.

Andrews, Madeline G.; Kriegstein, Arnold R. (2022): Challenges of Organoid Research. In *Annual review of neuroscience* 45, pp. 23–39. DOI: 10.1146/annurev-neuro-111020-090812.

Bhatia, Sugandha; Thompson, Erik W.; Gunter, Jennifer H. (2021): Studying the Metabolism of Epithelial-Mesenchymal Plasticity Using the Seahorse XFe96 Extracellular Flux Analyzer. In *Methods in molecular biology (Clifton, N.J.)* 2179, pp. 327–340. DOI: 10.1007/978-1-0716-0779-4_25.

Birey, Fikri; Andersen, Jimena; Makinson, Christopher D.; Islam, Saiful; Wei, Wu; Huber, Nina et al. (2017): Assembly of functionally integrated human forebrain spheroids. In *Nature* 545 (7652), pp. 54–59. DOI: 10.1038/nature22330.

Bogdanowicz, Danielle R.; Lu, Helen H. (2013): Studying cell-cell communication in co-culture. In *Biotechnology journal* 8 (4), pp. 395–396. DOI: 10.1002/biot.201300054.

Cacciamali, Andrea; Villa, Riccardo; Dotti, Silvia (2022): 3D Cell Cultures: Evolution of an Ancient Tool for New Applications. In *Frontiers in physiology* 13, p. 836480. DOI: 10.3389/fphys.2022.836480.

Chae, SooJung; Hong, Jiyoung; Hwangbo, Hanjun; Kim, GeunHyung (2021): The utility of biomedical scaffolds laden with spheroids in various tissue engineering applications. In *Theranostics* 11 (14), pp. 6818–6832. DOI: 10.7150/thno.58421.

Charlet-Faure, Claire; Thulesen, Annemette Præstegaard; Rogowska-Wrzesinska, Adelina (2023): Advancements in 3D spheroid imaging: Optimised cryosectioning and immunostaining techniques. In *MethodsX* 11, p. 102415. DOI: 10.1016/j.mex.2023.102415.

Childress, Elizabeth S.; Alexopoulos, Stephanie J.; Hoehn, Kyle L.; Santos, Webster L. (2018): Small Molecule Mitochondrial Uncouplers and Their Therapeutic Potential. In *Journal of medicinal chemistry* 61 (11), pp. 4641–4655. DOI: 10.1021/acs.jmedchem.7b01182.

Chmayssem, Ayman; Tanase, Constantin Edi; Verplanck, Nicolas; Gougis, Maxime; Mourier, Véronique; Zebda, Abdelkader et al. (2022): New Microfluidic System for Electrochemical Impedance Spectroscopy Assessment of Cell Culture Performance: Design and Development of New Electrode Material. In *Biosensors* 12 (7). DOI: 10.3390/bios12070452.

Choudhury, Subholakshmi; Das, Amitava (2021): Advances in generation of three-dimensional skin equivalents: pre-clinical studies to clinical therapies. In *Cytotherapy* 23 (1), pp. 1–9. DOI: 10.1016/j.jcyt.2020.10.001.

Chung, Henry H.; Mireles, Marcela; Kwarta, Bradley J.; Gaborski, Thomas R. (2018): Use of porous membranes in tissue barrier and co-culture models. In *Lab on a chip* 18 (12), pp. 1671–1689. DOI: 10.1039/c7lc01248a.

Costa, Elisabete C.; Silva, Daniel N.; Moreira, André F.; Correia, Ilídio J. (2019): Optical clearing methods: An overview of the techniques used for the imaging of 3D spheroids. In *Biotechnology and bioengineering* 116 (10), pp. 2742–2763. DOI: 10.1002/bit.27105.

Davies, Emma J.; Dong, Meng; Gutekunst, Matthias; Närhi, Katja; van Zoggel, Hanneke J. A. A.; Blom, Sami et al. (2015): Capturing complex tumour biology in vitro: histological and molecular characterisation of precision cut slices. In *Scientific reports* 5, p. 17187. DOI: 10.1038/srep17187.

Dings, J.; Meixensberger, J.; Jäger, A.; Roosen, K. (1998): Clinical experience with 118 brain tissue oxygen partial pressure catheter probes. In *Neurosurgery* 43 (5), pp. 1082–1095. DOI: 10.1097/00006123-199811000-00045.

Dirheimer, Luca; Pons, Thomas; Marchal, Frédéric; Bezdetnaya, Lina (2022): Quantum Dots Mediated Imaging and Phototherapy in Cancer Spheroid Models: State of the Art and Perspectives. In *Pharmaceutics* 14 (10). DOI: 10.3390/pharmaceutics14102136.

Dukes, Joseph D.; Whitley, Paul; Chalmers, Andrew D. (2011): The MDCK variety pack: choosing the right strain. In *BMC cell biology* 12, p. 43. DOI: 10.1186/1471-2121-12-43.

Duval, Kayla; Grover, Hannah; Han, Li-Hsin; Mou, Yongchao; Pegoraro, Adrian F.; Fredberg, Jeffery; Chen, Zi (2017): Modeling Physiological Events in 2D vs. 3D Cell Culture. In *Physiology (Bethesda, Md.)* 32 (4), pp. 266–277. DOI: 10.1152/physiol.00036.2016.

Fellenz, M. P.; Gerweck, L. E. (1988): Influence of extracellular pH on intracellular pH and cell energy status: relationship to hyperthermic sensitivity. In *Radiation research* 116 (2), pp. 305–312.

Fogh, J.; Fogh, J. M.; Orfeo, T. (1977): One hundred and twenty-seven cultured human tumor cell lines producing tumors in nude mice. In *Journal of the National Cancer Institute* 59 (1), pp. 221–226. DOI: 10.1093/jnci/59.1.221.

Forcione, Mario; Ganau, Mario; Prisco, Lara; Chiarelli, Antonio Maria; Bellelli, Andrea; Belli, Antonio; Davies, David James (2021): Mismatch between Tissue Partial Oxygen Pressure and Near-Infrared Spectroscopy Neuromonitoring of Tissue Respiration in Acute Brain Trauma: The Rationale for Implementing a Multimodal Monitoring Strategy. In *International journal of molecular sciences* 22 (3). DOI: 10.3390/ijms22031122.

Frandsen, Helle Sedighi; Štampar, Martina; Vej-Nielsen, Joel Mario; Žegura, Bojana; Rogowska-Wrzesinska, Adelina (2021): Method to Disassemble Spheroids into Core and Rim for Downstream Applications Such as Flow Cytometry, Comet Assay, Transcriptomics, Proteomics, and Lipidomics. In *Methods in molecular biology (Clifton, N.J.)* 2273, pp. 173–188. DOI: 10.1007/978-1-0716-1246-0_12.

Frank, Linda (2023): In silico Analyse der Sauerstoffverteilung in Zellen und Geweben mittels der Finiten-Elemente-Methode. Disseration. Universität Regensburg, Regensburg. Insitiut für Analytische Chemie, Chemo- und Biosensorik.

Garcia-Garcia, F. C.; Candarlioglu, P. L.; Porter, J. D.; Davies, D. E.; Swindle, E. J.; Morgan, H. (2022): Microfluidic technologies for ex vivo tissue biopsies: A review. In *Organs-on-a-Chip* 4, p. 100020. DOI: 10.1016/j.ooc.2022.100020.

Gaush, C. R.; Hard, W. L.; Smith, T. F. (1966): Characterization of an established line of canine kidney cells (MDCK). In *Proceedings of the Society for Experimental Biology and Medicine.*

Society for Experimental Biology and Medicine (New York, N.Y.) 122 (3), pp. 931–935. DOI: 10.3181/00379727-122-31293.

Gentet, L. J.; Stuart, G. J.; Clements, J. D. (2000): Direct measurement of specific membrane capacitance in neurons. In *Biophysical journal* 79 (1), pp. 314–320. DOI: 10.1016/S0006-3495(00)76293-X.

Giard, D. J.; Aaronson, S. A.; Todaro, G. J.; Arnstein, P.; Kersey, J. H.; Dosik, H.; Parks, W. P. (1973): In vitro cultivation of human tumors: establishment of cell lines derived from a series of solid tumors. In *Journal of the National Cancer Institute* 51 (5), pp. 1417–1423. DOI: 10.1093/jnci/51.5.1417.

Gorlach, A.; Bolling, B.; Holtermann, G.; Schwachofer, J.; Carlsson, J.; Acker, H. (1995): Changes in growth, po(2) and ph after exposure to oxamate - studies of 2 human tumor-cell lines growing as multicellular spheroids. In *International journal of oncology* 7 (4), pp. 831–839. DOI: 10.3892/ijo.7.4.831.

Goubko, Catherine A.; Cao, Xudong (2009): Patterning multiple cell types in co-cultures: A review. In *Materials Science and Engineering: C* 29 (6), pp. 1855–1868. DOI: 10.1016/j.msec.2009.02.016.

Graaf, Inge A. M. de; Olinga, Peter; Jager, Marina H. de; Merema, Marjolijn T.; Kanter, Ruben de; van de Kerkhof, Esther G.; Groothuis, Geny M. M. (2010): Preparation and incubation of precision-cut liver and intestinal slices for application in drug metabolism and toxicity studies. In *Nature protocols* 5 (9), pp. 1540–1551. DOI: 10.1038/nprot.2010.111.

Grimes, David Robert; Kelly, Catherine; Bloch, Katarzyna; Partridge, Mike (2014): A method for estimating the oxygen consumption rate in multicellular tumour spheroids. In *Journal of the Royal Society, Interface* 11 (92), p. 20131124. DOI: 10.1098/rsif.2013.1124.

Grün, Christoph; Pfeifer, Jana; Liebsch, Gregor; Gottwald, Eric (2023): O2-sensitive microcavity arrays: A new platform for oxygen measurements in 3D cell cultures. In *Frontiers in bioengineering and biotechnology* 11, p. 1111316. DOI: 10.3389/fbioe.2023.1111316.

Guyon, Joris; Daubon, Thomas (2023): Histological analysis of invasive glioblastoma organoids embedded in a 3D collagen matrix. In *STAR protocols* 4 (3), p. 102521. DOI: 10.1016/j.xpro.2023.102521.

Hajek, Kathrin; Wegener, Joachim (2017): Independent impedimetric analysis of two cell populations co-cultured on opposite sides of a porous support. In *Experimental cell research* 351 (1), pp. 121–126. DOI: 10.1016/j.yexcr.2017.01.003.

Hatz, Sonja; Lambert, John D. C.; Ogilby, Peter R. (2007): Measuring the lifetime of singlet oxygen in a single cell: addressing the issue of cell viability. In *Photochemical & photobiological sciences : Official journal of the European Photochemistry Association and the European Society for Photobiology* 6 (10), pp. 1106–1116. DOI: 10.1039/b707313e.

Hermanns, Maria Iris; Unger, Ronald E.; Kehe, Kai; Peters, Kirsten; Kirkpatrick, Charles James (2004): Lung epithelial cell lines in coculture with human pulmonary microvascular endothelial cells: development of an alveolo-capillary barrier in vitro. In *Laboratory investigation; a journal of technical methods and pathology* 84 (6), pp. 736–752. DOI: 10.1038/labinvest.3700081.

Hernández-Angeles, A.; Soria-Jasso, L. E.; Ortega, A.; Arias-Montaño, J. A. (2001): Histamine H1 receptor activation stimulates mitogenesis in human astrocytoma U373 MG cells. In *Journal of neuro-oncology* 55 (2), pp. 81–89. DOI: 10.1023/A:1013338515229.

Hildebrandt, Cornelia; Büth, Heiko; Cho, Sungbo; Impidjati; Thielecke, Hagen (2010): Detection of the osteogenic differentiation of mesenchymal stem cells in 2D and 3D cultures by electrochemical impedance spectroscopy. In *Journal of biotechnology* 148 (1), pp. 83–90. DOI: 10.1016/j.jbiotec.2010.01.007.

Hirschhaeuser, Franziska; Menne, Heike; Dittfeld, Claudia; West, Jonathan; Mueller-Klieser, Wolfgang; Kunz-Schughart, Leoni A. (2010): Multicellular tumor spheroids: an underestimated tool is catching up again. In *Journal of biotechnology* 148 (1), pp. 3–15. DOI: 10.1016/j.jbiotec.2010.01.012.

Hishinuma, S.; Young, J. M. (1995): Characteristics of the binding of 3H-mepyramine to intact human U373 MG astrocytoma cells: evidence for histamine-induced H1-receptor internalisation. In *British journal of pharmacology* 116 (6), pp. 2715–2723. DOI: 10.1111/j.1476-5381.1995.tb17232.x.

Hoheisel, D.; Nitz, T.; Franke, H.; Wegener, J.; Hakvoort, A.; Tilling, T.; Galla, H. J. (1998): Hydrocortisone reinforces the blood-brain barrier properties in a serum free cell culture system. In *Biochemical and biophysical research communications* 244 (1), pp. 312–316. DOI: 10.1006/bbrc.1997.8051.

Hujber, Zoltán; Horváth, Gergő; Petővári, Gábor; Krencz, Ildikó; Dankó, Titanilla; Mészáros, Katalin et al. (2018): GABA, glutamine, glutamate oxidation and succinic semialdehyde dehydrogenase expression in human gliomas. In *Journal of experimental & clinical cancer research : CR* 37 (1), p. 271. DOI: 10.1186/s13046-018-0946-5.

Hupf, Christina (2018): Impedance-based analysis of 3D tissue models: A novel measurement setup for novel measurement modes. Universität Regensburg.

Hytti, Maria; Korhonen, Eveliina; Hyttinen, Juha M. T.; Roehrich, Heidi; Kaarniranta, Kai; Ferrington, Deborah A.; Kauppinen, Anu (2019): Antimycin A-Induced Mitochondrial Damage Causes Human RPE Cell Death despite Activation of Autophagy. In *Oxidative medicine and cellular longevity* 2019, p. 1583656. DOI: 10.1155/2019/1583656.

Itoh, Takao (2012): Fluorescence and phosphorescence from higher excited states of organic molecules. In *Chemical reviews* 112 (8), pp. 4541–4568. DOI: 10.1021/cr200166m.

Jiang, L.; Xiao, L.; Sugiura, H.; Huang, X.; Ali, A.; Kuro-o, M. et al. (2015): Metabolic reprogramming during TGFβ1-induced epithelial-to-mesenchymal transition. In *Oncogene* 34 (30), pp. 3908–3916. DOI: 10.1038/onc.2014.321.

Kalluri, Raghu; Weinberg, Robert A. (2009): The basics of epithelial-mesenchymal transition. In *The Journal of clinical investigation* 119 (6), pp. 1420–1428. DOI: 10.1172/JCI39104.

Kamiloglu, Senem; Sari, Gulce; Ozdal, Tugba; Capanoglu, Esra (2020): Guidelines for cell viability assays. In *Food Frontiers* 1 (3), pp. 332–349. DOI: 10.1002/fft2.44.

Kang, Young Bok Abraham; Rawat, Siddhartha; Cirillo, Joseph; Bouchard, Michael; Noh, Hongseok Moses (2013): Layered long-term co-culture of hepatocytes and endothelial cells on a transwell membrane: toward engineering the liver sinusoid. In *Biofabrication* 5 (4), p. 45008. DOI: 10.1088/1758-5082/5/4/045008.

Kelm, Jens M.; Timmins, Nicholas E.; Brown, Catherine J.; Fussenegger, Martin; Nielsen, Lars K. (2003): Method for generation of homogeneous multicellular tumor spheroids applicable to a wide variety of cell types. In *Biotechnology and bioengineering* 83 (2), pp. 173–180. DOI: 10.1002/bit.10655.

Kessel, Sarah; Cribbes, Scott; Déry, Olivier; Kuksin, Dmitry; Sincoff, Eric; Qiu, Jean; Chan, Leo Li-Ying (2017): High-Throughput 3D Tumor Spheroid Screening Method for Cancer Drug Discovery Using Celigo Image Cytometry. In *SLAS technology* 22 (4), pp. 454–465. DOI: 10.1177/2211068216652846.

Kijanska M., Kelm J. (2016): In vitro 3D Spheroids and Microtissues: ATP-based Cell Viability and Toxicity Assays. With assistance of Markossian S, Grossman A, Arkin M. Edited by Eli Lilly & Company and the national Center for Advancing Translational Sciences. Assay Guidance Manual [Internet]. Available online at https://www.ncbi.nlm.nih.gov/books/NBK343426/.

Kim, Geon; Hugonnet, Herve; Kim, Kyoohyun; Lee, Jae-Hyuk; Lee, Sung Sik; Ha, Jeongmin et al. (2024): Holotomography. In *Nature reviews. Methods primers* 4 (1). DOI: 10.1038/s43586-024-00327-1.

Kim, Jihoon; Koo, Bon-Kyoung; Knoblich, Juergen A. (2020): Human organoids: model systems for human biology and medicine. In *Nature reviews. Molecular cell biology* 21 (10), pp. 571–584. DOI: 10.1038/s41580-020-0259-3.

Kim, Yena; Park, Narae; Rim, Yeri Alice; Nam, Yoojun; Jung, Hyerin; Lee, Kijun; Ju, Ji Hyeon (2018): Establishment of a complex skin structure via layered co-culture of keratinocytes and fibroblasts derived from induced pluripotent stem cells. In *Stem cell research & therapy* 9 (1), p. 217. DOI: 10.1186/s13287-018-0958-2.

Kloss, Daniel; Fischer, Michael; Rothermel, Andrée; Simon, Jan C.; Robitzki, Andrea A. (2008): Drug testing on 3D in vitro tissues trapped on a microcavity chip. In *Lab on a chip* 8 (6), pp. 879–884. DOI: 10.1039/B800394G.

Krebs, Angela M.; Mitschke, Julia; Lasierra Losada, María; Schmalhofer, Otto; Boerries, Melanie; Busch, Hauke et al. (2017): The EMT-activator Zeb1 is a key factor for cell plasticity and promotes metastasis in pancreatic cancer. In *Nature cell biology* 19 (5), pp. 518–529. DOI: 10.1038/ncb3513.

Lakowicz, Joseph R. (2006): Principles of Fluorescence Spectroscopy. Boston, MA: Springer US.

Lam, Maggie; Lamanna, Emma; Organ, Louise; Donovan, Chantal; Bourke, Jane E. (2023): Perspectives on precision cut lung slices-powerful tools for investigation of mechanisms and therapeutic targets in lung diseases. In *Frontiers in pharmacology* 14, p. 1162889. DOI: 10.3389/fphar.2023.1162889.

LaMontagne, Erin; Muotri, Alysson R.; Engler, Adam J. (2022): Recent advancements and future requirements in vascularization of cortical organoids. In *Frontiers in bioengineering and biotechnology* 10, p. 1048731. DOI: 10.3389/fbioe.2022.1048731.

Larco, J. E. de; Todaro, G. J. (1978): Epithelioid and fibroblastic rat kidney cell clones: epidermal growth factor (EGF) receptors and the effect of mouse sarcoma virus transformation. In *Journal of cellular physiology* 94 (3), pp. 335–342. DOI: 10.1002/jcp.1040940311.

Lee, Chung-Wein; Stantz, Keith M. (2016): Development of a mathematical model to estimate intra-tumor oxygen concentrations through multi-parametric imaging. In *Biomedical engineering online* 15 (1), p. 114. DOI: 10.1186/s12938-016-0235-5.

Lee, Mahn Jae; Lee, Jaehyeok; Ha, Jeongmin; Kim, Geon; Kim, Hye-Jin; Lee, Sumin et al. (2024): Long-term three-dimensional high-resolution imaging of live unlabeled small intestinal organoids via low-coherence holotomography. In *Experimental & molecular medicine* 56 (10), pp. 2162–2170. DOI: 10.1038/s12276-024-01312-0.

Lee, Rhianna E.; Reidel, Boris; Nelson, Mark R.; Macdonald, Jade K.; Kesimer, Mehmet; Randell, Scott H. (2023): Air-Liquid interface cultures to model drug delivery through the mucociliary epithelial barrier. In *Advanced drug delivery reviews* 198, p. 114866. DOI: 10.1016/j.addr.2023.114866.

Lieb, S.; Michaelis, S.; Plank, N.; Bernhardt, G.; Buschauer, A.; Wegener, J. (2016): Label-free analysis of GPCR-stimulation: The critical impact of cell adhesion. In *Pharmacological research* 108, pp. 65–74. DOI: 10.1016/j.phrs.2016.04.026.

Lovisa, Sara (2021): Epithelial-to-Mesenchymal Transition in Fibrosis: Concepts and Targeting Strategies. In *Frontiers in pharmacology* 12, p. 737570. DOI: 10.3389/fphar.2021.737570.

Lukic, Sonja; Wegener, Joachim (2005): Impedimetric Monitoring of Cell-Based Assays. In : Encyclopedia of Life Sciences: Wiley, pp. 1–8.

Madhu, Manivannan; Santhoshkumar, S.; Tseng, Wei-Bin; Tseng, Wei-Lung (2023): Maximizing analytical precision: exploring the advantages of ratiometric strategy in fluorescence, Raman, electrochemical, and mass spectrometry detection. In *Front. Anal. Sci.* 3, Article 1258558. DOI: 10.3389/frans.2023.1258558.

Majorova, Dominika; Atkins, Elizabeth; Martineau, Henny; Vokral, Ivan; Oosterhuis, Dorenda; Olinga, Peter et al. (2021): Use of Precision-Cut Tissue Slices as a Translational Model to Study Host-Pathogen Interaction. In *Frontiers in veterinary science* 8, p. 686088. DOI: 10.3389/fvets.2021.686088.

Mamchaoui, K.; Saumon, G. (2000): A method for measuring the oxygen consumption of intact cell monolayers. In *American journal of physiology. Lung cellular and molecular physiology* 278 (4), L858-63. DOI: 10.1152/ajplung.2000.278.4.L858.

Materi, Wayne; Wishart, David S. (2007): Computational systems biology in cancer: modeling methods and applications. In *Gene regulation and systems biology* 1, pp. 91–110.

Mazibuko-Mbeje, Sithandiwe E.; Mthembu, Sinenhlanhla X. H.; Dludla, Phiwayinkosi V.; Madoroba, Evelyn; Chellan, Nireshni; Kappo, Abidemi P.; Muller, Christo J. F. (2021): Antimycin A-induced mitochondrial dysfunction is consistent with impaired insulin signaling

in cultured skeletal muscle cells. In *Toxicology in vitro : an international journal published in association with BIBRA* 76, p. 105224. DOI: 10.1016/j.tiv.2021.105224.

Mazzocchi, Andrea R.; Man, Alan J.; DesOrmeaux, Jon-Paul S.; Gaborski, Thomas R. (2014): Porous Membranes Promote Endothelial Differentiation of Adipose-Derived Stem Cells and Perivascular Interactions. In *Cel. Mol. Bioeng.* 7 (3), pp. 369–378. DOI: 10.1007/s12195-014-0354-7.

Molckovsky, A.; Wilson, B. C. (2001): Monitoring of cell and tissue responses to photodynamic therapy by electrical impedance spectroscopy. In *Physics in medicine and biology* 46 (4), pp. 983–1002. DOI: 10.1088/0031-9155/46/4/306.

Molter, Timothy W.; McQuaide, Sarah C.; Suchorolski, Martin T.; Strovas, Tim J.; Burgess, Lloyd W.; Meldrum, Deirdre R.; Lidstrom, Mary E. (2009): A microwell array device capable of measuring single-cell oxygen consumption rates. In *Sensors and actuators. B, Chemical* 135 (2), pp. 678–686. DOI: 10.1016/j.snb.2008.10.036.

Mookerjee, Shona A.; Gerencser, Akos A.; Nicholls, David G.; Brand, Martin D. (2017): Quantifying intracellular rates of glycolytic and oxidative ATP production and consumption using extracellular flux measurements. In *Journal of Biological Chemistry* 292 (17), pp. 7189–7207. DOI: 10.1074/jbc.M116.774471.

Mueller-Klieser, W.; Freyer, J. P.; Sutherland, R. M. (1986): Influence of glucose and oxygen supply conditions on the oxygenation of multicellular spheroids. In *British journal of cancer* 53 (3), pp. 345–353. DOI: 10.1038/bjc.1986.58.

Mueller-Klieser, W. F.; Sutherland, R. M. (1982): Oxygen tensions in multicell spheroids of two cell lines. In *British journal of cancer* 45 (2), pp. 256–264. DOI: 10.1038/bjc.1982.41.

Mukomoto, Rei; Nashimoto, Yuji; Terai, Takato; Imaizumi, Takuto; Hiramoto, Kaoru; Ino, Kosuke et al. (2020): Oxygen consumption rate of tumour spheroids during necrotic-like core formation. In *The Analyst* 145 (19), pp. 6342–6348. DOI: 10.1039/D0AN00979B.

Naber, Tobias; Winter, Katharina; Wegener, Joachim (2025): TER-Ox: Simultaneous Monitoring of Epithelial Barrier Function (TER) and Mitochondrial Respiration (Ox). In *Applied Research* 4 (1), Article e202400172. DOI: 10.1002/appl.202400172.

Ochi, Mitsuo (2013): Shinya Yamanaka's 2012 Nobel Prize and the radical change in orthopedic strategy thanks to his discovery of iPS cells. In *Acta orthopaedica* 84 (1), pp. 1–3. DOI: 10.3109/17453674.2013.765642.

Ogita, Masaki; Ogita, Akira; Usuki, Yoshinosuke; Fujita, Ken-ichi; Tanaka, Toshio (2009): Antimycin A-induced cell death depends on AIF translocation through NO production and PARP activation and is not involved in ROS generation, cytochrome c release and caspase-3 activation in HL-60 cells. In *The Journal of antibiotics* 62 (3), pp. 145–152. DOI: 10.1038/ja.2009.2.

Parfitt, Geraint J. (2019): Immunofluorescence Tomography: High-resolution 3-D reconstruction by serial-sectioning of methacrylate embedded tissues and alignment of 2-D immunofluorescence images. In *Scientific reports* 9 (1). DOI: 10.1038/s41598-018-38232-9.

Parrish, A. R.; Gandolfi, A. J.; Brendel, K. (1995): Precision-cut tissue slices: applications in pharmacology and toxicology. In *Life sciences* 57 (21), pp. 1887–1901. DOI: 10.1016/0024-3205(95)02176-J.

Paşca, Anca M.; Sloan, Steven A.; Clarke, Laura E.; Tian, Yuan; Makinson, Christopher D.; Huber, Nina et al. (2015): Functional cortical neurons and astrocytes from human pluripotent stem cells in 3D culture. In *Nature methods* 12 (7), pp. 671–678. DOI: 10.1038/nmeth.3415.

Patra, Bishnubrata; Peng, Chien-Chung; Liao, Wei-Hao; Lee, Chau-Hwang; Tung, Yi-Chung (2016): Drug testing and flow cytometry analysis on a large number of uniform sized tumor spheroids using a microfluidic device. In *Scientific reports* 6, p. 21061. DOI: 10.1038/srep21061.

Patrone, Laura M.; Cook, Jeffrey R.; Crute, Barbara E.; Buskirk, Robert G. (1992): Differentiation of epithelial cells on microporous membranes. In *Journal of Tissue Culture Methods* 14 (4), pp. 225–234. DOI: 10.1007/BF01409015.

Piehowski, Paul D.; Zhu, Ying; Bramer, Lisa M.; Stratton, Kelly G.; Zhao, Rui; Orton, Daniel J. et al. (2020): Automated mass spectrometry imaging of over 2000 proteins from tissue sections at 100-µm spatial resolution. In *Nature communications* 11 (1), p. 8. DOI: 10.1038/s41467-019-13858-z.

Plitzko, Birte; Loesgen, Sandra (2018): Measurement of Oxygen Consumption Rate (OCR) and Extracellular Acidification Rate (ECAR) in Culture Cells for Assessment of the Energy Metabolism. In *Bio-protocol* 8 (10), e2850. DOI: 10.21769/BioProtoc.2850.

Pontén, J.; Macintyre, E. H. (1968): Long term culture of normal and neoplastic human glia. In *Acta pathologica et microbiologica Scandinavica* 74 (4), pp. 465–486. DOI: 10.1111/j.1699-0463.1968.tb03502.x.

Preuß, Eike B.; Schubert, Stephanie; Werlein, Christopher; Stark, Helge; Braubach, Peter; Höfer, Anne et al. (2022): The Challenge of Long-Term Cultivation of Human Precision-Cut Lung Slices. In *The American journal of pathology* 192 (2), pp. 239–253. DOI: 10.1016/j.ajpath.2021.10.020.

Prozialeck, Walter C.; Edwards, Joshua R.; Lamar, Peter C.; Smith, Conor S. (2006): Epithelial barrier characteristics and expression of cell adhesion molecules in proximal tubule-derived cell lines commonly used for in vitro toxicity studies. In *Toxicology in vitro : an international journal published in association with BIBRA* 20 (6), pp. 942–953. DOI: 10.1016/j.tiv.2005.11.006.

Pütz, Lisa (2022): Imaging Microphysiometry of 2D and 3D Tissue Models: Method Development and Application. Universität Regensburg.

Qian, Xuyu; Song, Hongjun; Ming, Guo-Li (2019): Brain organoids: advances, applications and challenges. In *Development (Cambridge, England)* 146 (8). DOI: 10.1242/dev.166074.

Ren, Hui; Birch, Nigel P.; Suresh, Vinod (2016): An Optimised Human Cell Culture Model for Alveolar Epithelial Transport. In *PloS one* 11 (10), e0165225. DOI: 10.1371/journal.pone.0165225.

Ren, Yi; Shen, Han-Ming (2019): Critical role of AMPK in redox regulation under glucose starvation. In *Redox biology* 25, p. 101154. DOI: 10.1016/j.redox.2019.101154.

Russell, Shonagh; Wojtkowiak, Jonathan; Neilson, Andy; Gillies, Robert J. (2017): Metabolic Profiling of healthy and cancerous tissues in 2D and 3D. In *Scientific reports* 7 (1), p. 15285. DOI: 10.1038/s41598-017-15325-5.

Samudio, Ismael; Fiegl, Michael; Andreeff, Michael (2009): Mitochondrial uncoupling and the Warburg effect: molecular basis for the reprogramming of cancer cell metabolism. In *Cancer Research* 69 (6), pp. 2163–2166. DOI: 10.1158/0008-5472.CAN-08-3722.

Schliwa, M. (1982): Action of cytochalasin D on cytoskeletal networks. In *The Journal of cell biology* 92 (1), pp. 79–91. DOI: 10.1083/jcb.92.1.79.

Schmittlein, Carina (2018): Sensors and Actuators for 2D and 3D Cell Culture Models based on Oxygen Sensitive Culture Substrates. Universität Regensburg.

Schneckenburger, Herbert; Richter, Verena (2021): Challenges in 3D Live Cell Imaging. In *Photonics* 8 (7), p. 275. DOI: 10.3390/photonics8070275.

Schreml, Stephan; Meier, Robert J.; Wolfbeis, Otto S.; Landthaler, Michael; Szeimies, Rolf-Markus; Babilas, Philipp (2011): 2D luminescence imaging of pH in vivo. In *Proceedings of the National Academy of Sciences of the United States of America* 108 (6), pp. 2432–2437. DOI: 10.1073/pnas.1006945108.

Sheridan, Steven D.; Gil, Sonia; Wilgo, Matthew; Pitt, Aldo (2008): Microporous membrane growth substrates for embryonic stem cell culture and differentiation. In *Methods in cell biology* 86, pp. 29–57. DOI: 10.1016/S0091-679X(08)00003-4.

Shiraishi, Akari; Oh-Hara, Tomoko; Takahashi, Yuki; Uchibori, Ken; Nishio, Makoto; Katayama, Ryohei (2024): 3D layered co-culture model enhances Trastuzumab Deruxtecan sensitivity and reveals the combined effect with G007-LK in HER2-positive non-small cell lung cancer. In *Biochemical and biophysical research communications* 725, p. 150255. DOI: 10.1016/j.bbrc.2024.150255.

Shlomo, Yael; Gavriel, Mark; Jaffa, Ariel J.; Grisaru, Dan; Elad, David (2024): Arrangement into layers and mechanobiology of multi-cell co-culture models of the uterine wall. In *Human reproduction (Oxford, England)* 39 (8), pp. 1767–1777. DOI: 10.1093/humrep/deae130.

Sirenko, Oksana; Mitlo, Trisha; Hesley, Jayne; Luke, Steve; Owens, Windsor; Cromwell, Evan F. (2015): High-content assays for characterizing the viability and morphology of 3D cancer spheroid cultures. In *Assay and drug development technologies* 13 (7), pp. 402–414. DOI: 10.1089/adt.2015.655.

Slater, E. C. (1973): The mechanism of action of the respiratory inhibitor, antimycin. In *Biochimica et biophysica acta* 301 (2), pp. 129–154. DOI: 10.1016/0304-4173(73)90002-5.

Soule, H. D.; Vazguez, J.; Long, A.; Albert, S.; Brennan, M. (1973): A human cell line from a pleural effusion derived from a breast carcinoma. In *Journal of the National Cancer Institute* 51 (5), pp. 1409–1416. DOI: 10.1093/jnci/51.5.1409.

Stevenson, B. R.; Anderson, J. M.; Goodenough, D. A.; Mooseker, M. S. (1988): Tight junction structure and ZO-1 content are identical in two strains of Madin-Darby canine kidney cells which differ in transepithelial resistance. In *The Journal of cell biology* 107 (6 Pt 1), pp. 2401–2408. DOI: 10.1083/jcb.107.6.2401.

Stolwijk, Judith A.; Wegener, Joachim (2019): Impedance-Based Assays Along the Life Span of Adherent Mammalian Cells In Vitro: From Initial Adhesion to Cell Death. In. Berlin, Heidelberg: Springer Berlin Heidelberg (Bioanalytical Reviews).

Storck, Steffen E.; Pietrzik, Claus U. (2018): Die Blut-Hirn-Schranke und ihre Rolle in der Alzheimer – Krankheit. In *Neuroforum* 24 (4), pp. 287–296. DOI: 10.1515/nf-2018-0014.

Sun, Duxin; Gao, Wei; Hu, Hongxiang; Zhou, Simon (2022): Why 90% of clinical drug development fails and how to improve it? In *Acta pharmaceutica Sinica. B* 12 (7), pp. 3049–3062. DOI: 10.1016/j.apsb.2022.02.002.

Takahashi, Yuki; Morimura, Rii; Tsukamoto, Kei; Gomi, Sayaka; Yamada, Asuka; Mizukami, Miki et al. (2024): In vitro throughput screening of anticancer drugs using patient-derived cell lines cultured on vascularized three-dimensional stromal tissues. In *Acta biomaterialia* 183, pp. 111–129. DOI: 10.1016/j.actbio.2024.05.037.

Takegahara, Kyoshiro; Sakai, Kazuko; Mitsudomi, Tetsuya; Nishio, Kazuto (2021): P28-3 Epithelial-mesenchymal transition changes mitochondrial oxidative phosphorylation in the lung adenocarcinoma cells. In *Annals of Oncology* 32, S345. DOI: 10.1016/j.annonc.2021.05.731.

Teixeira, José; Basit, Farhan; Swarts, Herman G.; Forkink, Marleen; Oliveira, Paulo J.; Willems, Peter H. G. M.; Koopman, Werner J. H. (2018): Extracellular acidification induces ROS- and mPTP-mediated death in HEK293 cells. In *Redox biology* 15, pp. 394–404. DOI: 10.1016/j.redox.2017.12.018.

Terada, H. (1975): Some biochemical and physiochemical properties of the potent uncoupler SF 6847 (3,5-di-tert-butyl-4-hydroxybenzylidenemalononitrile). In *Biochimica et biophysica acta* 387 (3), pp. 519–532. DOI: 10.1016/0005-2728(75)90090-0.

Terada, H. (1990): Uncouplers of oxidative phosphorylation. In *Environmental health perspectives* 87, pp. 213–218. DOI: 10.1289/ehp.9087213.

Thakuri, Pradip Shahi; Gupta, Megha; Plaster, Madison; Tavana, Hossein (2019): Quantitative Size-Based Analysis of Tumor Spheroids and Responses to Therapeutics. In *Assay and drug development technologies* 17 (3), pp. 140–149. DOI: 10.1089/adt.2018.895.

Turcios, Lilia; Marti, Francesc; Watt, David S.; Kril, Lilia M.; Khurana, Aman; Chapelin, Fanny et al. (2020): Mitochondrial uncoupling and the disruption of the metabolic network in hepatocellular carcinoma. In *Oncotarget* 11 (31), pp. 3013–3024. DOI: 10.18632/oncotarget.27680.

Urban, Florian; Hajek, Kathrin; Naber, Tobias; Anczykowski, Boris; Schäfer, Marcus; Wegener, Joachim (2020): PETER-assay: Combined Impedimetric Detection of Permeability (PE) and

Resistance (TER) of Barrier-Forming Cell Layers. In *Scientific reports* 10 (1), p. 7373. DOI: 10.1038/s41598-020-63624-1.

Vadivelu, Raja; Kamble, Harshad; Shiddiky, Muhammad; Nguyen, Nam-Trung (2017): Microfluidic Technology for the Generation of Cell Spheroids and Their Applications. In *Micromachines* 8 (4), p. 94. DOI: 10.3390/mi8040094.

Vakhshiteh, Faezeh; Bagheri, Zeinab; Soleimani, Marziye; Ahvaraki, Akram; Pournemat, Parisa; Alavi, Seyed Ebrahim; Madjd, Zahra (2023): Heterotypic tumor spheroids: a platform for nanomedicine evaluation. In *Journal of nanobiotechnology* 21 (1), p. 249. DOI: 10.1186/s12951-023-02021-y.

Vanderkooi, J. M.; Maniara, G.; Green, T. J.; Wilson, D. F. (1987): An optical method for measurement of dioxygen concentration based upon quenching of phosphorescence. In *Journal of Biological Chemistry* 262 (12), pp. 5476–5482. DOI: 10.1016/S0021-9258(18)45596-2.

Wagner, Brett A.; Venkataraman, Sujatha; Buettner, Garry R. (2011): The rate of oxygen utilization by cells. In *Free radical biology & medicine* 51 (3), pp. 700–712. DOI: 10.1016/j.freeradbiomed.2011.05.024.

Wang, Wei; Liu, Yuanhui; Huang, Xiaochen; Liang, Feng; Luo, Haoyue; Mao, Zheng et al. (2024): Diffusion-based culture and real-time impedance monitoring of tumor spheroids in hydrogel microwells of a suspended membrane under microfluidic conditions. In *Talanta* 278, p. 126473. DOI: 10.1016/j.talanta.2024.126473.

Wegener, J.; Keese, C. R.; Giaever, I. (2000): Electric cell-substrate impedance sensing (ECIS) as a noninvasive means to monitor the kinetics of cell spreading to artificial surfaces. In *Experimental cell research* 259 (1), pp. 158–166. DOI: 10.1006/excr.2000.4919.

Wegener, J.; Zink, S.; Rösen, P.; Galla, H. (1999): Use of electrochemical impedance measurements to monitor beta-adrenergic stimulation of bovine aortic endothelial cells. In *Pflugers Archiv : European journal of physiology* 437 (6), pp. 925–934. DOI: 10.1007/s004240050864.

Wegener, Joachim; Abrams, Dimitri; Willenbrink, Wolfgang; Galla, Hans-Joachim; Janshoff, Andreas (2004): Automated multi-well device to measure transepithelial electrical resistances under physiological conditions. In *BioTechniques* 37 (4), 590, 592-4, 596-7. DOI: 10.2144/04374ST03.

Wiley, Luke A.; Beebe, David C.; Mullins, Robert F.; Stone, Edwin M.; Tucker, Budd A. (2016): A Method for Sectioning and Immunohistochemical Analysis of Stem Cell-Derived 3-D

Organoids. In *Current protocols in stem cell biology* 37, 1C.19.1-1C.19.11. DOI: 10.1002/cpsc.3.

Wilson, D. F. (1992): Oxygen dependent quenching of phosphorescence: a perspective. In *Advances in experimental medicine and biology* 317, pp. 195–201. DOI: 10.1007/978-1-4615-3428-0_20.

wu, yisha; Hao, Dingqian; Tu, Yanyi; Chen, Lin; Yu, Liang; Yu, Peng et al. (2023): The role of ZEB1 in regulating Tight junctions in Antrochoanal polyp.

Xie, Peisi; Zhao, Chao; Liang, Xiaoping; Huang, Wei; Chen, Yanyan; Cai, Zongwei (2020): Preparation of Frozen Sections of Multicellular Tumor Spheroids Coated with Ice for Mass Spectrometry Imaging. In *Analytical Chemistry* 92 (11), pp. 7413–7418. DOI: 10.1021/acs.analchem.9b05812.

Xing, Wei; Yin, Min; Lv, Qing; Hu, Yang; Liu, Changpeng; Zhang, Jiujun (2014): Oxygen Solubility, Diffusion Coefficient, and Solution Viscosity. In : Rotating Electrode Methods and Oxygen Reduction Electrocatalysts: Elsevier, pp. 1–31.

Yagi, S.; Inoue, H. (1962): The absorption of oxygen into sodium sulphite solution. In *Chemical Engineering Science* 17 (6), pp. 411–421. DOI: 10.1016/0009-2509(62)85010-6.

Yang, Rong; Wei, Tuo; Goldberg, Hannah; Wang, Weiping; Cullion, Kathleen; Kohane, Daniel S. (2017): Getting Drugs Across Biological Barriers. In *Advanced materials (Deerfield Beach, Fla.)* 29 (37). DOI: 10.1002/adma.201606596.

Yang, Xiao; Li, Congcong; Li, Peifeng; Fu, Qinrui (2023): Ratiometric optical probes for biosensing. In *Theranostics* 13 (8), pp. 2632–2656. DOI: 10.7150/thno.82323.

Yuhas, J. M.; Li, A. P.; Martinez, A. O.; Ladman, A. J. (1977): A simplified method for production and growth of multicellular tumor spheroids. In *Cancer Research* 37 (10), pp. 3639–3643.

Zamora-Perez, Paula; Xiao, Can; Sanles-Sobrido, Marcos; Rovira-Esteva, Muriel; Conesa, José Javier; Mulens-Arias, Vladimir et al. (2022): Multiphoton imaging of melanoma 3D models with plasmonic nanocapsules. In *Acta biomaterialia* 142, pp. 308–319. DOI: 10.1016/j.actbio.2022.01.052.

Zhang, Peijing; Sun, Yutong; Ma, Li (2015): ZEB1: at the crossroads of epithelial-mesenchymal transition, metastasis and therapy resistance. In *Cell cycle (Georgetown, Tex.)* 14 (4), pp. 481–487. DOI: 10.1080/15384101.2015.1006048.

Zhang, Xudong; Wang, William; Nordin, Anis Nurashikin; Li, Fang; Jang, Sunghoon; Voiculescu, Ioana (2017): The influence of the electrode dimension on the detection sensitivity of electric cell–substrate impedance sensing (ECIS) and its mathematical modeling. In *Sensors and actuators. B, Chemical* 247, pp. 780–790. DOI: 10.1016/j.snb.2017.03.047.

Zhao, Zixuan; Chen, Xinyi; Dowbaj, Anna M.; Sljukic, Aleksandra; Bratlie, Kaitlin; Lin, Luda et al. (2022): Organoids. In *Nature reviews. Methods primers* 2. DOI: 10.1038/s43586-022-00174-y.

Zinkl, Maria (2022): Impedance-based Analysis of Adherent Cells using Interdigitated Electrodes of Subcellular Dimensions. Universität Regensburg.

11 Appendix

11.1 Supplementary Information

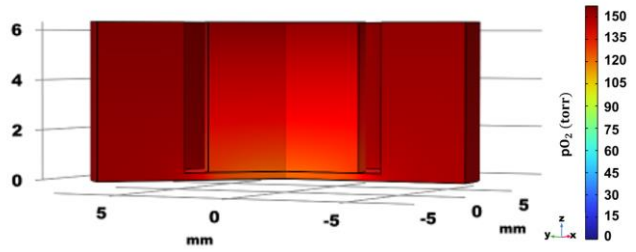

Figure S 1: 3D Plots visualizing the oxygen distribution of cells cultured on a permeable substrate after 12 hours. Data was obtained using finite element modeling. FEM was performed by Linda Frank. Figure adapted from Frank 2023.

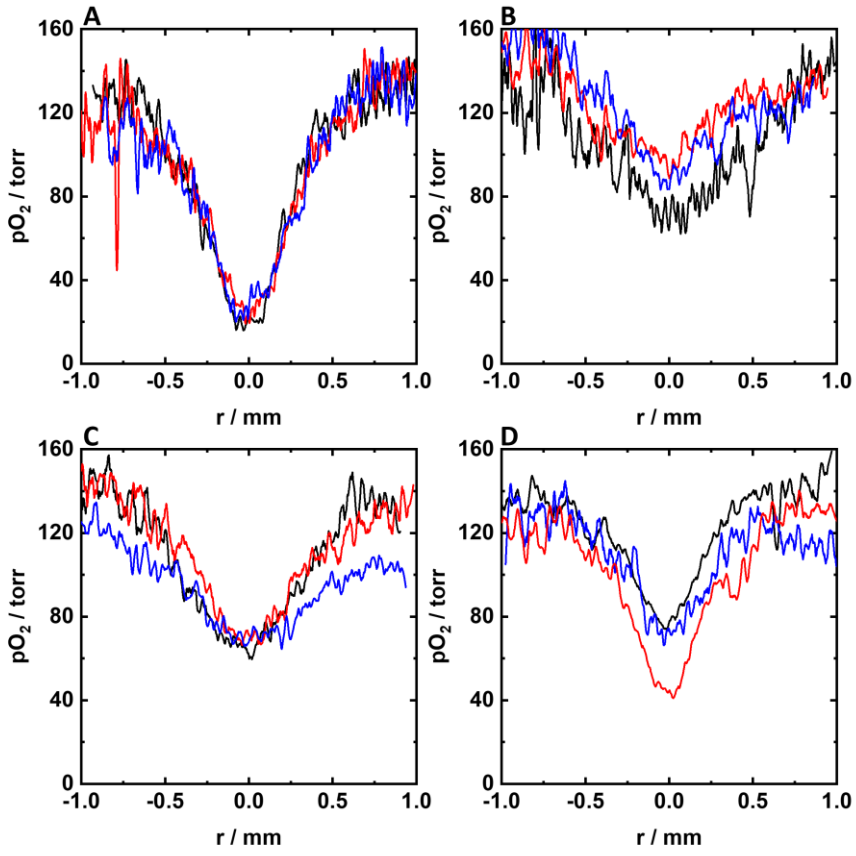

Figure S 2: Lateral oxygen profiles of spheroids from MCF-7 cells seeded with an initial cell number of $20 \cdot 10^3$ cells, cultured on (A) SFtl0.4 filters, (B) SFtp0.4 filters, (C) SFtl1.0 filters and (D) SFtl3.0 filters. Each color represents an individual experiment. Data was recorded using the VisiSens TD mic setup. All experiments were performed in a standard cell culture incubator at 37°C and 0 % CO_2.

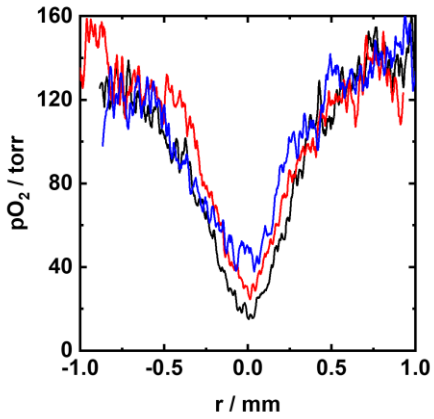

Figure S 3: Lateral oxygen profiles of spheroids from MCF-7 cells seeded with an initial cell number of $4 \cdot 10^3$ cells, cultured SFtl0.4 filters. Each color represents an individual experiment. Data was recorded using the VisiSens TD mic setup. All experiments were performed in a standard cell culture incubator at 37°C and 0 % CO_2.

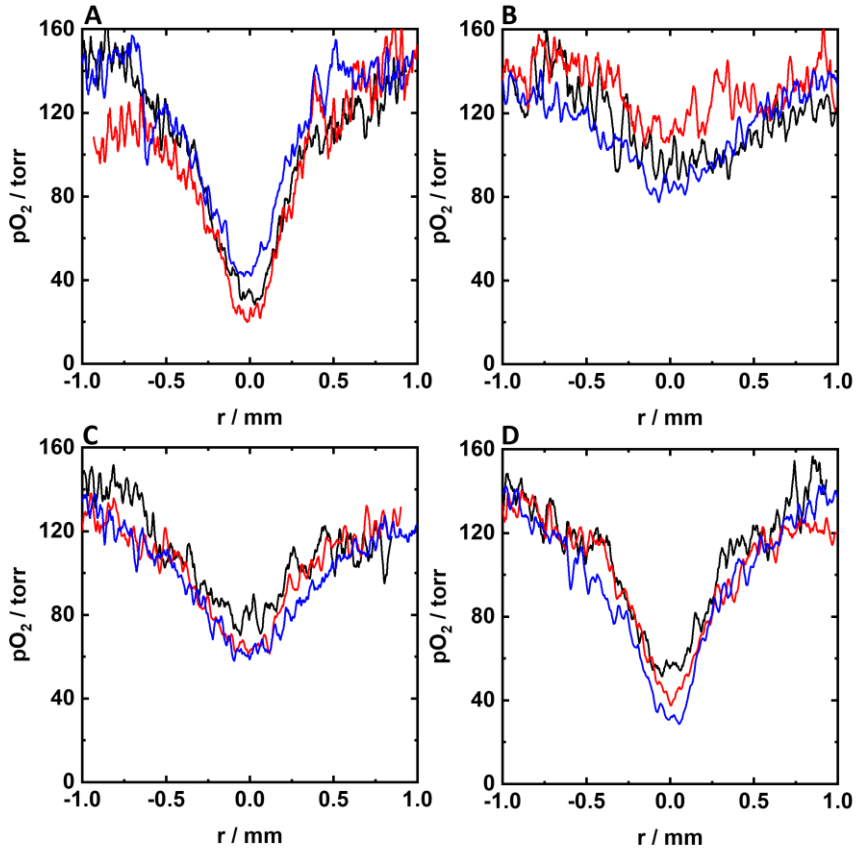

Figure S 4: Lateral oxygen profiles of spheroids from U373 MG cells seeded with an initial cell number of $30 \cdot 10^3$ cells, cultured on (A) SFtl0.4 filters, (B) SFtp0.4 filters, (C) SFtl1.0 filters and (D) SFtl3.0 filters. Each color represents an individual experiment. Data was recorded using the VisiSens TD mic setup. All experiments were performed in a standard cell culture incubator at 37°C and 0 % CO_2.

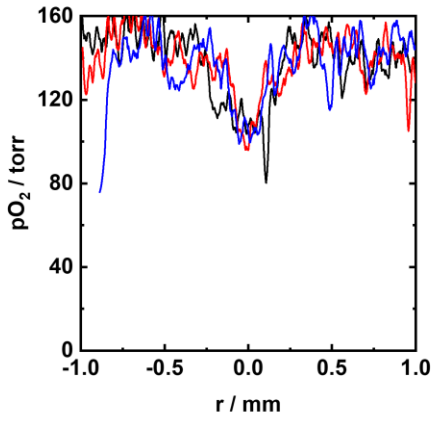

Figure S 5: Lateral oxygen profiles of spheroids from U373 MG cells seeded with an initial cell number of $6 \cdot 10^3$ cells, cultured on SFtl0.4 filters. Each color represents an individual experiment. Data was recorded using the VisiSens TD mic setup. All experiments were performed in a standard cell culture incubator at 37°C and 0 % CO_2.

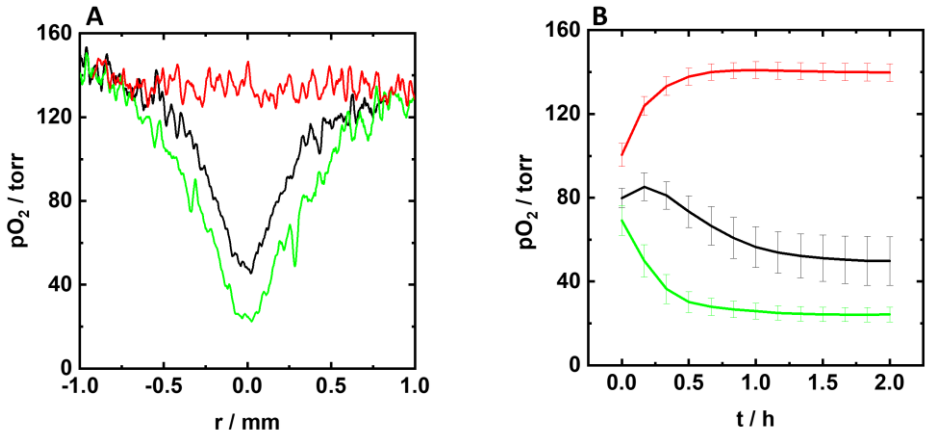

Figure S 6: Lateral oxygen profiles (A) and partial oxygen pressure time courses (B) of spheroids from MCF-7 cells seeded with an initial cell number of $4 \cdot 10^3$ cells and cultured on SFtl0.4 filters. Cells were treated with **L15 (control)**, **antimycin A (2 µM)** and **malonoben (100 nM)**. Data were recorded using the VisiSens TD mic setup. All experiments were performed in a standard cell culture incubator at 37 °C and 0 % CO_2.

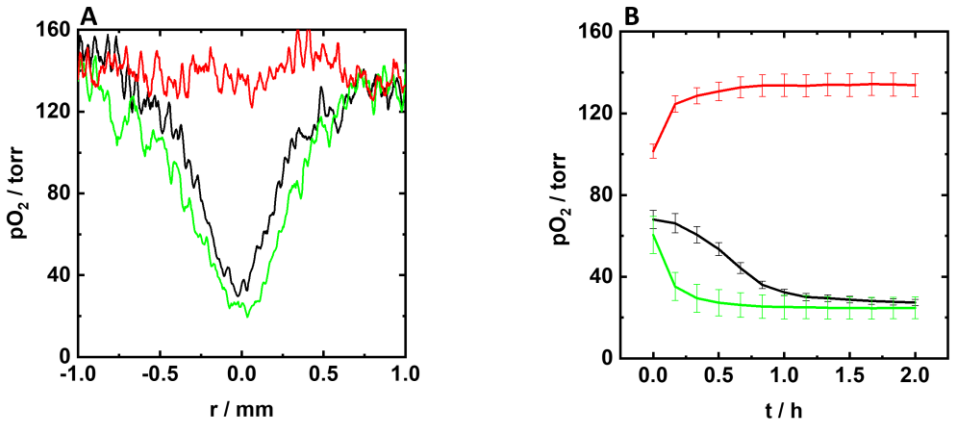

Figure S 7: Lateral oxygen profiles (A) and partial oxygen pressure time courses (B) of spheroids from U373 cells seeded with an initial cell number of $30 \cdot 10^3$ cells and cultured on SFtl0.4 filters. Cells were treated with **L15 (control)**, **antimycin A (2 µM)** and **malonoben (100 nM)**. Data were recorded using the VisiSens TD mic setup. All experiments were performed in a standard cell culture incubator at 37 °C and 0 % CO_2.

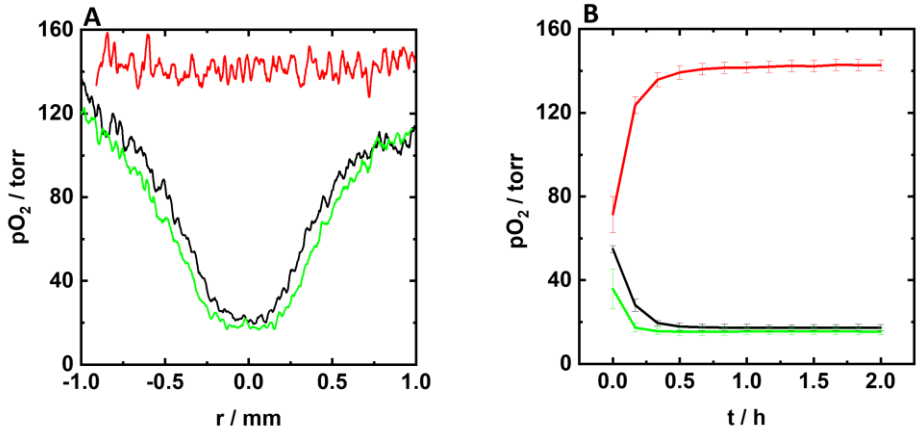

Figure S 8: Lateral oxygen profiles (A) and partial oxygen pressure time courses (B) of spheroids from SK-Mel cells seeded with an initial cell number of $4 \cdot 10^3$ cells and cultured on SFtl0.4 filters. Cells were treated with **L15 (control)**, **antimycin A (2 µM)** and **malonoben (100 nM)**. Data were recorded using the VisiSens TD mic setup. All experiments were performed in a standard cell culture incubator at 37 °C and 0 % CO_2.

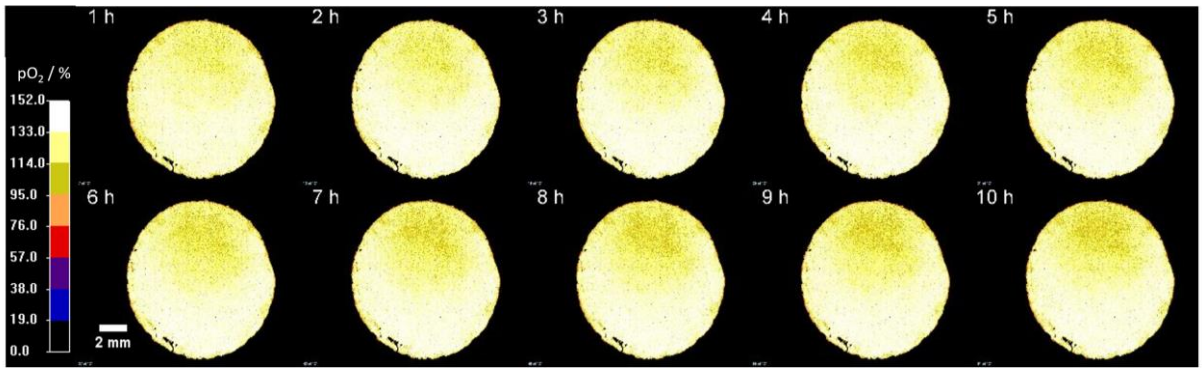

Figure S 9: Oxygen distribution maps of a precision cut lung slice in L15 buffer. PCLS was applied directly on the sensor foil surface and fixated using a 12-well filter insert (d_{pore} = 0.4 µm, $\delta_{pore} = 100 \cdot 10^6$ pores/well) in an open system. Experiment was performed in a dry standard cell culture incubator at 37 °C and 0 % CO_2.

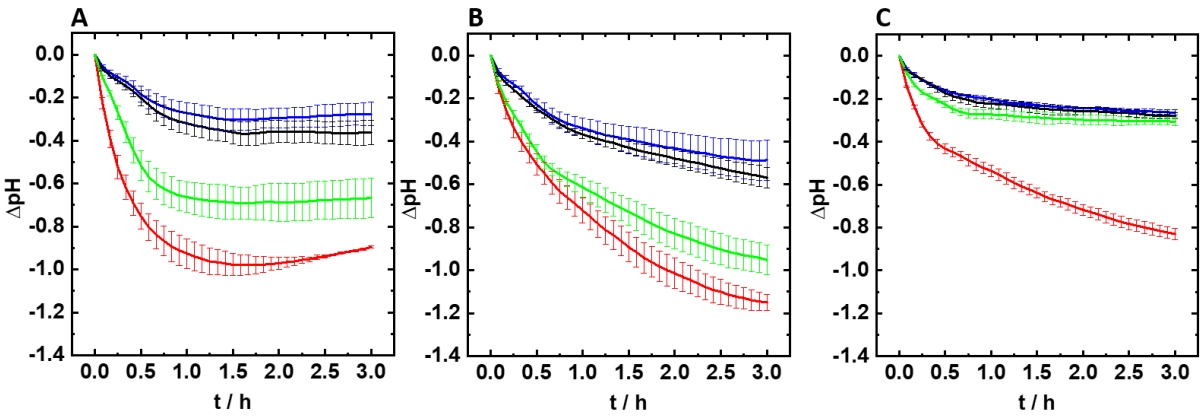

Figure S 10: Monitoring of extracellular pH of cell cultured on permeable substrates. Time course of normalized extracellular pH of (A) MCF-7 cells, (B) SK-Mel 28 and (C) U373 cells treated with a **control condition (L15-buffer + 4.5 g/L glucose)**, **L15-buffer**, **malonoben (100 nM)** and **antimycin A (2 µM)**. Data were recorded using the VisiSens TD setup in a dry cell culture incubator at 37 °C and 0 % CO_2 (Mean ± SEM, n = 3)

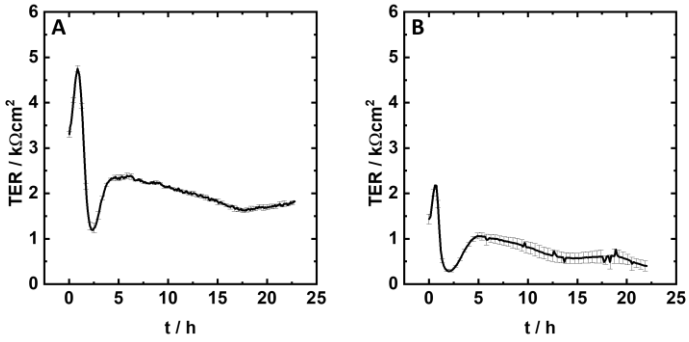

Figure S 11: (A) TER time course of MDCK-I cells measured using cellZscope® device. (B) TER time course of MDCK-I cells in L15 medium without Glucose addition measured with TER-Ox. All results were obtained in a dry cell culture incubator at 37°C and 0 % CO_2 in three individual measurements (Mean ± SEM).

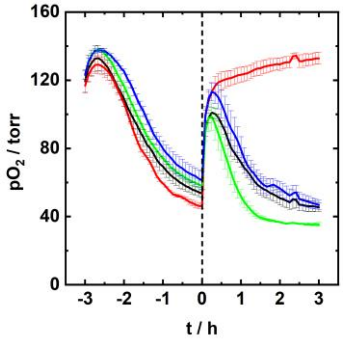

Figure S 12: Time course of oxygen partial pressure during the treatment of MDCK-II cells with a L15 buffer control, antimycin A (2 µM), malonoben (10 nM) and cytochalasin D (5 µM). The modulating drugs were added at t = 0 h (dashed line). Data was obtained using TER-Ox in a dry cell culture incubator at 37 °C and 0 % CO_2 in three individual experiments (Mean ± SEM).

11.2 Consumables and Devices

12-well cell culture plate	TPP Techno Plastic Products AG
24-well cell culture plate	Greiner Bio-One GmbH
96-well cell culture plate	Greiner Bio-One GmbH
agarose	Sigma-Aldrich
Bunsen burner	IBS Tecnomara GmbH
Bürker Chamber	Paul Marienfeld GmbH & Co. KG
cell counter	Thermo Fisher Scientific Inc.
cell culture flasks	Greiner Bio-One GmbH
cell culture incubator	Thermo Fisher Scientific Inc.
cell culture incubator	Memmert GmbH & Co. KG
cell culture medium	Sigma-Aldrich
Centrifuge Hereus Multifuge	Thermo Fisher Scientific Inc.
cellstar® tubes (15 mL, 50 mL)	Greiner Bio-One GmbH
cellZscope®	nanoAnalytics GmbH
centrifuge tubes (15 mL, 50 mL)	Sarstedt AG & Co. KG
Cytochalasin D	Cayman Chemical Company
D-glucose	Merck KGaA
DMEM	Sigma-Aldrich
DMSO	Carl Roth GmbH
EDTA	Sigma-Aldrich
eppendorf pipettes	Brand GmbH
ethanol	Merck KGaA
filter inserts	Sabeu GmbH & Co. KG
filter inserts (Transwell®)	Corning Inc.
HEPES	Carl Roth GmbH
impedance analyzer SI 1260	Solartron
L-15 medium	Sigma-Aldrich
laminar air flow cabinet	Thermo Fisher Scientific Inc.
Lexan® type 8010 colorless 112 polish	alt-intech
L-glutamine	Sigma-Aldrich
liquid nitrogen tank German Cryo	Jutta Ohst german-cryo GmbH
Nikon Diaphot inverted phase contrast microscope	Nikon Instruments Europe

office 365	Microsoft Corp.
origin pro 2022	OriginLab Corp.
orbital shaker KM-2 AKKU	Edmund Bühler GmbH
oxygen sensitive sensor foil SF-RPSu4	PreSens Precision Sensing GmbH
PBS	Sigma-Aldrich
pH electrode	Xylem Inc.
pH meter LabStar	Schott Instruments
pH sensitive sensor foil SF-HP5R	PreSens Precision Sensing GmbH
pipette tips (10 µL, 200 µL, 1 mL)	Sarstedt AG & Co. KG
plasma cleaner PDC 32G-2	Harrick Plasma
self-adhesive aluminum foil	Greiner Bio-One GmbH
silicon fat, KORASINOL-Paste	Kurt Obermeier GmbH & Co. KG
silicon glue	RS Components Ltd.
silicon rubber, Product-Nr.: 240000100	Technischer Handel Straub
sodium sulfite	Merck KGaA
steam autoclave DX-45	Systec GmbH
trypsin	Sigma-Aldrich
VisiSens TD (mic)	PreSens Precision Sensing GmbH
water bath Type TW12	Julabo

11.3 Abbreviations

°C	degree Celsius
%	percent
A	area
AC	alternating current
AEP	aerobic profile
amol	attomole
AntA	antimycin A
AOCR	apparent oxygen consumption rate
BBB	blood brain barrier
C	capacitance
C_{ap}	capacitance of the apical membrane
C_{bl}	capacitance of the basolateral membrane
C_{Cl}	capacitance of cell layer (equals TEC)
C_{ins}	capacitance of insert
CE	counter electrode
CIS	cellular impedance sensing
CLSM	confocal laser scanning microscope
cm	centimeter
cm^2	square centimeter
CO_2	carbon dioxide
CPE	constant phase element
cZs	cellZscope®
d	diameter, dimension
D	diffusion coefficient
DMEM	Dulbecco's Modified Eagle Medium
DMSO	dimethyl sulfoxide
DSMZ	Deutsche Sammlung von Mikroorganismen und Zellkulturen
δ	density
EAR	extracellular acidification rate
ECIS®	electric cell-substrate impedance sensing
EDTA	ethylenediaminetetraacetic acid
ETC	electron transport chain
f	frequency

FCS	fetal calf serum
fil	filter
(h)iPSCs	(human) induced pluripotent stem cells
h	hour
Hz	Hertz
I	current
IDE	interdigitated electrode
L	liter
L15-medium	Leibovitz's medium
max	maximum
MDCK	Madin Darby canine kidney
MEME	Minimum Essential Medium Eagle
min	minute
mL	milliliter
mpH	milli pH
µ	micro
µF	microfarad
µL	microliter
Na_2SO_3	sodium sulfite
nM	nanomolar
norm	normalized
NRK	normal rat kidney
OCR	oxygen consumption rate
OxPhos	oxidative phosphorylation
PBS	phosphate buffered saline
PCTS	precision cut tissue slices
PDMS	polydimethylsiloxane
pmol	picomole
pO_2	partial oxygen pressure
r	radius, profile
R_{Cl}	resistance of cell layer (equals TER)
R_{Ins}	resistance of insert
s	second
SEM	standard error of the mean

t	time
TEC	transepithelial electrical capacitance
TER	transepithelial electrical resistance
U	voltage
V	volume
Ω	ohm
ω	angular frequency
WE	working electrode
X	reactance
Y	admittance
Z	complex impedance
Z_{norm}	normalized impedance
$\|Z\|$	impedance magnitude

11.4 Curriculum Vitae

Tobias Naber

Lebenslauf

Persönliche Daten

Geburtsdatum:

22.07.1995

Geburtsort:

Regensburg

Nationalität:

Deutsch

E-Mail:

tobias.naber1@gmx.de

Ausbildung

Seit 01/2021	**Universität Regensburg / Fraunhofer EMFT** Doktorand, Wissenschaftlicher Mitarbeiter, Bioanalytik Thema: „Label-free, non-invasive phenotypic characterization of complex disease models"
10/2017 – 09/2020	**Universität Regensburg** Master of Science Chemie Schwerpunkte: (Bio-) Analytische Chemie, Physikalische Chemie, Biochemie, Nachhaltige Chemie Thema Masterarbeit: „Extending Microphysiometry to cell layers cultured on permeable substrates "
10/2014 – 09/2017	**Universität Regensburg** Bachelor of Science Chemie Thema Bachelorarbeit: „Zytotoxische Studien potenzieller Redoxsonden zur Untersuchung der Barrierefunktion von Epithelschichten"
05/2014	**Goethe Gymnasium Regensburg** Abitur, Auslandsjahr USA (2011/2012, Quincy Highschool, MI)

Nebenjobs & Praktika

Seit 01/2021	**Universität Regensburg** Wissenschaftliche Hilfskraft, Betreuung von chemischen Praktika, Allgemeine und Organische Chemie
09/2018 – 05/2019	**Université de Technologie de Compiègne** Praktikant in wissenschaftlichem Labor Thema: "Development and Characterization of bioactive dendritic polymers"

Tobias Naber

Lebenslauf

Kenntnisse & sonstige Qualifikationen

Sprachen	Deutsch (Muttersprache), Englisch (fließend), Französisch (Grundkenntnisse)
IT-Kenntnisse	Microsoft Office (sehr gut) Python (Grundkenntnisse) Joomla (Grundkenntnisse)
Soziales Engagement	**SWC Jura Nittendorf e.V.** Übungsleiter, Skilehrer, Ausschussmitglied (Öffentlichkeitsarbeit)

Konferenzen

IBCA 2023	**Conference on Impedance-based Cellular Assays** Poster & Talk „TER-Ox: Simultaneous monitoring of epithelial barrier function and respiration”
BBMEC 2024	**Workshop on Biosensors and Bioanalytical Microtechniques in Environmental, Food and Clinical Analysis** Poster & Talk „TER-Ox: Simultaneous monitoring of epithelial barrier function and respiration” **1st Prize: Best oral presentation**
3D cell culture 2025	**3D Cell Culture 2025: Functional Precision Medicine** Poster „Time resolved mapping of oxygen consumption and extracellular acidification in 3D tissue models”

11.5 List of publications

Journal Articles (accepted):

Naber, Tobias; Winter, Katharina; Wegener, Joachim (2025): TER-Ox: Simultaneous Monitoring of Epithelial Barrier Function (TER) and Mitochondrial Respiration (Ox). In *Applied Research* 4 (1), Article e202400172. DOI: 10.1002/appl.202400172

Application Notes:

Friedrich S., Goricnik B., Naber T., Meier R. J., Wegener Joachim (2024): Oxygen and pH Effects of Modulator Agents on SK-Mel Cell Cultures. https://www.presens.de/knowledge/publications/application-note/oxygen-and-ph-effects-of-modulator-agents-on-sk-mel-cell-cultures-2014. Stand: 27.02.2025

Friedrich S., Goricnik B., Naber T., Meier R. J., Wegener Joachim (2024): Studying Dose Response Relationship on MDCK-II cells (2024) https://www.presens.de/de/wissen/publikationen/applikationsbericht/studying-dose-response-relationship-on-mdck-ii-cells-2016. Stand: 27.02.2025

nanoAnalytics (2024): High-speed TEER monitoring of MDCK-I cells. https://www.nanoanalytics.com/en/products/cellzscope/applications/ap5-mdck-i-cell-layer-treated-with-saponin.html. Stand: 27.02.2025

Contributions to conferences:

Conference on Impedance-based Cellular Assays (IBCA 2023)

Poster & Talk: „TER-Ox: Simultaneous monitoring of epithelial barrier function and respiration”

Workshop on Biosensors and Bioanalytical Microtechniques in Environmental, Food and Clinical Analysis (BBMEC2024)

Poster & Talk: „TER-Ox: Simultaneous monitoring of epithelial barrier function and respiration”

1st Prize: Best oral presentation

3D Cell Culture 2025: Functional Precision Medicine

Poster: „Time resolved mapping of oxygen consumption and extracellular acidification in 3D tissue models”

Interviews:

https://www.sabeu.com/de/news/detail/interview-mit-dr-joachim-wegener, Stand: 21.05.2025

11.6 Danksagung

Es gibt so wahnsinnig viele Leute, denen ich zu danken habe. Viele Begleiter, die mich auf dieser Reise unterstützt und geprägt haben. Deswegen möchte ich mich, bevor ich mich nochmal Einzel-Personen widme, zuerst einmal bei Allen die ein Teil dieser unglaublich intensiven Zeit waren bedanken. Vielen Dank für eine großartige Zeit an der Uni Regensburg und am Fraunhofer EMFT.

Besonderer Dank gilt zunächst meinem Doktorvater! Joe, ich danke dir für die Unterstützung und dein Vertrauen während meiner Zeit als Doktorand aber auch schon vor meiner Promotion. Ich durfte eine wahnsinnig großartige Zeit in deinem Arbeitskreis verbringen, in der ich tolle Menschen kennenlernen und an interessanten Forschungsthemen arbeiten konnte. Ich danke dir auch für die vielen Gespräche abseits der Wissenschaft, sei es über Fußball oder auch andere private Themen, das hat immer sehr geholfen sich auch in „harten“ Zeiten wohlzufühlen. Und vergiss nie der Stern des Südens wird am Fußballhimmel immer der Hellste sein!

Weiterer Dank gilt den Mitgliedern meines Promotionskomitees. Vielen Dank an Karsten für die Übernahme des Postens als Zweitgutachter und die Reise aus Frankreich. An dieser Stelle möchte ich dir auch nochmal für die prägende Zeit, die ich in deiner Arbeitsgruppe verbringen durfte, danken! Danke an Miriam Breunig für die Übernahme des Postens als Drittprüferin. Danke auch an Thomas Hirsch für die Leitung des Prüfungskomitees.

Außerdem möchte ich gerne allen Studenten danken die ich in meiner Zeit als Doktorand in ihren Arbeiten begleiten durfte und die auch einen entscheidenden Anteil an meinem Erfolg geleistet haben. Rahel danke ich für die Messung vieeeeler Sphäroide im Rahmen ihrer Forschungsarbeit. Auch danke an Lukas der im Rahmen seiner Forschungsarbeit einen großen Teil der finalen pH-messungen durchgeführt hat. Saskia für ihren Einsatz im Forschungspraktikum und die Pionierarbeiten zu CIS-TER. Kathi und Lisa für ihren Einsatz in ihren Bachelorarbeiten. Beide konnte entscheidend zum Erfolg der Setups in Kapitel 5 bzw. Kapitel 7 beitragen. Nicht zuletzt möchte ich mich bei Jannik bedanken, der sich 9 Monate lang mit der Entwicklung und der Etablierung der pH Messungen beschäftigt hat und in der „gemeinsamen“ Zeit zu einem geschätzten Freund wurde.

Ein riesiges Dankeschön geht auch an alle weiteren Mitglieder des AGW in meiner Zeit als Doktorand aber auch davor. Ihr habt alle besonders dazu beigetragen, dass ich eine tolle Zeit verbringen konnte. Ganz besonders Nadja und Barbara die immer eingesprungen sind wenn es mal zu viel wurde und Nicole ohne die man wohl in so einige „bürokratische Problemchen“ gelaufen wäre.

Vor allem möchte ich hier aber meine langjährige Laborkollegin Anne hervorheben. Ich hoffe du weißt, wie dankbar ich dir bin für die vielen Gespräche, unser gegenseitiges Vertrauen und die gegenseitige Unterstützung. Du warst stets eine wichtige Säule und musstet doch auch einiges mit mir durch machen! Ich kann mich da an diverse Emotionsausbrüche erinnern. Dafür bin ich unendlich dankbar und ich hätte mir niemand besseren als Laborpartnerin vorstellen können!! Wir hatten wirklich eine tolle Zeit😊

Hier möchte ich auch die Mitglieder des Projektes A07 aus dem Konsortium des TRR305 erwähnen. Kim und mein Zwilling Ole, die verrückten Nordlichter für großartige Zeiten in Hamburg. Silvia und Natasa für die Zusammenarbeit in Regensburg. Ach ja, und danke für den legendären Skiurlaub 😊

Eine große Hilfe war auch die Feinmechanik Werkstatt der Chemie Fakultät der Uni Regensburg, die großen Anteil am finalen Layout der TER-Ox Kammer haben.

Ein Dank gilt auch den beiden Firmen PreSens und nanoAnalytics für die Zusammenarbeit in den letzten Jahren.

Danken möchte ich auch meiner treuen Freundesgruppe den Berbern. Die gemeinsamen Urlaube und die vielen verrückten Stunden waren immer eine willkommene Abwechslung.

Der letzte und in jedem Falle größte Dank geht aber an meine Familie und vor allem meine Eltern. Das Studium und auch die Promotion wären ohne eure Unterstützung unmöglich gewesen. Nicht jeder kann sich über so eine großartige Unterstützung seiner Eltern freuen und dafür bin ich unendlich dankbar, auch wenn es vielleicht manchmal nicht so rüberkommt :D Ich möchte hier auch unbedingt noch meinen Opa, Gerhard Naber erwähnen. Er war stets einer meiner größten Supporter während meines Studiums bis hinein in meine Doktorarbeit und kann das wunderbare Ende leider nicht mehr miterleben.

Ich danke euch allen von Herzen <3

11.7 Eidesstaatliche Erklärung

(1) Ich erkläre hiermit an Eides statt, dass ich die vorliegende Arbeit ohne unzulässige Hilfe Dritter und ohne Benutzung anderer als der angegebenen Hilfsmittel angefertigt habe; die aus anderen Quellen direkt oder indirekt übernommenen Daten und Konzepte sind unter Angabe des Literaturzitats gekennzeichnet.

(2) Weitere Personen waren an der inhaltlich-materiellen Herstellung der vorliegenden Arbeit nicht beteiligt. Insbesondere habe ich hierfür nicht die entgeltliche Hilfe eines Promotionsberaters oder anderer Personen in Anspruch genommen. Niemand hat von mir weder unmittelbar noch mittelbar geldwerte Leistungen für Arbeiten erhalten, die im Zusammenhang mit dem Inhalt der vorgelegten Dissertation stehen.

(3) Die Arbeit wurde bisher weder im In- noch im Ausland in gleicher oder ähnlicher Form einer anderen Prüfungsbehörde vorgelegt.

Datum / Ort	Unterschrift